Optical and structural properties of systems of conjugated molecules and graphenes

DISSERTATION

zur Erlangung des akademischen Grades

Dr. rer. nat.

im Fach Physik

eingereicht an der

Mathematisch-Naturwissenschaftlichen Fakultät I

der Humboldt-Universität zu Berlin

von

Dipl.-Phys. Philipp Lange

Präsident der Humboldt-Universität zu Berlin:

Prof. Dr. Jan-Hendrik Olbertz

Dekan der Mathematisch-Naturwissenschaftlichen Fakultät I:

Prof. Stefan Hecht PhD

Gutachter:

1. Prof. Dr. Jürgen P. Rabe
2. Prof. Dr. Oliver Benson
3. Ao. Univ.-Prof. DI Dr. Emil J.W. List-Kratochvil

Tag der mündlichen Prüfung: 18.03.2014

Abstract

Systems of conjugated molecules and graphenes bear high potential for applications in optics and optoelectronic devices. In addition these systems allow to investigate the interaction between nanoscale light emitters and quasi two-dimensional conducting layers like graphene. In this thesis optical microscopy, spectroscopy and scanning force microscopy are complementarily used to explore the optical and structural properties of such systems. In particular (i) the permeation barrier properties of graphene are quantified *in-situ* on a semiconducting organic layer. Furthermore (ii) the fluorescence and (iii) Raman emission of conjugated molecules in proximity to graphene are investigated and the respective coupling mechanisms are discussed.

(i) Graphene is a promising electrode material for flexible organic optoelectronic devices. Moreover, it may function as a permeation barrier to protect a device from chemical degradation under ambient conditions. Here the chemical and structural stability of graphenes is investigated *in-situ* on a fluorescent conjugated polymer film [poly(3-hexylthiophene)]. Defect free graphene is found to efficiently protect the polymer from degradation by oxygen and water from the ambient atmosphere. However, in single layer graphene a growing number of permeable defects is observed resulting from a weak photochemical degradation. In contrast few layer graphene remains free of permeable defects. This suggests that graphenes can serve as both transparent electrode and barrier layer in future optoelectronic devices.

(ii) Based on combined tight binding model and random phase approximation calculations graphene is considered to be plasmon active only up to the infrared. Here it is shown that the known optical properties of graphene as measured by ellipsometry and simulated by density functional theory imply the existence of strongly localized graphene plasmons in the visible with a line width of 0.1 eV. Using fluorescent emitters [rhodamine 6G (R6G)] that provide the high wave vectors necessary to excite graphene plasmons at optical frequencies, graphene plasmon induced excitation enhancement by nearly 3 orders of magnitude is demonstrated. Thus graphene can be considered as a potential candidate for highly integrated nano-optoelectronic devices.

(iii) Enhancement of Raman scattering of molecules through graphene is still controversially discussed in the literature. Here enhancement of the Raman cross section of molecules (R6G) in subnanometer proximity to graphene relative to its value in solution by one order of magnitude is demonstrated. It is shown that the results gained here and by others can be consistently interpreted with electromagnetic enhancement provided by coupling of graphene plasmons and the Raman scattering dipole. The large graphene plasmon linewidth relative to the Raman emission of the molecules is reason for the lower effective enhancement here as compared to fluorescence (see above). Yet the future design of antennas for additional direct farfield excitation of graphene plasmons makes graphene promising for the development of a powerful substrate for surface enhanced Raman spectroscopy.

In summary the studied systems allow to gain new insight in graphene's properties and highlight the potential of systems of conjugated molecules and graphenes for optoelectronic and nano-optical applications.

Zusammenfassung

Systeme aus konjugierten Molekülen und Graphenen bergen hohes Potential für Anwendungen in der Optik und in optoelektronischen Bauelementen. Darüber hinaus ermöglichen diese Systeme, die Wechselwirkung zwischen nanoskaligen Lichtemittern und quasi zweidimensionalen leitfähigen Schichten wie Graphen zu untersuchen. In dieser Arbeit werden optische Mikroskopie, Spektroskopie und Rasterkraftmikroskopie komplementär verwendet, um die optischen und strukturellen Eigenschaften solcher Systeme zu erforschen. Insbesondere werden (i) die Permeationsbarriere-Eigenschaften von Graphen *in-situ* auf einer halbleitenden organischen Schicht quantifiziert. Weiterhin werden (ii) die Fluoreszenz- und (iii) Raman-Emission von konjugierten Molekülen in der Nähe von Graphen untersucht und die entsprechenden Kopplungsmechanismen diskutiert.

(i) Graphen ist ein vielversprechendes Elektrodenmaterial für flexible organische optoelektronische Bauelemente. Zudem könnte es als Permeationsbarriere fungieren, um Bauelemente vor chemischer Degeneration unter Umgebungsbedingungen zu schützen. Hier wird die chemische und strukturelle Stabilität von Graphenen *in-situ* auf einem fluoreszenten konjugierten Polymerfilm [Poly(3-hexylthiophen)] untersucht. Defektfreies Graphen zeigt sich als effizienter Schutz des Polymers vor Degeneration durch Sauerstoff und Wasser aus der Umgebungsluft. Allerdings ist in Einzellagen-Graphen eine wachsende Anzahl permeabler Defekte feststellbar, die auf eine geringe photochemische Degradation zurückgeführt werden kann. Wenige Lagen Graphen hingegen bleiben frei von permeablen Defekten. Dies legt nahe, dass Graphene als transparente Elektrode sowie als Barrierematerial in künftigen optoelektronischen Bauelementen dienen können.

(ii) Basierend auf gekoppelten Tight-Binding-Model und Random-Phase-Approximation Berechnungen wird angenommen, dass Graphen nur bis ins Infrarote Plasmon-aktiv ist. Hier wird gezeigt, dass die bekannten optischen Eigenschaften von Graphen, mittels Ellipsometrie gemessen und mithilfe von Dichtefunktionaltheorie simuliert, die Existenz von stark lokalisierten Graphen-Plasmonen im Sichtbaren mit einer Linienbreite von 0.1 eV implizieren. Durch Verwendung von fluoreszenten Emittern [Rhodamin 6G (R6G)], welche die für

Anregung von Graphen-Plasmonen im optischen Frequenzbereich notwendigen großen Wellenvektor bereitstellen, wird Graphen-Plasmonen-induzierte Anregungsverstärkung von nahezu 3 Größenordnungen nachgewiesen. Demnach kann Graphen als potentieller Kandidat für hoch integrierte nano-optoelektronische Bauelemente angesehen werden.

(iii) Die Verstärkung der Raman-Streuung von Molekülen durch Graphen wird nach wie vor kontrovers in der Literatur diskutiert. Hier wird Verstärkung des Raman-Querschnittes von Molekülen (R6G) im subnanometer Abstand zu Graphen relativ zum Wert in Lösung um eine Größenordnung nachgewiesen. Es wird gezeigt, dass die hier gesammelten Ergebnisse und jene von anderen konsistent durch elektromagnetische Verstärkung aufgrund von Kopplung zwischen Graphen-Plasmonen und Raman-Streudipol interpretiert werden können. Die relativ zur Raman-Emission der Moleküle hohe Linienbreite der Graphen-Plasmonen ist Ursache für die kleinere effektive Verstärkung in diesem Fall, verglichen zur Fluoreszenz (siehe oben). Zukünftige Entwicklung von Antennen für zusätzliche direkte Anregung von Graphen-Plasmonen aus dem Fernfeld macht Graphen dennoch vielversprechend für die Entwicklung eines leistungsfähigen Substrates für oberflächenverstärkte Raman-Spektroskopie.

Zusammenfassend ermöglichen die analysierten Systeme neue Einblicke in die Eigenschaften von Graphen zu gewinnen und heben das Potential von Systemen aus konjugierten Molekülen und Graphenen für optoelektronische und nanooptische Anwendungen hervor.

Table of contents

1 Introduction

Graphene is a crystalline monolayer of carbon atoms arranged in a hexagonal lattice (Figure 1.1a).[1] It exhibits a visual transparency of almost 98%,[2] ballistic charge transport [3,4] and high flexibility [5,6]. Furthermore carbon is abundantly available on earth. Thus graphene is a promising alternative to the commonly used transparent indium-tin oxide electrodes, which are fabricated from limited indium resources.[7] Today various promising methods for large scale fabrication of graphene are available, e.g. growth on metal substrates by chemical vapour deposition (CVD) followed by a transfer process (Figure 1.1b),[8] reduction from graphene oxide [9,10] and fabrication from chemically synthesised nanographenes [11]. The applicability of the two former ones for electrode fabrication has recently been demonstrated in prototypical optoelectronic devices.[7,12,13] Combined with organic electronics the broad introduction of flexible "all-carbon devices" may become possible.[14,15]

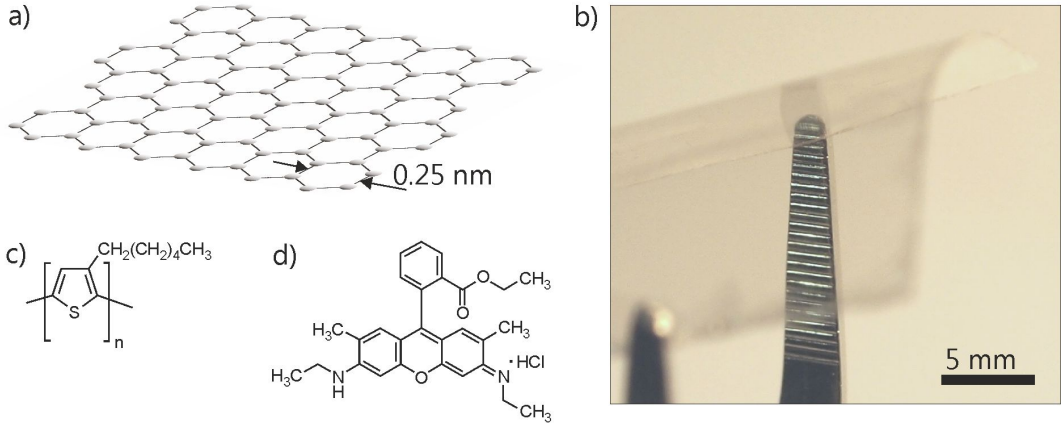

Figure 1.1. a) Cartoon of graphene. b) Photography of CVD-graphene on a mica substrate bent in a pair of tweezers indicating the high transparency of graphene. The graphene is not detectable with the naked eye, yet its coverage is indicated by microscopy (not shown). Sample kindly provided by Khaled Parvez from the graphite group at the Max Planck Institute for Polymer Research in Mainz, Germany. c) and d) Chemical structure of poly(3-hexylthiophene) [16] and, respectively, rhodamine 6G [17]. The conjugated bonds result in electrons delocalized across the molecules, capable of charge transport and light absorption and emission.

However, organic devices suffer from ubiquitous degradation by water and oxygen from the ambient atmosphere.[18-20] Currently the degradation of organic devices is reduced by encapsulation with glass [21] and composite barrier layers [22,23]. This thesis addresses whether graphene can not only be used as window electrode but

simultaneously as a transparent permeation barrier layer to protect organic devices from degradation. To quantify the barrier properties of graphene a method is developed, that allows to monitor the water vapour and oxygen transmission rates and the photo-chemical degradation kinetics of graphene *in-situ* on an organic conjugated polymer film (poly(3-hexylthiophene), see Figure 1.1c).

Besides graphene's potential application as electrode, it is an interesting quasi two-dimensional system. Microscopically small graphene flakes exfoliated from graphite were isolated for the first time in 2004.[1,24] Alreday in 2010 Andre Geim and Konstantin Novolselov were awarded with The Nobel Prize in Physics "for groundbreaking experiments regarding the two-dimensional material graphene". It was demonstrated, that graphene exhibits pseudo relativistic transport of electrons resulting from the linear band dispersion at low energies [25] previously predicted by Wallace in 1947 [26], the anomalous quantum Hall effect even at room temperature [25] and a visual transparency defined by fundamental constants [2]. These findings are characteristic for two-dimensional Dirac fermions, resembled by electrons in graphene near the Dirac point.[2,25,27] It is interesting to note that investigations focussing on graphene's properties are yet mostly performed on graphene mechanically exfoliated from graphite, still seeming to be the best source for graphenes of highest quality.

A current hot topic is graphene plasmonics, density oscillations of graphene electrons, bearing high potential for nano-optical applications. So far direct optical excitation of graphene plasmons has been demonstrated only in the infrared.[28-31] Yet, accelerated electrons have been shown to support even the high wavevectors necessary for graphene plasmon excitation in the visible [32,33] implying also optical excitability of graphene plasmon in the visible. Still graphene is assumed to be plasmon inactive at optical frequencies.[29,34,35] Also for this reason it is controversially discussed in literature, whether graphene is suitable for surface enhanced Raman spectroscopy.[35-37] To gain further insight in this fields, this thesis also addresses the impact of graphene on optical emitters in its proximity. The fluorescence and Raman emission of organic emitters (rhodamine 6G, see Figure 1.1d) in graphene's proximity is investigated and coupling meachanisms between graphene and emitters are discussed.

The basis for sample preparation in this thesis was provided in cooperation with colleagues: Methods were developed, that allow reliable identification and largely defect free fabrication of graphenes on transparent substrates. Furthermore this thesis includes the assembly of a setup for locally and spectrally resolved absorption, fluorescence and Raman investigation of molecular films down to submonolayer thickness.

In the following the fundamentals of graphene and its interaction with dipolar emitters will be introduced. These are used as the basis for the interpretation of the results in the main part of this thesis.

2 Fundamentals

2.1 Graphene

2.1.1 Structural and electronic properties

The tetravalence of carbon, the participation of the outer four electrons in formation of chemical bonds, makes the large number of occurring carbon-based systems possible.[38] Graphene is the two-dimensional allotrope of carbon in which the carbon atoms are arranged in covalently bonded hexagons (see Figure 2.2a). Graphite, the three-dimensional form of graphene, consists of parallel aligned graphene layers and exhibits a hexagonal crystal structure, i.e. the B-atoms (see Figure 2.2a) are centered above or, respectively, below the hexagons of the adjacent layers (AB-stacked). The layers have an interlayer distance of 0.335 nm (ref. [39]) and define the so-called basal planes of graphite.[38,40]

Figure 2.1 shows photographies of natural graphite flakes with visible triangular and parallelogram-like patterns primarily defined by internal angles of 60° and 120°. The visible pattern results from light scattering at the edges of the basal planes of the crystallites.

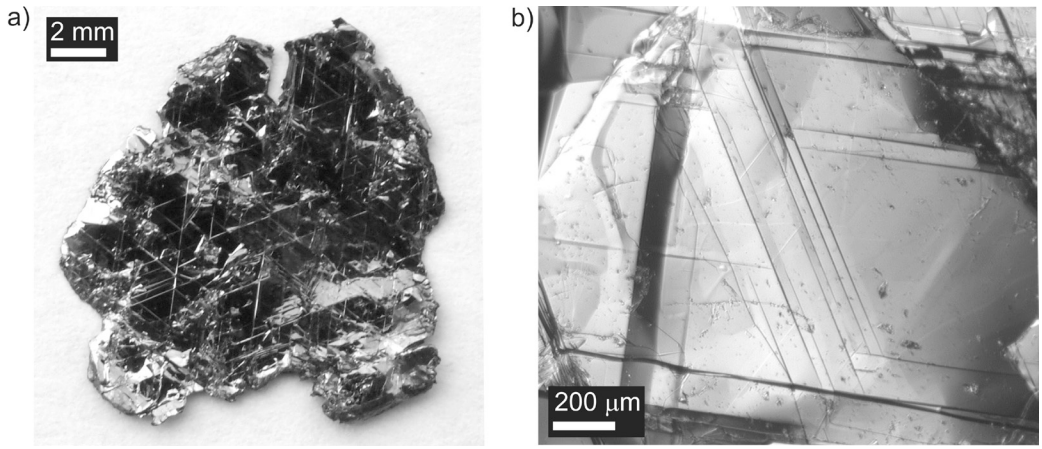

Figure 2.1. a) Photography of a natural graphite flake (purchased from NGS Naturgraphit GmbH) taken with a Olympus Pen E-PL1 camera equipped with a M.Zuiko Digital 14-42mm object lens at diffused illumination. Some edges of millimeter sized crystallites appear bright due to light scattering. b) Reflection microscopy image of a graphite flake, higher magnification than in a). Image was taken with Zeiss Axio Lab.A1 equipped with an EC Epiplan 5x/0.13 object lens and a EHD UK1157 CCD camera. Edges of the crystallites appear here dark, since the sample was illuminated through the object lens.

The in-plane bonds within the graphene layers are formed by sp^2 hybridized orbitals, originating from the 2s, the $2p_x$ and the $2p_y$ valence orbitals of the carbon atoms. The binding energy of these in-plane σ-bonds amounts to 615 kJ/mol and is reason for the high mechanical and chemical stability of graphene.[38] The interplane binding energy of the π-bonds between the graphene layers generated by the remaining $2p_z$ orbitals oriented perpendicular to the basal plane is much weaker and allows the "simple" fabrication of atomically thin graphene layers from graphite by mechanical exfoliation (microscopy image of graphene given in next the chapter, Figure 2.3).[38]

The hexagonal lattice of graphene yields a unit cell defined via the basis lattice vectors a_1 and a_2. The distance of the two atoms A and B in the unit cell is $a \approx 0.142$ nm and with this the length of the lattice vectors can be written as (see Figure 2.2a):[26]

$$|a_1| = |a_2| = \sqrt{3}\, a\,. \qquad \text{Eq. 2.1}$$

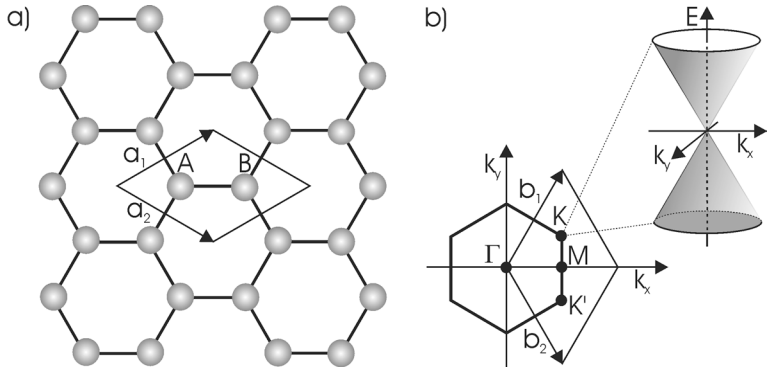

Figure 2.2. a) Hexagonal lattice structure of graphene with the carbon atoms at the corners of the hexagons. The basis lattice vectors a_1 and a_2 mark the unit cell containing two nonequivalent atoms A and B. b) Hexagonal Brillouin zone of graphene and reciprocal lattice vectors b_1 and b_2. The letters Γ, M, K and K' mark the symmetry points of the reciprocal lattice with the Dirac cones of the electronic band structure being located at the K and K' points, resulting from the A and B sub-lattices.[41]

Graphene's electronic band structure can be approximated with the tight binding model (TBM). This model assumes that the crystal lattice is defined by the in-plane σ-bonds formed from three of the valence electrons. The fourth valence electron occupies the $2p_z$ orbital, which is oriented perpendicular to the plane of graphene and forms delocalized π-orbitals with the neighbouring $2p_z$ orbitals.[38] Thus the interaction with the σ-bonds can be neglected and consequently it is assumed that the

electronic properties can be described by the π-electrons only. Furthermore the unit cell of graphene is divided into two triangular sub-lattices which are generated by the A and B atoms, respectively, and contain a single electron only.[26] This justifies the treatment of the electronic properties of graphene by a single electron per atom confined in a quasi 2-dimensional hexagonal lattice (Figure 2.2b).[26,38] The resulting energy bands can be calculated using the Schrödinger equation. The Hamiltonian H can be written as sum of the Hamiltonian H_0 of an isolated carbon atom and the periodic potential V of the lattice [26]:

$$H = H_0 + V - U\,, \qquad \text{Eq. 2.2}$$

with U being the potential field of an isolated carbon atom. Using the symmetry of the hexagonal lattice and considering only interaction between the electrons of nearest neighbour atoms the square of the absolute value of the Hamiltonian can be written as [26]:

$$\left|H\right|^2 = \gamma_0^2\left(1 + 4\cos^2 \pi k_y a + 4\cos \pi k_y a \cos k_x \sqrt{3}a\right), \qquad \text{Eq. 2.3}$$

with γ_0 being the exchange (overlap) integral between nearest neighbours, which takes interactions between the two sub-lattices into account. The integral takes a value between 2.5 eV and 3 eV.[42] Expanding the solution for the dispersion relation near the corners of the Brillouin zone (K points), at which conduction and valence band meet, results into [26,38]:

$$E(k) \approx \sqrt{3}\pi\gamma_0 a\left|k - K\right| = \hbar v_F \left|k - K\right|, \qquad \text{Eq. 2.4}$$

with v_F being the Fermi velocity, the group velocity of the electrons, which is about 10^6 ms^{-1}.[25] This is the well-known form of the dispersion relation of graphene, showing a linear relation between E and k (Dirac cone approximation). Since therefore electrons in graphene near the K point fulfill the Dirac-equation for massless particles, the K points are called Dirac points at which the electrons show pseudo-relativistic behaviour (linear dispersion) [41].

The density of electronic states can be calculated by integrating $(\mathrm{d}E/\mathrm{d}k)^{-1}$ over a curve s of constant energy E [26]:

$$N(E) = 2A\int \frac{ds}{|dE/dk|}, \qquad \text{Eq. 2.5}$$

with A being the area of the lattice (e.g. area of the unit cell). From this one can predict within the Dirac cone approximation a vanishing density of states at the Dirac point K along with a vanishing effective mass of the electrons and for $k \neq K$ a density of states increasing linear with the absolute value of the energy E.[26,41] Graphene can be described as a zero bandgap semiconductor or a semimetal, respectively, since conduction and valence band meet at the Dirac point (point of vanishing density of states).[38,41]

First evidence for Dirac fermions near the Dirac point in graphene was given by measurement of the Schubnikow-de Haas effect and the anomalous quantum Hall effect (detectable even at room temperature) in graphene. The derived carrier concentration dependent cyclotron mass in graphene indicated linear energy-momentum dispersion. Extrapolation of the data further indicates a vanishing effective mass at the Dirac point.[25]

Another feature of an electronic system with linear dispersion is, that it should exhibit a minimum conductivity of $4e^2/\pi h$.[43] However, the measured minimum conductivities are at least $\sim\pi$ times greater.[4,25] The origin is still under discussion but, resulting from graphene's quasi 2-dimensionality, might be due to its electronic properties being sensitive to the environment (rippling, dopants etc.).[4,44]

The next chapter will treat the optical properties of graphene, which can be related to its electronic properties [27].

2.1.2 Optical properties

The optical properties of graphene, in particular its absorption, can be linked to graphene's dynamic (optical) conductivity.[2,27]

In ideal graphene (massless Dirac fermions) optical interband transistions generated by a photon with energy $\hbar\omega$, i.e. the excitation of an electron from the lower Dirac cone at $-\hbar\omega/2$ to the upper Dirac cone at $\hbar\omega/2$ (inset in Figure 2.3a) yield the real part of the optical conductivity:

$$\sigma(\omega) = \frac{\pi e^2}{\omega} |v(\omega)|^2 D(\omega) \left[f\left(-\frac{\hbar\omega}{2}\right) - f\left(\frac{\hbar\omega}{2}\right) \right], \qquad \text{Eq. 2.6}$$

with v being the velocity matrix element, D the joint density of states and f the Fermi-Dirac distribution. If only interaction between the electrons of nearest neighbour atoms is taken into account (see last chapter) the optical conductivity is given by fundamental constant yielding the universal conductivity $\sigma_0 = e^2/4\hbar$, which is the dynamic conductivity of Dirac fermions.[27]

For normal light incidence the optical transmittance of a material with conductivity σ can be written as [2,27]:

$$T = \left(1 + \frac{2\pi}{c}\sigma\right)^{-2} \approx 1 - \frac{4\pi}{c}\sigma, \qquad \text{Eq. 2.7}$$

with c being the speed of light. As light reflection by a thin film like graphene can be neglected (reflection goes to zero for infinitely thin thickness) [45] this yields an absorption $A \approx 1 - T$. Within the Dirac cone approximation this gives a frequency independent value for the absorption defined by fundamental constant only equal to $\pi\alpha$, with α being the fine-structure constant.[27] This corresponds to an absorption of 2.3%, which was experimentally confirmed in the green and red wavelength range by transmission microscopy of free standing graphene (Figure 2.3a).[2] However, the Dirac cone approximation underestimates the absorption already in the blue wavelength range, which is not surprising as the Dirac cone approximation is only valid for small energies.[2]

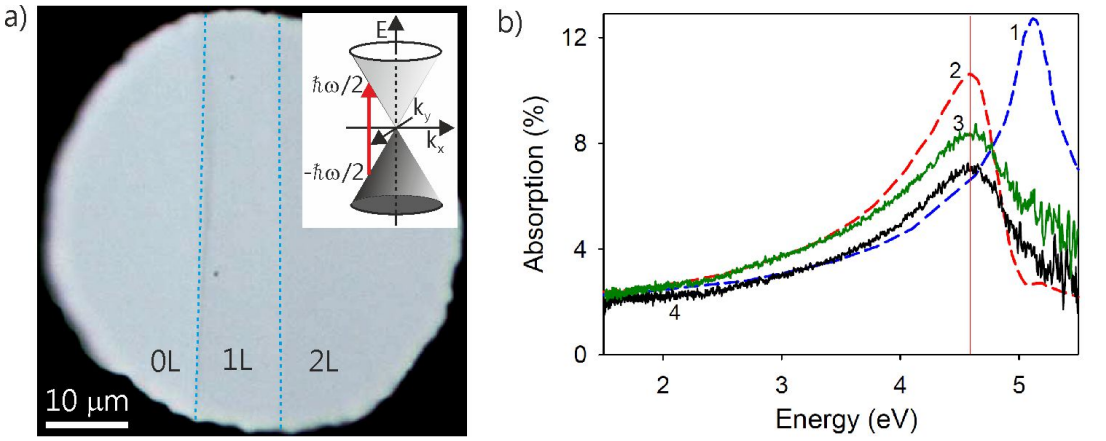

Figure 2.3. a) Transmission microscopy image of an aperture partially covered by single (1L) and double layer graphene (2L), uncovered regions are marked as (0L). The change in transmission induced by single layer graphene corresponds to a visual absorption of 2.3%. From Nair, R.R. et al., Fine structure constant defines visual transparency of graphene, Science 320, 1308 (2008). Reprinted with permission from AAAS. Inset: Absorption of a photon with energy $\hbar\omega$ by graphene through excitation of an electron from a filled valence band state (lower Dirac cone) into an empty conduction band state in the (upper Dirac cone). b) Absorption of graphene on quartz substrate (black and green curve are lower and upper limits of the experimental data, respectively) and calculated absorption of graphene with (red curve) and without (blue curve) including many-body interactions. From arXiv:1003.2618, also published as Kravets,V.G. et. al., Spectroscopic ellipsometry of graphene and an exciton-shifted van Hove peak in absorption, Physical Review B 81, 155413 (2010).

Nevertheless, even beyond the Dirac Cone approximation, the TBM still underestimates the absorption in the blue wavelength range.[2] Furthermore the peak absorption of graphene, predicted by TBM being at 5.2 eV, is blue shifted by 0.6 eV to the experimentally value of 4.6 eV (Figure 2.3b, for graphene on solid substrate as well as freely suspended) [45,46].

The deviation of the experimental absorption from the value predicted by the TBM might result from adsorbates, which itself absorb light, or result in doping of graphene.[2] Effects like doping can not be taken into account by the TBM, since it is a simplified one-electron model [26] and neglects many body effects like electron-electron and electron-hole interactions [47]. The consideration of doping requires a modified, perturbated Hamiltonian $H' = H + H_1$, with H_1 accounting for electron-electron interaction and a subsequent modified interaction between electrons and the ionic cores. These interactions can be approximated by an effective electron-electron interaction, which is known as the random phase approximation (RPA).[48,49] Using the local random phase approximation (small wavevectors, e.g. relevant for optical spectroscopy) the dynamic conductivity of graphene becomes [34,49]:

$$\sigma(\omega) = \frac{e^2 E_F}{\pi\hbar^2}\frac{i}{\omega + i\tau^{-1}} + \frac{e^2}{4\hbar}\left[\theta(\hbar\omega - 2E_F) + \frac{i}{\pi}\log\left|\frac{\hbar\omega - 2E_F}{\hbar\omega + 2E_F}\right|\right], \quad \text{Eq. 2.8}$$

with τ being the relaxation time of the electrons and E_F being the Fermi level shift, e.g. due to doping. The first term accounts for intraband transitions, which become possible due to a Fermi level shift induced population of the upper Dirac cone with electrons. At the same time the part of the conductivity resulting from interband transitions (terms in the brackets) is modified.[41] For transitions well below an energy of $2E_F$ the real part of the conductivity is predicted to be orders of magnitude below the value deduced from the Dirac cone approximation (σ_0) and simultaneously an imaginary part of the conductivity (out-of-phase response) [50] occurs, which can even be larger than σ_0. On the other hand for transitions with energy well above $2E_F$ and for undoped graphene the local random phase approximation converges against the Dirac cone approximation. However, even for strong doping levels the modification of the conductivity in the visible spectral range is expected to be small and the imaginary part is always much smaller than the real part of the conductivity. The predicted results do even not alter strongly using the nonlocal RPA.[34] Additionally, it should be noted that the tight binding model predicts at visible frequencies even beyond the Dirac cone approximation (integration over the full Brillouin zone) an imaginary part of the dynamic conductivity orders of magnitude smaller than the real part.[51]

Thus neither TBM nor RPA can explain the absorption of graphene beyond the green wavelength range. It should be noted that RPA as used in Eq. 2.8 is still a strongly simplified model, as it uses TBM as a basis and introduces electron-electron interaction by an effective interaction (linear response theory) [48]. In the undoped case many body effects are still neglected.

However, *ab initio* calculations, e.g., by means of the Kohn-Sham equation (density functional theory (DFT)) [52] and Bethe-Salpeter equation (BSE) [47] are nonlinear approaches (interactions between electrons and cores depend on the electron density

itself) [52] which allow to include man-body effects like electron-electron and electron-hole interaction in graphene also in the undoped case. The calculated absorption of graphene is in good agreement with the absorption of graphene on solid substrate in the visible spectral range and with the absorption peak in the ultra violet at 4.6 eV (Figure 2.3b).[45,47] The peak in the ultraviolet can be interpreted as a coupled excitation of plasmons and excitons.[33,53]

DFT also allows to calculate the complex dielectric constant of graphene. While the bandstructure of graphene near the Dirac point (small energies) predicted by DFT is in good agreement with the Dirac cone approximation and the experimental bandstructure, the dielectric response of graphene in the visible spectral range (higher energies) calculated by DFT is rather similar to that of graphite (not resembling Dirac fermions).[54] The dielectric constant of graphene can be converted into its optical conductivity, using that the relation between relative permittivity ε and susceptibility χ is given by $\varepsilon = 1 + \chi$ and between susceptibility χ and conductivity σ by $\chi = -\sigma / i\omega\varepsilon_0 d$ (ref. [27,55,56]):

$$\sigma = i\omega\varepsilon_0 d(\varepsilon - 1), \qquad \text{Eq. 2.9}$$

with d being the thickness of the graphene layer. Using this equation DFT predicts even in the undoped case real and imaginary part of graphene's conductivity in the visible spectral range to be both on the order of σ_0 (1.4 + 0.8i at 550 nm in units of σ_0) [54,56] in contrast to TBM and TBM based RPA. This behaviour can be explained by significant contributions to the imaginary part of the conductivity from transitions between the π- and σ-states along the high symmetry line between the Γ and M points, in contrast to the prediction by TBM, being dominated by transition only in the vicinity of the K points.[54,56] However, it should be noted that DFT overestimates the real part of the conductivity, better agreement with experimental real part is achieved by BSE.[47]

The calculated complex dielectric constant of graphene using DFT can also be compared to the experimental refractive index of graphene verified by picometrology [57] using that the refractive index n is related to the relative permittivity ε by $n^2 = \varepsilon$ for a permeability μ close to unity. Converting the experimental dielectric constant

further into the conductivity (Eq. 2.9), gives an experimental complex conductivity of $0.8 + 0.6i$ (in units of σ_0) at 532 nm.[56,57] As predicted by DFT real and imaginary part of graphene's experimental conductivity are on the same order which shows that TBM and TBM based RPA do not sufficiently describe graphene's optical properties in the visible spectral range,[54,56] since they do not include many body interactions in the undoped case.

However, it should be noted that the real part of graphene's conductivity derived from the experimental refractive index of graphene verified by picometrology is below the conductivity derived from the absorption of freely suspended graphene [2]. This very likely results from an experimental error of the picometrology measurement. Better agreement of the real part of the conductivity derived from the refractive index of graphene with the conductivity derived from the absorption of freely suspended graphene is achieved with the refractive index of graphene verified by ellipsometry [45,58] (see ref [58] and discussion part of this thesis). Additionally it should be noted that there is no contradiction between the real part of graphene's conductivity derived from graphene's absorption [2] and the complex conductivity derived from graphene's refractive index, since absorption measurements are rather insensitive to the imaginary part of graphene's conductivity.[56]

Both real and imaginary parts of the conductivity are important for the properties of plasmons in graphene, which will be treated in the next chapter.

2.1.3 Plasmons in Graphene

Surface plasmons are collective oscillations of the surface charge at the interface between a dielectric and a conductive medium, e.g. a bulk metal. The coupled excitation of photons and plasmons is called surface plasmon polaritons. Surface plasmons can be described as a *p*-polarized electromagnetic wave located at an interface, the electric field E has the form [59]:

$$E = \begin{pmatrix} E_x \\ 0 \\ E_z \end{pmatrix} \exp(ik_x x - i\omega t)\exp(ik_z z), \qquad \text{Eq. 2.10}$$

with k_x and k_z being the wavevector components along the interface and perpendicular to the interface, respectively. The localisation of the field to the interface is characterized by an exponential decay of the electric field with increasing distance z to the interface being located at $z = 0$. Along the interface (x-direction) it has an oscillatory character.

The wavevector of surface plasmons is always larger than the wavevector of free space photons (smaller group velocity) and they are capable to propagate along interfaces. Energy and momentum of surface plasmons are related through the plasmon dispersion relation which dependends on the geometry and material parameters of the conducting and dielectric media at the interface.[59], [34,60]

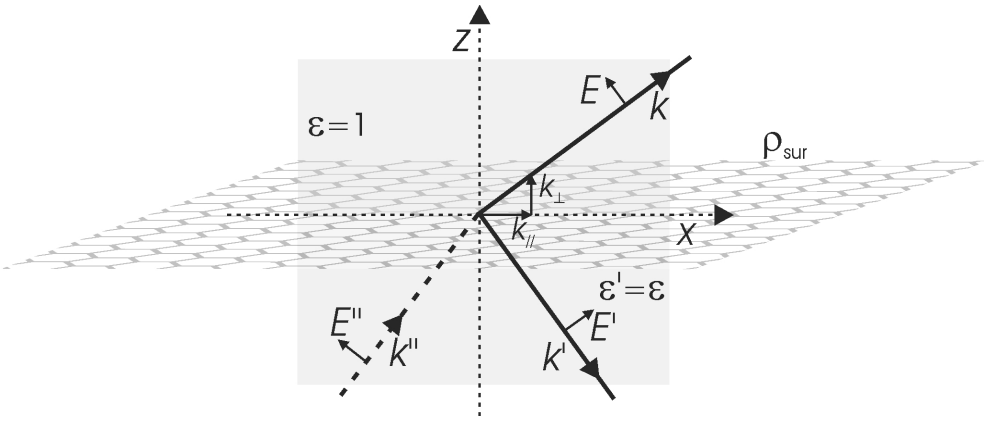

Figure 2.4. Sketch of an interface between two dielectric media with dielectric constants 1 and ε, respectively. The quasi 2-dimensional conducting layer graphene is located at z = 0 and described as a surface charge ρ_{sur}. The p-polarized fields inside the substrate with dielectric constant ε are denoted as *E*'' (incident) and *E*' (reflected), the field of the diffracted wave outside the substrate is denoted as E. The wavevector *k* may be splitted into its components polarized parallel ($k_{//}$) and perpendicular ($k_\perp$) to the interface. Surface plasmons are characterized by the disappearance of the incident or reflected electric field, here the incident electric field *E*'' (eigenmode of the system).

Plasmons are not only limited to the surface of a bulk conductor, they may also exist near quasi 2-dimension conducting films like graphene.[34,60] In the following the derivation of the surface plasmon dispersion relation and the required material parameters for the existence of plasmons near quasi 2-dimensionl conducting film will be summarized based on ref. [34] and [59].

Since plasmons are an interface phenomenon with reactive character the plasmon dispersion relation can be related to the optical response of graphene. In particular it can be derived from the pole of the reflection coefficient *r* of graphene (vanishing denominator, r = *E*'/*E*'') for waves polarized parallel to the plane of incidence,[34] i.e. vanishing of the incident electric field component *E''* (see Figure 2.4). This means that plasmons are eigenmodes of the system, i.e. they exist without external excitation.[59] In the following, the reflection coefficient of graphene will be derived from the boundary conditions of the field components at the interface.

From continuity of the electric field components $E_{//}$ parallel and the magnetic induction $B_{\perp}$ perpendicular to graphene Maxwell's first and fourth equations yield [59]:

$$\Delta E_{//} = 0 \text{ and } \Delta B_{\perp} = 0 . \qquad \text{Eq. 2.11}$$

If the interface is covered with a surface charge ρ_{sur}, Maxwell's third equation yields the following boundary condition of the perpendicular component of the electric field displacement $D_{\perp}$ [59]:

$$\Delta D_{\perp} = \rho_{sur} , \qquad \text{Eq. 2.12}$$

with the electric field displacement *D* being related to the electric field *E* by the vacuum permittivity ε_0 and the corresponding dielectric constant ε of the medium at the interface [59]:

$$D_{\perp} = \varepsilon_0 \varepsilon E_{\perp} . \qquad \text{Eq. 2.13}$$

Assuming time harmonic fields with an oscillation frequency ω, i.e. $E(r,t) = \mathrm{Re}[E(r) \exp(-i\omega t)]$,[59] the time derivative of Eq. 2.12 can be written as:

$$-i\omega\Delta\varepsilon_0\varepsilon E_{\perp} = \frac{d}{dt}\rho_{sur} . \qquad \text{Eq. 2.14}$$

Using furthermore that the time derivative of the surface charge ρ_{sur} is related to the current j by (continuity equation) [59]:

$$\frac{d}{dt}\rho_{sur} = -\nabla \cdot j \qquad \text{Eq. 2.15}$$

and that the current j is related to the electric field E by the surface conductivity σ ($j = \sigma E_{//}$),[59] Eq. 2.14 can be rearranged to [34]:

$$\Delta\varepsilon_0\varepsilon E_\perp = \frac{\sigma}{i\omega}\nabla \cdot E_{//}. \qquad \text{Eq. 2.16}$$

With these equations the reflection coefficient r_p for waves polarized parallel to the plane of incidence can be written as [34]:

$$r_p = \frac{\varepsilon k_\perp - k_\perp' + \sigma k_\perp k_\perp' / \varepsilon_0\omega}{\varepsilon k_\perp + k_\perp' + \sigma k_\perp k_\perp' / \varepsilon_0\omega}, \qquad \text{Eq. 2.17}$$

with $k_\perp$ and $k_\perp'$ being the wavevectors perpendicular to graphene outside and, respectively, inside the substrate. Using that $k_\perp = \sqrt{k_0^2 - k_{//}^2}$, with $k_{//}$ being the wavevector parallel to graphene and $k_0 = \omega/c$ being the wavevector of free space photons, i.e. splitting of the wavevector of the *p*-polarized wave into its components parallel and perpendicular to graphene (see Figure 2.4), the pole of the reflection coefficient is given by the following equation [34]:

$$\varepsilon / \sqrt{k_0^2 - k_{//}^2} + 1 / \sqrt{k_0^2 - k_{//}^2} = -\sigma / \varepsilon_0\omega. \qquad \text{Eq. 2.18}$$

Using $k_{sp} = k_{//}$ and assuming $k_0 << |k_{sp}|$ the surface plasmon dispersion relation for quasi 2-dimensional plasmons can be written as [34,60]:

$$k_{sp} \approx i(\varepsilon + 1)\varepsilon_0\omega/\sigma. \qquad \text{Eq. 2.19}$$

An oscillating surface wave requires a finite real part of the plasmon wavevector k_{sp}, which is only given for a non vanishing imaginary part of the conductivity of graphene.[61] Furthermore the imaginary part of the wavevector reflects the in-plane decay length of the plasmon, which is large for a small real part of the conductivity.[34]

Efficient excitation of plasmons by photons requires match of energy and momentum of the photons to the plasmons, i.e. the momentum of the photons must be increased compared to its free space value. A prominent example is the use of the near-field generated by total internal reflection at the interface of a prism.[59] However, in graphene plasmons are hardly excitable through the near field generated by total internal reflection, since the wavevector mismatch exceeds an order of magnitude. However, it has been suggested that graphene plasmons are excitable by small dipole emitters, like fluorescent molecules and scattering metal tips.[34] In the mid-infrared metal tips have been demonstrate to efficiently excite graphene plasmons.[28,29] Furthermore, the graphene plasmon resonance in the ultraviolet was shown to enhance the fluorescence of a semiconducting film.[62] Additionally electron energy loss spectroscopy (EELS) was used to verify the dispersion curve of graphene plasmons excited by accelerated electrons.[32,33] It could be shown by EELS that the frequency of the plasmon is roughly increasing with the square root of the wavevector, a dispersion expected from a two dimensional electron gas rather than from massless Dirac fermions.[32,33]

The dispersion of graphene plasmons in the visible spectral range expected from graphene's refractive index [45,58] and their excitation will be treated in the discussion part of this thesis.

The next chapter will treat light-matter interaction including interaction with plasmons.

2.2 Light-matter interaction

The following chapters are mainly summarized from Novotny, L. & Hecht, B., *Principles of Nano-Optics*, Cambridge (2006) (ref. [59]). They cover the properties of the radiation of an emitter within the point dipole approximation and light-matter interaction on the nanoscale.

2.2.1 Near- and far-field of a dipolar emitter

Within a microscopic picture a particle or molecule can be considered as a set of discrete charges q_n with the position vector of the nth charge being denoted as r_n (Figure 2.5).

Assuming that the charge distribution can be polarized by a time dependent external field, the electric dipole moment p of the charges mowing around the origin r_0 can be written as [59]:

$$p(t) = \sum_n q_n [r_n(t) - r_0]. \qquad \text{Eq. 2.20}$$

Higher order moments (e.g. quadrupole moments) are not considered in the equation above, however, the equation provides for small emitters (e.g. single molecules) sufficient accuracy [63,64].

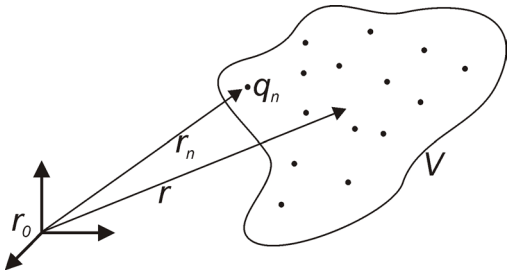

Figure 2.5. A dipole results from the movement of charges q_n with coordinates r_n. The charge distribution can also be expressed by a center coordinate r. Sketch according to reference [59].

The movement of the charges will generate a current which can be derived from the time derivative of the dipole moment. By developing the derivative around the origin r_0 and describing the response of the charges q_n as a collective response with center r the current density j can be approximated to [59] :

$$j(r,t) = \frac{d}{dt} p(t)\delta[r - r_0]. \qquad \text{Eq. 2.21}$$

By further assuming a harmonic time dependency of the charge oscillation which gives [59]:

$$p(r,t) = \mathrm{Re}[p\ \exp(-i\omega t)], \qquad \text{Eq. 2.22}$$

with ω being the frequency of the charge oscillation, the current density j can be rewritten as [59]:

$$j(r) = -i\omega\, p\delta[r - r_0]. \qquad \text{Eq. 2.23}$$

This equation is the current density of an emitter within the point dipole approximation. The current density can be related to its radiated fields as follows.

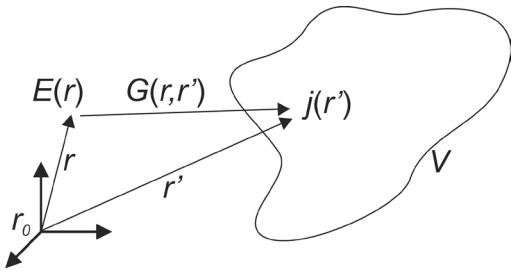

Figure 2.6. The Green's function G relates the field E at the point r to a point source at the point r'. V is the source volume of the current density j. Sketch according to reference [59].

Using the dyadic Green's function $\overleftrightarrow{G}$, which renders the electric field at the point r to a current density at the point r' (Figure 2.6), the electric and magnetic fields E and H, respectively, radiated in linear, isotropic and homogeneous space are derived to [59]:

$$E(r) = E_0 + i\omega\mu\mu_0 \int_V \overleftrightarrow{G}(r,r')j(r')dV', \qquad \text{Eq. 2.24}$$

$$H(r) = H_0 + \int_V \left[\nabla \times \overleftrightarrow{G}(r, r') \right] j(r') dV' , \qquad \text{Eq. 2.25}$$

with E_0 and H_0 being the fields in absence of the current density, μ_0 and μ the magnetic permeabilities of vacuum and of the considered medium, respectively, and V being the source volume of the current density. Introducing the current density from Eq. 2.21 the fields can be rewritten as:

$$E(r) = \omega^2 \mu \mu_0 \overleftrightarrow{G}(r, r_0) p , \qquad \text{Eq. 2.26}$$

$$H(r) = -i\omega \left[\nabla \times \overleftrightarrow{G}(r, r_0) \right] p . \qquad \text{Eq. 2.27}$$

The dyadic Green's function of a single dipole (point source) in homogeneous space is given by [59]:

$$\overleftrightarrow{G}(r, r_0) = \left[\overleftrightarrow{\mathrm{I}} + \frac{1}{k^2} \nabla \nabla \right] G(r, r_0), \; G(r, r_0) = \frac{\exp(ik|r - r_0|)}{4\pi |r - r_0|}, \qquad \text{Eq. 2.28}$$

where I is the unit dyad and G the scalar Green's function, the wavevector k is defined by $k = (\omega/c)n$ with c the speed of light in vacuum and n the refractive index. The scalar Green's function is part of a particular solution for the time-harmonic vector potential A in the Helmholtz equation, which can be derived from Maxwell's equations and the so-called Lorentz gauge. The inhomogeneous Helmholtz equation turns out to be [59]:

$$\left[\nabla^2 + k^2 \right] A(r) = -\mu_0 \mu \, j(r), \qquad \text{Eq. 2.29}$$

and the particular solution for the vector potential is:

$$A(r) = \mu_0 \mu \int_V G_0(r, r') j(r') dV' . \qquad \text{Eq. 2.30}$$

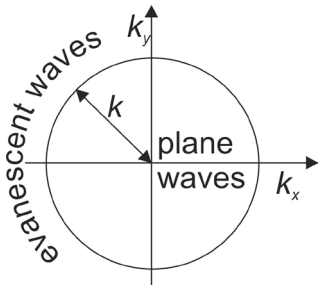

Figure 2.7. The wavevectors of plane waves are restricted to the circular area, those of evanescent waves to the space outside the area. A plane wave propagating in z-direction (out of the circle) has no oscillations in direction of the x- and y-axis, on the other hand the highest oscillations (largest wavevectors) of a plane wave propagating perpendicular to the z-axis are given by the radius of the circle. Evanescent fields with wavevectors larger than the circle exponentially decay in z-direction. Sketch according to reference [59].

The dyadic Green's function of the dipole has terms in $(kR)^{-1}, (kR)^{-2}, (kR)^{-3}$ where R is the absolute value of $(r - r_0)$. While in the far-field ($R >> \lambda$) only terms with $(kR)^{-1}$ are present, with the wavelength λ being related to the wavevector k by $\lambda = 2\pi/k$, the near-field is dominated by those with $(kR)^{-3}$.[59]

The strong decay of the near-field compared to the far-field results from its large wavecetors: Plane waves (e.g. in the far-field of a dipole) evaluated in an arbitrary plane $z = \text{const}$ are oscillating functions in z which wavevectors k (defined by $k^2 \equiv k_x^2 + k_y^2 + k_z^2$) are restricted to $k_x^2 + k_y^2 \leq k^2$; evanescent waves (near-field) are exponentially decaying along the z axis and their wavevectors fullfil $k_x^2 + k_y^2 \geq k^2$. This can be visualized by a circle with radius k, with the wavevectors of plane waves being restricted to the area within and those of evanescent waves to the area outside the circle (see Figure 2.7). Furthermore plane waves have no oscillations transverse to their propagation direction.[59]

The angular (wavevector) representation of the fields of a dipole oscillation along the z-axis (Figure 2.8**)** can be calculated from Eq. 2.28, using that the wavevector representation of $\exp(ikr)/r$ is given by the Weyl identity [65]:

$$\frac{\exp\left(ik\sqrt{x^2+y^2+z^2}\right)}{\sqrt{x^2+y^2+z^2}} = \frac{i}{2\pi}\int_{-\infty}^{\infty}\int\frac{\exp\left(ik_x x + ik_y y + ik_z|z|\right)}{k_z}dk_x dk_y, \qquad \text{Eq. 2.31}$$

with $r = (x^2 + y^2 + z^2)^{1/2}$.

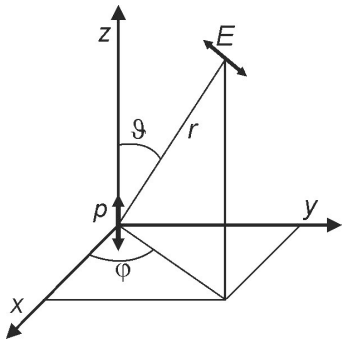

Figure 2.8. The field *E* of a dipole oscillating along the z-axis can be represented in spherical coordinates. While the near-field of a dipole contains accessible energy in any direction, there is no emission of energy into the far-field in direction of the dipole's oscillation (z-direction). Sketch according to reference [59].

Evanescent fields, characterized by a high field strength due to the high wavevectors (strong localisation), are for instance important for nonradiative energy transfer between emitters and absorbing media, which will be considered in chapter 2.2.3.

Finally the equations above can be used to derive the far-field radiation pattern (real space) of a dipole, here chosen to oscillate along the *z*-axis (Figure 2.8). Integration of the pointing vector, with the pointing vector given by *E* x *H*, over a closed spherical surface yields the time averaged radiated power *P*. The normalized power radiated into an infinitesimal small unit angle $d\Omega = \sin(\vartheta) d\vartheta d\varphi$ is in spherical coordinates evaluated to [59]:

$$\frac{P(\vartheta,\varphi)}{P} = \frac{3}{8\pi}\sin(\vartheta)^2 . \qquad \text{Eq. 2.32}$$

Most of the power is radiated perpendicular to the dipole axis and there is no radiation in direction of the dipole axis. This is, however, different for the near-field of the dipole (see above), even though the pointing vector in z direction is vanishing, evanescent fields contain accessible energy (see chapter 2.2.3).

While this chapter treated an emitter represented by the dipole approximation within a classical picture, the next chapter handles with the quantum mechanical description based on the transition dipole moment between a lower and a higher electronic state.

2.2.2 Spontaneous decay of excited emitters

In this chapter, the quantum mechanical picture of an oscillating dipole will be used to derive the spontaneous emission rate of a two-level quantum system, e.g. a fluorescent molecule. To preserve equilibrium of the emitting molecule and its environment, the description of its radiation (spontaneous decay) needs the inclusion of vacuum fluctuations and thus a quantum mechanical treatment. The used picture (classically or quantum mechanically) does not directly affect the radiated fields of the emitter. However, the interaction of radiation generated by spontaneous emission or, respectively, scattering (classically) with e.g. plasmons (chapter 2.2.4) requires a treatment dependening on the respective picture.

According to Fermi's Golden Rule [66] the transition rate γ form an initial state |i⟩ to a set of final state |f⟩ with frequencies ω_i and ω_f, respectively, (see Figure 2.9) is given by:

$$\gamma = \frac{2\pi}{\hbar^2}\sum_f \left|\langle f|\hat{H}_1|i\rangle\right|^2 \delta(\omega_i - \omega_f), \qquad \text{Eq. 2.33}$$

where $\hat{H}_1 = -\hat{p}\,\hat{E}$ is the interaction Hamiltonian in the dipole approximation with the dipole moment operator $\hat{p}$ and electric field operator $\hat{E}$, respectively. Eq. 2.33 can be rewritten as [59]:

$$\gamma = \frac{2\omega_0}{3\hbar\varepsilon_0}|\mathrm{p}|^2 \rho_\mathrm{p}(\mathrm{r}_0, \omega_0), \qquad \text{Eq. 2.34}$$

with $\omega_0 = \omega_i - \omega_f$, the transition dipole matrix element p and the partial local density of states ρ_p (related to the electric field, see below). The latter can be related to the imaginary part of the Green's dyadic function [59]:

$$\rho_p(r_0, \omega_0) = \frac{6\omega_0}{\pi c^2}\left[n_p \cdot \mathrm{Im}\{\overleftrightarrow{G}(r_0, r_0; \omega_0)\} \cdot n_p\right], \qquad \text{Eq. 2.35}$$

where n_p is the unit vector in direction of the dipole moment p. From a classical viewpoint the Green's dyadic is equivalent to the electric field emitted by the dipole

at a former time and arriving backs at its origin r_0 and with this Eq. 2.34 is equivalent to the rate of energy dissipation of the emitter.[59] Thereby the decay rate of the emitter can be modified (see next chapter).

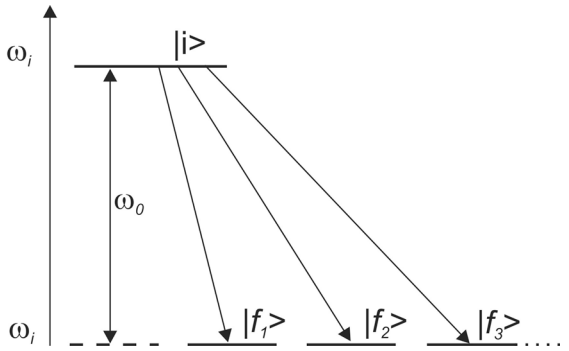

Figure 2.9. In the quantum mechanical picture the emission of a dipole can be described by a transition from an initial state |i⟩ to a set of final states |f⟩. The transition energy equals in all cases $\hbar\omega_0$. Sketch according to reference [59].

In homogeneous and isotropic environment the partial local density of states ρ_p is equal to the total local density of states ρ. In free space the total density of states ρ takes the value ρ_0 of [59]:

$$\rho_0 = \frac{\omega_0^2}{\pi^2 c^3}, \qquad \text{Eq. 2.36}$$

which is equal to the free space density of electromagnetic modes also used in the description of blackbody radiation.

Combining Eq. 2.34 and Eq. 2.36 the free space spontaneous decay rate γ_0 finally turns out to be [59]:

$$\gamma_0 = \frac{\omega_0^3 |p|^2}{3\pi\varepsilon_0 \hbar c^3}. \qquad \text{Eq. 2.37}$$

This shows that the square of the transition dipole matrix element p is proportional to the rate of spontaneous emission, which means that it is a dipole moment with fixed amplitude. In contrast the dipole moment within the classical picture (Eq. 2.20) is an induced dipole moment which amplitude depends on the excitation field (e.g. scattering).[52]

The decay rate of the excited state quantum system corresponds classically to the lifetime τ of an oscillating dipole, the time after which the dipole's energy has decreased to 1/e of its initial value, i e. in free space $\tau = 1/\gamma_0$.[59]

The decay rate of the emitter can be enhanced by its environment, which offers further decay channels and thus modifies the mode density, or, classically, increases the secondary dipole field (field scattered by the environment).

2.2.3 Fluorescence quenching

2.2.3.1 Nonradiative energy transfer

In this chapter the environmental induced nonradiative decay of an emitter will be treated. In the weak coupling regime classically and quantum mechanically treatment give identical results [59] and thus a classical treatment as in chapter 2.2.1 is chosen here. Examples for nonradiative decay in the weak coupling regime are energy transfer from a donor to an acceptor molecule and thermal dissipation of fluorescence emission near interfaces.[67-69]

In inhomogeneous environment the decay rate of an emitter or, respectively, the time average radiated power of a current distribution with harmonic time dependence can be modified. According to Poynting's theorem the latter is in a linear medium identical to the mean rate of energy dissipation dW/dt which is given by [59]:

$$\frac{dW}{dt} = -\frac{1}{2}\int_V \mathrm{Re}\left\{j^* \cdot E\right\} dV' , \qquad \text{Eq. 2.38}$$

with V being the source volume. In this case j is not the total current, but it represents either a source current that generates fields or a loss current resulting from thermal losses, e.g. loss currents induced in the environment (see also below). Inserting the expression for the current density of a point dipole (Eq. 2.23) Eq. 2.38 can be rewritten as [59]:

$$\frac{dW}{dt} = \frac{\omega}{2}\mathrm{Im}\{p^* \cdot E(r_0)\}, \qquad \text{Eq. 2.39}$$

with E being now the field at the dipole's origin. Using further the expression for the electric field generated by a current density (Eq. 2.26) dW/dt can be expressed in terms of the Green's function [59]:

$$\frac{dW}{dt} = \frac{\omega^3 |p^2|}{2c^2 \varepsilon_0 \varepsilon}\left[n_p \cdot \mathrm{Im}\{\overleftrightarrow{G}(r_0, r_0; \omega_0)\} \cdot n_p\right]. \qquad \text{Eq. 2.40}$$

The expression in the brackets is identical to that in the local density of states (Eq. 2.35). From a classical viewpoint the Green's dyadic is equivalent to the electric field emitted by the quantum system at a former time and arriving backs at its origin r_0, i.e. the density of states depends on the total local electric field $E = E_0 + E_s$, with E_0 being the primary dipole field and E_s the secondary field or the field scattered by the inhomogeneous environment.

In the case of energy transfer from donor to acceptor, the field E_s is sometimes denoted as the field of the donor and the current j is associated with charges of the acceptor. This means that the decay rate of the emitter in inhomogeneous environment can be modified (increased) compared to its free space value as the emitter interacts with its own scattered field (see Figure 2.10). The change of energy dissipation depends on the secondary dipole field and one can state [59]:

$$\gamma = \gamma_0 + \frac{2}{\hbar}\mathrm{Im}\{p_0^* E_s(r_0)\}. \qquad \text{Eq. 2.41}$$

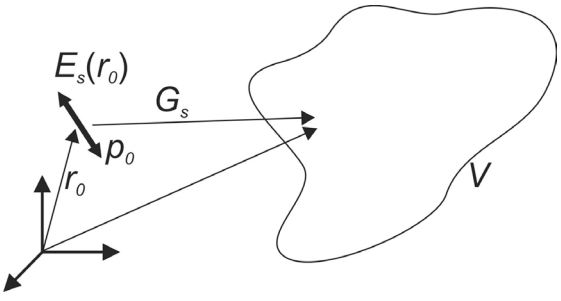

Figure 2.10. Interaction of a dipole p_0 with the field E_s scattered by the volume V. Sketch according to reference [59].

The equation requires that γ remains much smaller than ω, to ensure that the oscillation amplitude stays constant over one amplitude.[59]

The decay rate offered by the inhomogeneous environment through E_s (quantum mechanically: additional decay channels) may e.g. result in thermal dissipation of the energy; in the case of energy transfer between a spectrally overlapping donor and acceptor molecules the energy, nonradiatively transferred from donor to acceptor, can be radiatively reemitted by the acceptor.[68] Both results in quenching of the donor emission (see also below). To ensure that that the probability for backtransfer of the energy from acceptor to donor is small, transfer rates smaller than the vibrational relaxation rates of the molecules are required (weak coupling regime).[59]

Planar interfaces, e.g. graphene

For a planar interface the secondary dipole field E_s can be directly related to the Fresnel reflection coefficients r_s and r_p for *p*- and *s*-polarized waves, respectively and the distance z between emitter and interface. With this the total decay rate is derived to [34]:

$$\gamma = \gamma_0 + \frac{1}{\hbar}\int_0^\infty k_{//}\,dk_{//} \qquad \text{Eq. 2.42}$$

$$\mathrm{Re}\left\{\left[|p_{//}|^2\left(k_0^2 r_s - k_\perp^2 r_p\right) + 2|p_\perp|^2 k_{//}^2 r_p\right]\frac{\exp(2ik_\perp z)}{k_\perp}\right\},$$

where $p_{//}$ and $p_\perp$ are the dipole moments and $k_{//}$ and $k_\perp$ the wavevector components parallel and accordingly perpendicular to the interface. The equation can be explored in the electrostatic limit, which is accurate for distances z much smaller than the wavelength of the emission. Considering an interface to a quasi two-dimensional layer, like graphene, with optical conductivity σ and supported by a medium with dielectric constant ε the equation can be evaluated to [34]:

$$\gamma \approx \gamma_0 + \frac{2}{\hbar}\left(|p_{//}|^2 + 2|p_{\perp}|^2\right) \int_0^{\infty} k_{//}{}^2 dk_{//}\ \mathrm{Im}\left\{\frac{-1}{\varepsilon + 1 + 4\pi i k_{//}\sigma/\omega}\right\} e^{-2k_{//}z}\ , \qquad \text{Eq. 2.43}$$

with ω being the frequency of the emission. Division of Eq. 2.43 by the radiative rate $\gamma_r = 4k_0^3|p|^2/3\hbar$ (as given in ref. [34]) and cconsidering only dipoles oriented parallel to graphene yields the normalized total decay rate, as used in the results and discussion part of this thesis:

$$\gamma^g/\gamma_r = 1 + \frac{3c^3}{2\omega^3}\int_0^{\infty} k^2 dk\ \mathrm{Im}\left\{\frac{-1}{\varepsilon + 1 + 4\pi i k\sigma/\omega}\right\} e^{-2kz}\ . \qquad \text{Eq. 2.44}$$

The decay rate induced by the interface may result in thermal dissipation of the energy, or in conversion of the energy into evanescent fields at the interface. The integral in Eq. 2.44 may be separated into these contributions, the latter can be associated with excitation of surface plasmons.[34] In particular for dipoles oriented parallel to graphene, the plasmon contribution to the normalized decay rate in the graphene region γ^{sp}/γ_r can be calculated from the graphene plasmon wavelength λ_{sp}, which is related to the optical conductivity of graphene (see chapter 2.1.3) at the emission frequency ω of the emitter [34]:

$$\gamma^{sp}/\gamma_r \approx \frac{12\pi^4 c^3}{(\varepsilon+1)\omega^3}\frac{e^{-4\pi z/\lambda_{sp}}}{\lambda_{sp}{}^3}, \qquad \text{Eq. 2.45}$$

where c is the speed of light.

Quenching by graphene has been demonstrated for fluorescent quantum dots [70] and molecules [71]. There is however so far no theoretical description of quenching through graphene that agrees with all experiments. Quenching by graphene can thus

be considered to be still under discussion and will be addressed in the results and discussion part of this thesis.

Quantum yield

The quantum yield ϕ of an emitter is a measure of its radiative output and defined as [59]:

$$\phi = \frac{\gamma_r}{\gamma}, \qquad \text{Eq. 2.46}$$

with γ_r being the radiative decay rate, which denotes the emission radiated into the far-field. The radiative decay rate can be increased by the emitter's environment in the case that the decay channels offered by the environment transfer the energy into the far-field instead of thermal dissipation (calculation of the rates via Eq. 2.38). The total decay rate γ includes radiative and nonradiative decay channels, e.g. thermal dissipation. The lifetime τ of the excited state quantum system is related to γ by $\tau = 1/\gamma$, i.e. interaction of the emitter with its environment may yield to a strong reduction of its excited state lifetime.

2.2.3.2 Stern-Volmer quenching

The nonradiative decay of emitters induced by acceptor molecules can also be used to determine the acceptor concentration in the environment of an emitter. The relation between quencher (acceptor) concentration [Q] and fluorescence intensity of the emitter (donor) is given by the Stern-Volmer equation, which can be derived from the fluorescence quantum yield. Let $\phi_{[Q]}$ be the fluorescence quantum yield in presence of a quencher with concentration [Q] [72]:

$$\phi_{[Q]} = \frac{\gamma_r}{\gamma_r + \gamma_{nr} + \gamma_Q[Q]}, \qquad \text{Eq. 2.47}$$

with γ_r being the radiative rate, γ_Q being the decay rate induced by the interaction of emitter and quencher, and γ_{nr} being nonradiative decay induced through arbitrary other processes. Denoting ϕ_0 as the quantum yield and τ_0 as the fluorescence lifetime

in absence of the quenchers ($[Q] = 0$) and using that fluorescence intensity I is proportional to the fluorescence quantum yield ϕ one can write [72]:

$$\frac{I_0}{I_{[Q]}} = 1 + \gamma_Q \tau_0 [Q]. \qquad \text{Eq. 2.48}$$

This is the Stern-Volmer equation and it predicts a linear relation between $I_0/I_{[Q]}$ and the quencher concentration $[Q]$. $\gamma_Q \tau_0$ is called Stern-Volmer constant and needs to be determined for the each system of emitters and quenchers. The decay induced by the quenchers must not necessarily results from energy transfer to an acceptor but can also results from e.g. collisional quenching and complex formation.[72]

The Stern-Volmer equation and the Stern-Volmer constant of oxygen in P3HT [18] will be used in the results and discussion part of this thesis to determine the upper limits of the water vapour and oxygen transmission rates through graphene on top of a fluorescent P3HT film.

2.2.4 Plasmon induced excitation and emission enhancement

In the chapter 2.2.3 the modification of the emission rate through interaction of an emitter with its environment was considered. The derivations were based on the interaction of the emitter with its own emitted field, scattered by the environment. So far not considered was that the environment of the emitter can also modify the local excitation field of the emitter, which may yield to enhancement of the excitation rate. This and also enhancement of the radiative emission rate will be considered in the following. An example of combined excitation and emission enhancement is electromagnetic Raman enhancement of molecules through rough metal surfaces, particles and tips.[73-75]

Excitation enhancement

Classically (e.g. scattering) the dipole moment p is not a permanent dipole moment, but it is induced and can be related to its polarisability α and the local excitation field. The local excitation field consists of the incident field E_0 and the field E_s scattered by the environment (see Figure 2.11), for simplicity all quantities are assumed to be scalars [59]:

$$p(\omega_0,\omega)=\alpha(\omega_0,\omega)\left[E_0(r_0,\omega)+E_s(r_0,\omega)\right], \qquad \text{Eq. 2.49}$$

with ω_0 being the emission frequency of the emitter and ω the frequency of the local excitation field at the position of the emitter r_0. Both incident and scattered local fields have the frequency ω. E_s depends linearly on E_0 and the local excitation field can thus be written as [59]:

$$E(r_0,\omega)=E_0(r_0,\omega)+E_s(r_0,\omega)=(1+f)E_0(r_0,\omega), \qquad \text{Eq. 2.50}$$

with f designated as the local field enhancement factor. As the field E_R radiated by a dipole is proportional to the dipole moment (Eq. 2.26), the local field enhancement f yields an enhancement of the energy emitted by the dipole proportional to f^2. Large field enhancement factors are generally only achieved locally through energy confinement to e.g. interfaces or hot spots [73,76].

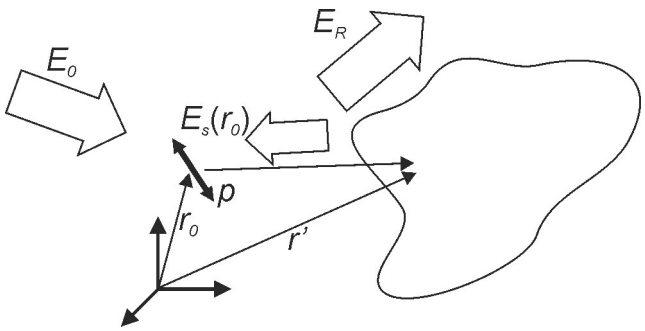

Figure 2.11. A dipole can be induced by both the incident field E_0 and the field E_s scattered by the environment (coordinate r'). This may yield to enhancement of the field E_R radiated into the far-field. Sketch according to reference [59].

Emission enhancement

Similar to the excitation rate (energy) also the decay rate (emitted energy) of an emitter can be enhanced through the environment. As discussed in chapter 2.2.3.1 scattering of the dipole's own emitted field by the environment yields a decay rate enhancement (Eq. 2.39). The offered decay channels are here, however, assumed to be primarily of radiative nature. A qualitative description of the radiation enhancement factor f is given by Eq. 2.50, by replacing ω with the emission frequency of the scattered field ω_0.[59]

The theory for emission enhancement applies to Raman scattering and fluorescence emission. However, for fluorescence emission, due to the nature of the quantum mechanically transition dipole moment, exited state quenching must also be taken into account,[59] as discussed in chapter 2.2.3.1. The emission enhancement in the case of fluorescence is interpreted as an environmental induced modification of the ability of the dipole to radiate energy, i.e. additional radiative decay channels. In the classical description (scattering) the ability of the dipole to interact with the incident field is modified, i.e. increase of the dipole amplitude.[52]

Combined excitation and emission enhancement

As described above the enhancement of the excitation rate (energy) scales with the square of the field enhancement factor f^2. Provided that the spectral response of the emitter's environment is broad compared to the Stokes shift of the emitter $\omega - \omega_0$ (approximation for negligible Stokes shift), the enhancement of the decay rate is as well given by the square of the same field enhancement factor f^2. Thus, assuming that the decay channels offered by the environment are only of radiative nature, the radiative emission enhancement scales with the fourth power of the field enhancement. For $f >> 1$ one can thus write [59]:

$$E_R^2 = f^4 E_R'^2, \qquad \text{Eq. 2.51}$$

with E'_R being the emitted field in absence of the field enhancing environment. This corresponds to the commonly assumed Raman enhancement by rough metal surfaces, scaling with the fourth power of the local field enhancement f. The source of the local field enhancement by rough metal surfaces is the excitation of surface plasmon modes.

Beyond unidirectional energy transfer

Another phenomenon regarding the interaction of an emitter and its environment is strong coupling. In the theory of energy transfer from donor to acceptor it is usually assumed that the field scattered by the environment can not re-excite the emitter since it is Stokes shifted to the emitter's absorption. Nevertheless, if the decay rate induced by the environment exceeds the vibration relaxation rate of the emitter this assumption is no longer given, since the Stokes shift is strongly reduced. Considering

an energy transfer from donor to acceptor, with donor and acceptor being identical molecules this may yield to coherent re-excitation of the donor by the acceptor which results into characteristic exciton bands shifted with respect to the emission of the non-interacting emitters.[59] The effect is called strong coupling, a prominent example is molecular J-aggregates [77-79].

Following this logic re-excitation by local fields should also apply to accessible (not instantaneous dissipated) evanescent fields excited in the environment by the emitter itself, e.g. surface plasmon modes (see chapter 2.2.3). This means that the emitter is driven (not necessarily coherently) by both the incident and its own field scattered by the environment (see also discussion part of this thesis). If the interaction between emitters and plasmons is coherent strong coupling is expected also in this case [80].

3 Experimental part

3.1 Absorption spectroscopy

Absorption spectroscopy measurements of thin dye films on mica substrates were performed in a double beam absorption spectrometer (UV-2101PC, Shimadzu) with blank reference. Prior to the absorption measurement and after deposition of the dye onto the surface (front side) of the mica substrate, the rear side was cleaved off in order to remove possible contamination. Then the absorption of the dye covered substrate was recorded. In order to obtain the absorption of the uncovered mica substrate, the dye covered surface (front side) was also cleaved off followed by recording the absorption of the bare substrate. The recorded pair of curves was aligned in the blue/violet spectral wavelength range, in which no dye absorption is expected.

3.2 Contrast spectroscopy

The following method was used for absorption measurements of layers with subnanometer thickness and lateral extension below 100 μm.

Contrast spectroscopy measurements were performed with a reflection microscope: Zeiss Axioskop equipped with a HBO 50 microscope lamp and narrow bandpass filters (center and half width according to the error bars in direction of the wavelength axis in Figure 4.22), crossed polarizers (see also Figure 3.2a) and a Nikon 40x/0.55 object lens. The illumination aperture was chosen to be slightly smaller than the aperture of the object lens in order to avoid possible contrast reduction. The contrast was measured with a CCD camera (kamPro 02IR, EHD) by separately averaging over the intensity of the graphene covered and uncovered regions.

Interpretation of the measured contrast with a Fresnel law based model allows to convert contrast into absorption, since reflection from thin films is mostly sensitive to its absorption (see results and discussion).

3.3 Fluorescence spectroscopy

Fluorescence spectra were obtained with an inverted fluorescence microscope (Axiovert 100 TV, Zeiss). The fluorescence of thin polymer and dye films on mica substrate was excited at 532 nm (Verdi-V5 laser, Coherent) and detected through a 570 nm longpass filter or, respectively, excited with a microscope lamp (HBO 50, Zeiss) equipped with a 450 nm – 490 nm bandpass filter and detected through a 515 nm long pass filter. The fluorescence was spectrally resolved with a CCD spectrometer (SP-150 spectrograph, Acton Research Corporation, equipped with a 300 grooves/mm grating and a LN/CCD-1340/100-EB/1 detector, Roper Scientific, see also Figure 3.1).

3.4 Fluorescence microscopy

Fluorescence images were acquired with an inverted fluorescence microscope (Axiovert 100 TV, Zeiss). The polymer films were excited at 532 nm (Verdi-V5 laser, Coherent) by transmitted light illumination (~ 100 W/cm^2) or, respectively, by impinging light illumination with a microscope lamp (HBO 50 equipped with UV/infrared blocking filters (Zeiss), ~ 0.5 - 1 W/cm^2) using a 515 nm - 560 nm band pass filter and a LD achroplan 20x/0.4 object lens (Zeiss); the dye films were accordingly excited using a 445 nm - 565 nm band pass filter (Laser Components) and a Plan 40x/0.55 object lens (Nikon). The fluorescence of polymer films was collected with a LD achroplan 20x/0.4 object lens (Zeiss) through a 590 nm long pass filter (Zeiss) and detected with CCD camera (kamPro 02IR, EHD). The fluorescence of dye films was collected with a Plan 40x/0.55 object lens (Nikon) through a 585 nm long pass filter (Laser Components) and detected with a cooled CCD camera (SC4022, EHD). The intensity of images recorded from mica substrates, not covered with dye and freshly cleaved from both sides, in the same setup used to record fluorescence images was regarded as background and subtracted from the fluorescence intensity of the dye covered mica substrates.

3.5 Confocal microscopy

Confocal microscopy measurements were performed with home-made setups based on Zeiss microscopes.

The setup used for confocal optical spectroscopy (fluorescence and Raman) is described in Figure 3.1 and chapter 3.5.1 (see below). The low thickness of the samples (subnanometer - nanometer) does not generally require the use of an aperture (decrease of depth of field), high resolution can already be achieved with a diffraction limited laser spot.

Details of the setup used for fluorescence decay measurements can be found in chapter 3.5.2.2 (see below) and in reference [81].

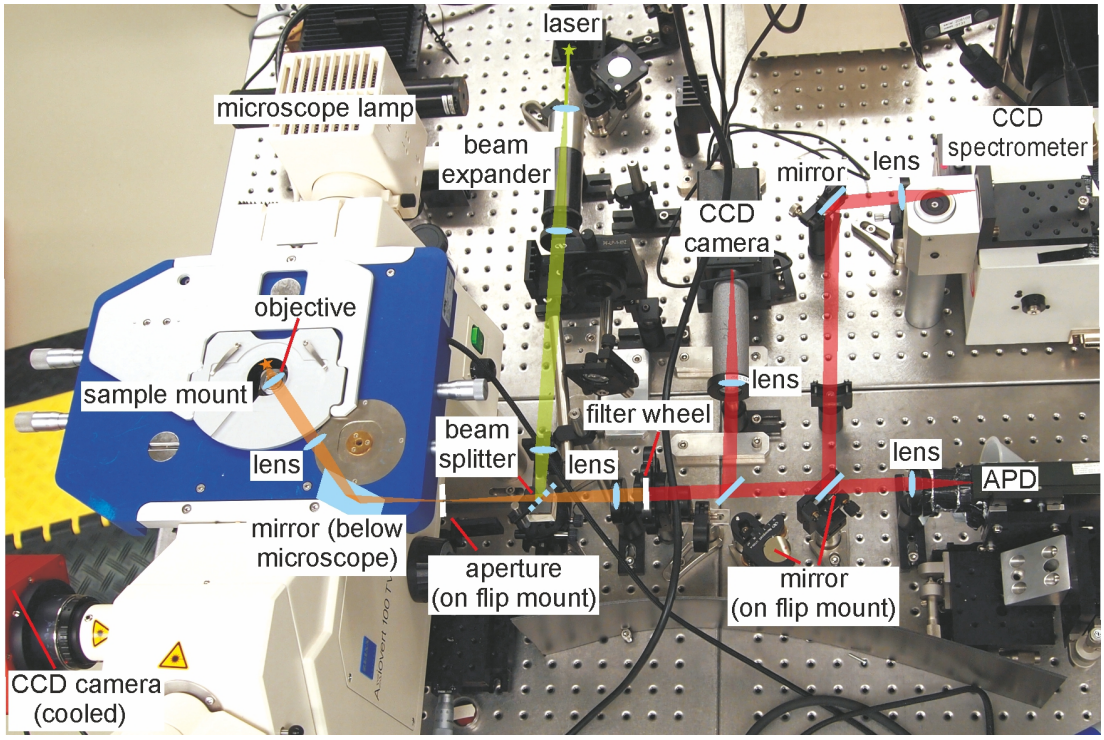

Figure 3.1. Photography and sketch of the confocal microscope used for spectroscopy. The optical path is visualized with the green (laser), orange (laser and emission of the sample) and red (emission of the sample) shaded areas. The setup is based on a Zeiss Axiovert 100 TV equipped with 532 nm laser (4611-050-1000 µGREEN-SLM Nd:YVO4 Laser, JDS Uniphase) and a CCD spectrometer (SP-150 spectrograph, Acton Research Corporation, equipped with a 1200 grooves/mm or, respectively, 300 grooves/mm grating and a LN/CCD-1340/100-EB/1 detector, Roper Scientific). The switchable apertur allows also to record spectra non confocally excited using the microscope lamp. Confocal images (scanning of sample mount, JPK TAO module) and time evolution of the fluorescence can be recorded with an avalanche photodiode (APD, SPCM-AQ-14Y, EG&G). The black CCD camera on the table can be used for adjustment of the positions of the laser spot and a regions of interest, e.g. graphenes. The cooled CCD camera allows to record low noise fluorescence images.

3.5.1 Optical spectroscopy

Raman measurements were performed with a confocal microscope based on an inverted fluorescence microscope (Zeiss Axiovert 100 TV equipped with a Nikon Plan 40x/0.55 object lens, see Figure 3.1). The spectra (Raman and background fluorescence) were excited at 532 nm (4611-050-1000 μGREEN-SLM Nd:YVO4 Laser, JDS Uniphase) and recorded with a CCD spectrometer (SP-150 spectrograph, Acton Research Corporation, equipped with a 1200 grooves/mm grating and a LN/CCD-1340/100-EB/1 detector, Roper Scientific); excitation light was additionally blocked with 550 nm long pass filter (Thorlabs, reaching nearly its full transmittance at 564 nm, equals ~1067 cm^{-1}), background was recorded on bare mica substrate and subtracted from the spectra recorded on dye and graphene covered mica substrates.

Optical identification of the graphenes before the Raman measurement in the same setup (see chapter 3.8) allowed to record spectra separately on uncovered regions and regions covered by different numbers of graphene layers.

3.5.2 Time resolved fluorescence

3.5.2.1 Fluorescence evolution

The evolution of continuously excited polymer fluorescence on a time scale between millisecond and days was confocally detected with an avalanche photodiode (SPCM-AQ-14Y, EG&G).

3.5.2.2 Fluorescence decay

Time resolved fluorescence decay measurements of thin dye films on mica substrate were performed with a confocal microscope based on an inverted fluorescence microscope (Axiovert 200, Zeiss). The dyes were excited at 532 nm (LDH-P-FA-530, PicoQuant), and the fluorescence was detected through a longpass filter with an avalanche photodiode (SPCM-AQR-14, Perkin Elmer); the time intervals between excitation and detection of the fluorescence were measured by time-correlated single photon counting (Picoharp 300, PicoQuant). Further details of the setup can be found in reference [81].

3.6 Scanning force microscopy

Scanning force microscopy (SFM) images of polymer films partially covered by graphenes were recorded in tapping mode under ambient condition (JPK NanoWizard).

SFM images of graphenes and dyes confined by graphenes were recorded by operating in tapping mode under controlled humidity (MultiMode SFM, Veeco Metrology; Nanoscope IIIa and IV SFM controller, Digital Instruments; AC160TS SFM cantilever, Olympus). The SFM head was placed in a bell jar chamber; the humidity inside the chamber was measured with a humidity sensor (testo 635 and testo 625, Testo AG) and controlled by purging with dry nitrogen or dry nitrogen bubbled through purified water.

3.7 Deposition of P3HT and R6G on muscovite mica

Thin polymer films were produced by spincoating (SCI 20, Novocontrol) from chloroform solution onto freshly cleaved muscovite mica (Ratan mica exports, V1 (optical quality)). Regioregular poly(3-hexylthiophene) (P3HT) and chloroform (Sigma Aldrich) were used as received. The film thickness of undegraded freshly prepared P3HT films was determined with SFM (see above) by measurement of the depth of trenches generated in the soft P3HT film using a flexible tapered fiber. The quoted error is the standard deviation of the film thickness of films prepared under the same conditions.

Submonolayers of rhodamine 6G (R6G) were prepared by spincoating from aqueous solutions (purified, 0.1 μm filtered water (Sigma-Aldrich), concentrations 0.03 – 0.1 mM) onto freshly cleaved muscovite mica (Ratan mica exports, V1 (optical quality)) under ambient conditions (22-23°C, 40 - 48% relative humidity (RH)). The rear side of the substrate was cleaved off after spincoating to remove its possible contaminations. Submonolayer thickness of R6G was confirmed by absorption spectroscopy and scanning force microscopy (see results and discussion).

3.8 Deposition and identification of graphenes

3.8.1 Graphenes on mica

This chapter introduces identification of graphenes on mica substrate by reflection microscopy, used as a basis for identification of graphenes on top of polymer and dye layers on mica substrate (see chapter 3.8.2, 3.8.3 and the results and discussion part of this thesis).

The following is in part reprinted with permission from High contrast optical detection of single graphenes on optically transparent substrates, M. Dorn, P. Lange, A. Chekushin, N. Severin and J.P. Rabe, Journal of Applied Physics, 108 (2010). Copyright 2013 American Institute of Physics.

In this thesis graphenes were fabricated by mechanical exfoliation from graphite, since this is a source for graphenes of high quality. A drawback of the mechanical exfoliation is the low surface density of single graphene deposits and the difficulty to detect them resulting from their high optical transparency [2].

Raman microscopy has been demonstrated to be a powerful tool for identification of single and double layer graphenes [82], however, a careful examination of the recorded spectra is necessary.

Scanning force microscopy (SFM) has been used to identify and image graphenes, however, search for single graphenes with SFM can be very time consuming, and moreover, the apparent height of graphenes in SFM images is sensitive to scan parameters [83]. This makes unambiguous and efficient identification of graphenes with SFM rather difficult.

Thus ordinary optical microscopy remains still one of the most important and efficient methods of graphene detection. Sufficient high contrast of graphene for its detection with a naked eye can be achieved on Fabry–Pérot structures composed of an opaque silicon substrate covered with a transparent oxide layer.[84-87]

However, it would be advantageous to perform experiments with graphenes on transparent and atomically flat substrates (e.g. for combined optical spectroscopy and

SFM). Mica is a commonly used transparent and atomically flat substrate. Furthermore, the birefringence of mica can be used to achieve contrasts comparable to that on Fabry–Pérot structures [84-87] by using reflection microscopy to observe the graphenes through the substrate and employ crossed polarizers to block light reflected from the upper air-mica interface (see Figure 3.2a and below). This method allows reliable and efficient detection of graphenes on mica substrate and will be described in the following including a theoretical interpretation of the measured contrasts.

Figure 3.2b shows a reflection microscopy image of graphenes exfoliated from graphite (Madagascar, NGS Naturgraphit GmbH) on muscovite mica (Ratan mica exports, V1 (optical quality)) using the standard method of mechanical exfoliation of graphite [1,24] - repeated peeling of natural graphite flakes with scotch tape.

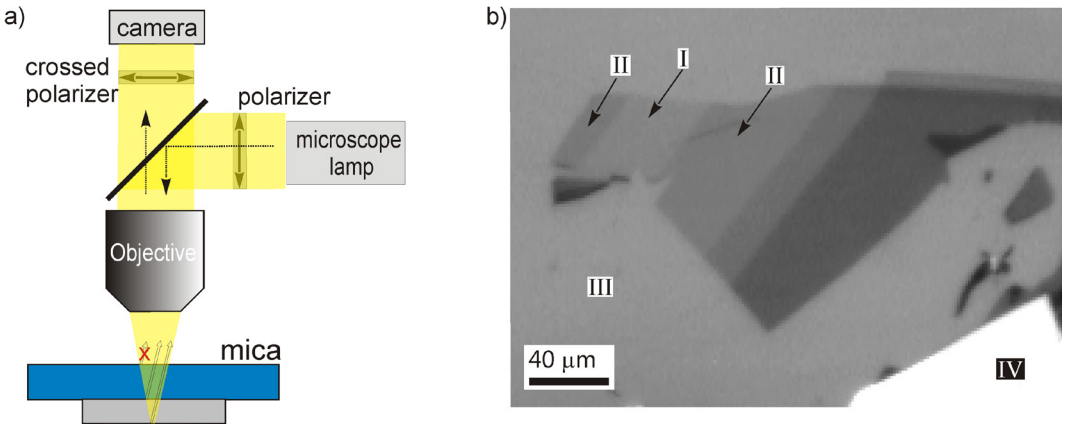

Figure 3.2. a) Scetch of the setup used for identification of graphenes. Reflection images were recorded by illuminating the samples through the mica substrates. The use of crossed polarizers prevents the light reflected from the upper mica interface taking part in contrast formation on the images. b) Reflection image of graphenes were recorded with a Zeiss Axioskop equipped with crossed polarizers, a Halogen lamp and a CMOS camera (SMX-155M, EHD). Single, double and multilayer layer graphenes are marked as (I), (II) and (IV), respectively; the uncovered mica region as (III).

The samples were suspended over a black background with low reflectivity and imaged in reflection using a Zeiss Axioskop with a 20x/0.4 object lens. Illumination was carried out with light from a 50 W halogen lamp passed through a linear polarizer. Light reflected from the sample was passed through a crossed linear polarizer. Micrographs were taken with a CMOS camera (SMX-155M, EHD imaging GmbH). Background correction was performed prior to the measurements. The mica sample was rotated around the optical axis of the microscope until the

highest brightness was achieved. The crossed polarizers increase substantially the contrast of graphenes (explanation see below).

Thick graphene flakes appear brighter than the background (Figure 3.2b, regions marked with IV and, respectively, III), but also flakes darker than the mica background were detected (I, II). The dark flakes exhibit clear contrast quantization and terracing. Tapping-mode scanning force microscopy (SFM) measurements revealed the height of the darkest terraces to be about six nanometers (not shown).

Raman spectra of the objects with apparently lowest contrast were recorded and could thereby be identified as single layer graphenes (see reference [88]).

The contrasts C of the graphene flakes can be quantified by comparing the mean intensity of graphenes covered ($I_{graphene}$,) and uncovered (I_{mica}) regions with the contrast C being defined as $(I_{mica} - I_{graphene},)/(I_{mica})$.

The contrast of graphenes varied from sample to sample with contrasts between 7% and 10% for monolayers and contrasts between 14% and 20% for bilayers. The large error can be attributed to camera non linearity and inhomogeneous illumination.[89] In order to minimize the experimental error a violet laser was used as light source combined with a calibrated photo detector for contrast detection. This resulted in measured contrasts of 12.8% ± 1.2% and 22.7% ± 1.6% for the single and double graphenes, respectively (see also reference [88]), the increased contrast very likely results from increase of the graphene absorption beyond the green wavelength range [2].

The measured contrasts of the graphenes can be calculated with a Fresnel law based model taking into account in the graphene region the reflections at the mica-graphene and graphene-air interface and in the mica region the reflection at the mica-air interface. The reflection at the air-mica interface can be neglected through the use of crossed polarizers. Assuming normal light incidence only, for mica a homogeneous refractive index of 1.596 (ref. [90]) and for graphene the refractive index of graphite (2.675 - 1.35i) [91] and 0.34 nm as the thickness of a single graphene layer [84] this yields calculated contrast of 10% for single layer and 20% for double layer graphene

at 600 nm (roughly the wavelength of peak detection of the reflected intensities resulting from the emission spectrum of the halogen lamp and the spectral response of the used camera). The calculated contrasts are in good agreement with the measured contrasts. Furthermore the Fresnel model predicts a peak contrast for about 20 layers of graphene (roughly corresponding to the number of layers in the darkest regions in Figure 3.2b) and a negative contrast for more than about 50 layers of graphene. It should be noted that multilayer graphenes containing about 45 layer have at 600 nm almost the same calculated contrast as single layer graphenes. However these layers appear slightly blue coloured and can thus be distinguished from single layer graphene.[88]

Taking additionally into account the reflection from the upper air-mica interface results in a strong decrease of the calculated and measured (without crossed polarizers) graphene contrast by a factor of about 2, which already makes a fast preselection by the naked eye difficult. Furthermore the reflection from the upper mica air interface can be expected to be substrate thickness and object lens aperture dependent (depth of sharpness) which makes a reliable detection without crossed polarizers difficult.

In summary the suggested method allows reliable, simple and fast detection of graphenes on mica substrate with a contrast sufficiently high to be observable by the human eye. The method can also be applied for identification of graphenes confining thin organic layers (see next chapters).

3.8.2 Graphenes on P3HT films

The standard method of mechanical exfoliation of graphite [1,24] - repeated peeling of natural graphite flakes (Madagascar, NGS Naturgraphit GmbH) with scotch tape - was used for deposition of the graphenes onto the P3HT films. The peeled flakes were gently pressed against the P3HT films under nitrogen flow and graphenes attach to the film surface presumably due to van der Waals forces. The samples were never exposed to ambient atmosphere for more than a few seconds during spincoating and transport and thereby only exposed to indirect lightning of less than 10 $\mu W/cm^2$. Thus photo-induced degradation of the P3HT films prior to fluorescence

investigation can be neglected, since irreversible degradation needs time or intense illumination [18].

Graphenes on P3HT films were identified optically by reflection microscopy [88] (Axiovert 100 TV equipped with a LD achroplan 20x/0.4 object lens, Zeiss) under continuous nitrogen flow. The sample was illuminated through the mica substrate (HBO 50 micrsocope lamp, spectrally narrowed with a 585 nm long-pass and infrared blocking filter, Zeiss), the reflected light was detected through crossed polarizers. Images were acquired with a CCD camera (kamPro 02IR, EHD) operated with a manual exposure time and gain setting along with a minimum gamma to minimize non linear behaviour. The response of the camera was additionally verified with a calibrated photodetector (818-UV, Newport). The number of graphene layers was derived based on the optical contrast estimated with a Fresnel law based model including the ambient atmosphere, graphenes, the P3HT film and the mica substrate (see results and discussion). Supposed single graphenes were confirmed with Raman spectroscopy.

3.8.3 Graphenes on R6G submonolayers

Graphenes were deposited onto the R6G covered mica substrates by mechanical exfoliation of highly oriented pyrolytic graphite (Momentive, HOPG, grade ZYB). The HOPG bulk crystal was cleaved with scotch tape prior to the exfoliation process. Then, the freshly cleaved surface of the HOPG bulk crystal was brought gently into contact with the R6G covered mica substrates. This method allows to fabricate graphenes essentially free of contamination by scotch tape residuals, important for determination of the orientation of the confined R6G molecules (see results and discussion).

Graphenes were identified optically by reflection microscopy [88] using an Axiovert 100 TV equipped with a HBO 50 microscope lamp with UV and infrared blocking filters (Zeiss) and a Plan 40x/0.55 object lens (Nikon). The samples were illuminated through the mica substrate in a spectral region of small R6G absorption (lamp spectrally narrowed with a 565 nm – 595 nm band pass filter), necessary to minimize contribution of R6G absorption to the contrast of the graphenes (see results and

discussion); the reflected light was detected through crossed polarizers. Images were acquired with a cooled CCD camera (SC4022, EHD).

4 Results and discussion

4.1 Graphenes as water and oxygen permeation barriers

4.1.1 Introduction

Conjugated polymers are widely used as active layers in organic electronics [92,93]. While they have great potential for light weight and flexible optoelectronic devices, they suffer from rather fast degradation under ambient conditions due to reactions with oxygen and water [18-20]. In order to achieve reliable and long time operation, commercial organic devices are generally protected with composite barrier layers to meet the technologically required oxygen and water transmission rates [22,23]. However, these barrier layers suffer from limited transparency due to light scattering caused by domain boundaries and surface roughness [94].

Graphene with its remarkable properties, including high conductivity [4], transparency [2] and mechanical flexibility [5], is a highly appealing electrode material for flexible organic optoelectronic devices [12], especially as it is based on the abundantly available carbon, while the predominant current transparent electrodes from indium tin oxide (ITO) suffer from limited natural indium resources. Recent efforts to fabricate large area graphene electrodes have shown that high-throughput, low cost processing is possible, as demonstrated for organic solar cells [7], OLEDs [13] and displays [12]. Moreover, graphene offers the possibility that it could not only serve as a transparent electrode, but simultaneously act as a permeation barrier.

The following chapters cover investigations of the chemical and structural stability of graphene *in-situ* on a conjugated polymer film. Fluorescence and scanning force microscopies are used to probe the degradation kinetics of the fluorescent polymer protected from ambient by graphene. Changes of the continuously excited polymer fluorescence are monitored over time and compared for single, double, and triple

layer graphenes. Finally the Stern-Volmer equation will be used to convert the fluorescence degradation into an upper bound for the water vapour and oxygen transmission rates (WVTR and OTR, respectively) through graphenes.

The next chapter will describe how to identify graphenes on thin polymer films. This is more challenging than the identification of graphenes on bare mica substrate [88] as discussed in the following.

4.1.2 Identification of graphenes on P3HT films

Graphenes were identified by reflection microscopy with the setup described in the methods section (see also ref. [88]). The microscope lamp was spectrally narrowed with a 585 nm long-pass and infrared blocking filter (Zeiss), a wavelength range at which P3HT exhibits low light absorption [95], and imaged under continuous nitrogen flow in order to minimize degradation of P3HT prior to fluorescence investigation. Illumination in a wavelength range with low P3HT light absorption is also advantageous for identification of graphenes (see below).

Since a polymer layer confined between mica and graphene has very like impact on the measured contrast of graphene, it will be estimated in the folllowing how to detect graphenes on thin polymer films. The contrast behaviour of graphenes deposited on P3HT covered mica was calculated by a Fresnel law based model with three interfaces. The reflection at the interface between mica and nitrogen gas can be neglected due to the use of crossed polarizers [88]. The reflection coefficients at all interfaces are given by [96]:

$$r = \frac{n_1 - n_2}{n_1 + n_2}, \qquad \text{Eq. 4.1}$$

where n_1 and n_2 are the refractive indices of the media forming the interface. The total intensity reflected by the graphene covered regions can be written as

$$R_{graphene} = \left| \frac{r_{mp} + r_{pg} e^{-i\left[\frac{4\pi}{\lambda} n_p d_p\right]} + r_{gn} e^{-i\left[\frac{4\pi}{\lambda}\left(n_p d_p + n_g d_g\right)\right]} + r_{mp} r_{pg} r_{gn} e^{-i\left[\frac{4\pi}{\lambda} n_g d_g\right]}}{1 + r_{mp} r_{pg} e^{-i\left[\frac{4\pi}{\lambda} n_p d_p\right]} + r_{mp} r_{gn} e^{-i\left[\frac{4\pi}{\lambda}\left(n_p d_p + n_g d_g\right)\right]} + r_{pg} r_{gn} e^{-i\left[\frac{4\pi}{\lambda} n_g d_g\right]}} \right|^2 , \quad \text{Eq. 4.2}$$

with r_{mp}, r_{pg} and r_{gn} the reflection coefficients at the mica-P3HT, P3HT-graphene and graphene-nitrogen interface. λ is the wavelength of the illumination light, d_g the thickness of the graphene layer and d_p the thickness of the P3HT film. Mica is simplified to be isotropic with a refraction index of n_m = 1.596 [90]. Graphene is assumed to have the refractive index of bulk graphite n_g = 2.675 – 1.35i for an electric field parallel to the orientation of the graphene sheet [91], and the monolayer thickness is assumed to be 0.34 nm [84]. The strongly wavelength dependent refraction index of solid P3HT was assumed to be n_p = 2.4 – 0.45i at 600 nm [95].

Graphenes deposited on e.g. 4 nm thick P3HT yield calculated contrasts of 9.4% for single layer, 18% for double layer, and 25.7% for triple layer graphene. The calculated contrasts of graphenes decrease dramatically for thicker P3HT films, eg. 0.8% for single layer, 1.4% for double layer and 1.9% for triple layer graphene on 20 nm P3HT. This behaviour was confirmed experimentally, inasmuch as it was quite difficult to image and distinguish few layer graphenes on P3HT films with thickness in the range of tens of nanometers, due to strongly reduced contrast resulting from light absorption by the P3HT film. Therefore P3HT film thicknesses on the order of a few nanometers were chosen to perform the fluorescence experiments. The low P3HT film thickness is also preferable for a sensitive estimation of the water vapour and oxygen transmission rates through graphene (see chapter 4.1.6).

Figure 4.1a shows a reflection microscopy image of a 4 nm ± 0.4 nm thick P3HT film partly covered by graphene recorded under nitrogen flow prior to investigation with fluorescence microscopy. Graphenes appear as regions of dark contrast relative to the uncovered film (X) with the contrast depending on the number of graphene layers. Double layer graphene (II) appears to be darker than single layer graphene (I), triple layer graphene (III) appears even darker. The measured contrast of 10.2% ±

2.4% for single layer, 17.7% ± 2.3% for double layer, and 23.8% ± 2.2% for triple layer graphene on the P3HT covered mica substrate are consistent with the calculated contrasts (see above) within the errors and allowed reliable identification of the number of graphene layers (the quoted error results from camera noise, camera nonlinearity and inhomogeneous illumination). The monolayer assignment was additionally verified with Raman spectroscopy [82] (Figure 4.1b, Renishaw, excitation at 488 nm).

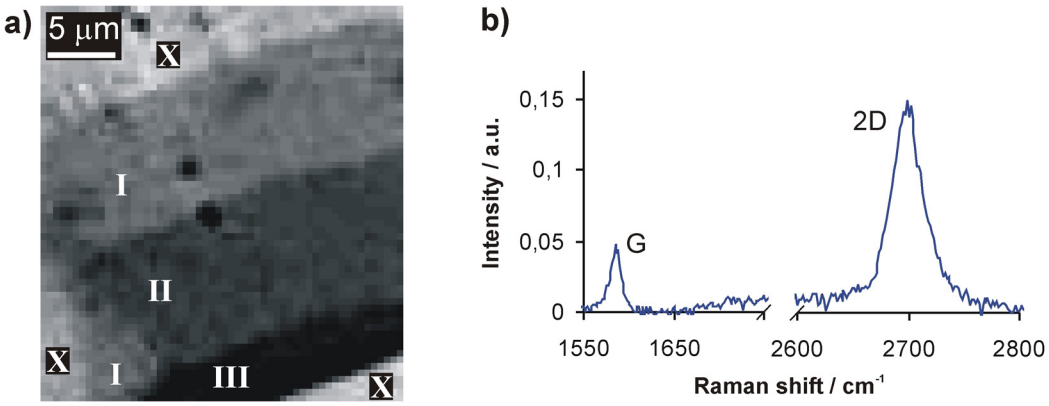

Figure 4.1. a) Contrast enhanced reflection microscopy image of graphene covered P3HT film on mica substrate, (I) single layer graphene, (II), double layer graphene, (III) triple graphene, (X) uncovered P3HT film. b) Raman spectrum of single layer graphene obtained after fluorescence investigation (see below). Signal to noise ratio suffers from a strong P3HT fluorescence background, subtracted from the spectrum. Profile and FWHM of the 2D peak confirms monolayer thickness [82].

4.1.3 Fluorescence of unconfined and confined P3HT

The next chapters cover fluorescence investigation of unconfined P3HT and P3HT confined by single and multilayer graphene. Additionally thin mica films were used as reference for an impermeable barrier.

4.1.3.1 Fluorescence of P3HT under nitrogen flow and in ambient athmosphere

Figure 4.2a shows a fluorescence spectrum of a 4 nm ± 0.4 nm thick P3HT film on mica substrate under nitrogen flow. The two typical peaks around 637 nm and 738 nm are observed, arising from intra – and intermolecular excitations [97,98]. Exposing the P3HT films to the ambient results into a fast decay of the fluorescence within tens of miliseconds (Figure 4.2b). The strong and fast fluorescence decay of

uncovered P3HT is attributed to photo-induced P3HT degradation through interaction with water and oxygen [18-20].

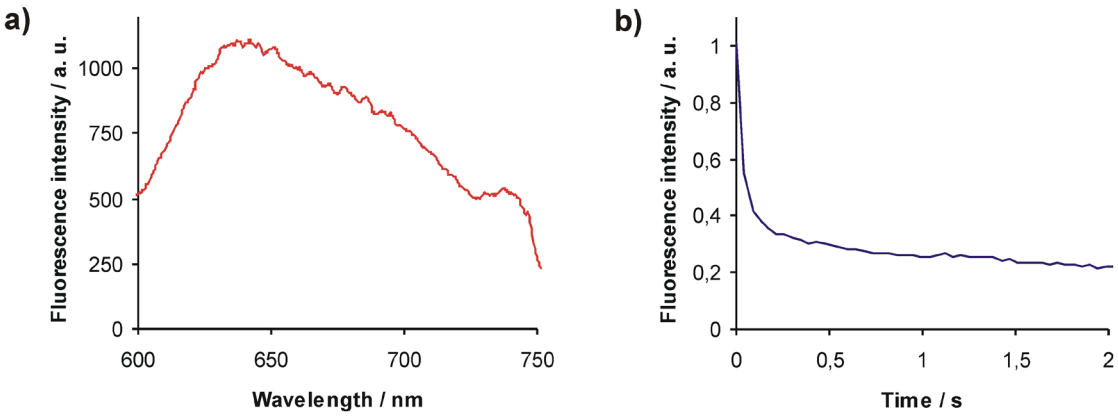

Figure 4.2. a) Fluorescence spectrum of 4 nm thick P3HT film under nitrogen flow b) Fluorescence decay of a 4 nm thick P3HT film in ambient athmosphere.

4.1.3.2 Fluorescence of P3HT confined by graphenes

In order to investigate the barrier properties of graphenes, freshly prepared P3HT films were covered by graphene. The degradation of graphene covered polymer films was investigated during continuous illumination (~ 100 W/cm^2) for 44 h. The total intensity incident on the sample during the investigation for nearly two days was chosen to be comparable to the intensity incident on a solar cell during 10.000 h of operation. First fluorescence images of the as-prepared P3HT film were recorded under nitrogen flow to determine the fluorescence intensity of the undegraded P3HT. Figure 4.3a displays a fluorescence image of the micrograph depicted in the Figure 4.1a. The graphene covered P3HT film regions (I, II, III) appear darker than the uncovered regions (X). The fluorescence of the film regions covered with one, two, or three layers of graphene (I, II, III) is equally lowered by 42% ± 6% compared to the uncovered regions. It is attributed to quenching of the P3HT fluorescence by graphene [99].

Figure 4.3b shows a fluorescence image of the same sample acquired after 6 minutes of continuous illumination under ambient conditions. The fluorescence of the uncovered P3HT film regions (X) has dropped below the detection limit of the camera (on a time scale of tens of milliseconds; see Figure 4.2b). In addition, the fluorescence is degraded near the edges of the graphene layer and in some regions of the film covered with single layer graphene. Interestingly the dark areas do not grow

significantly even after continuous illumination under ambient conditions for nearly two days (Figure 4.3b - d). The bright areas exhibit even a weak fluorescence increase during the first hours of illumination (Figure 4.3b and c), which is attributed to improved π-stacking (see discussion below).

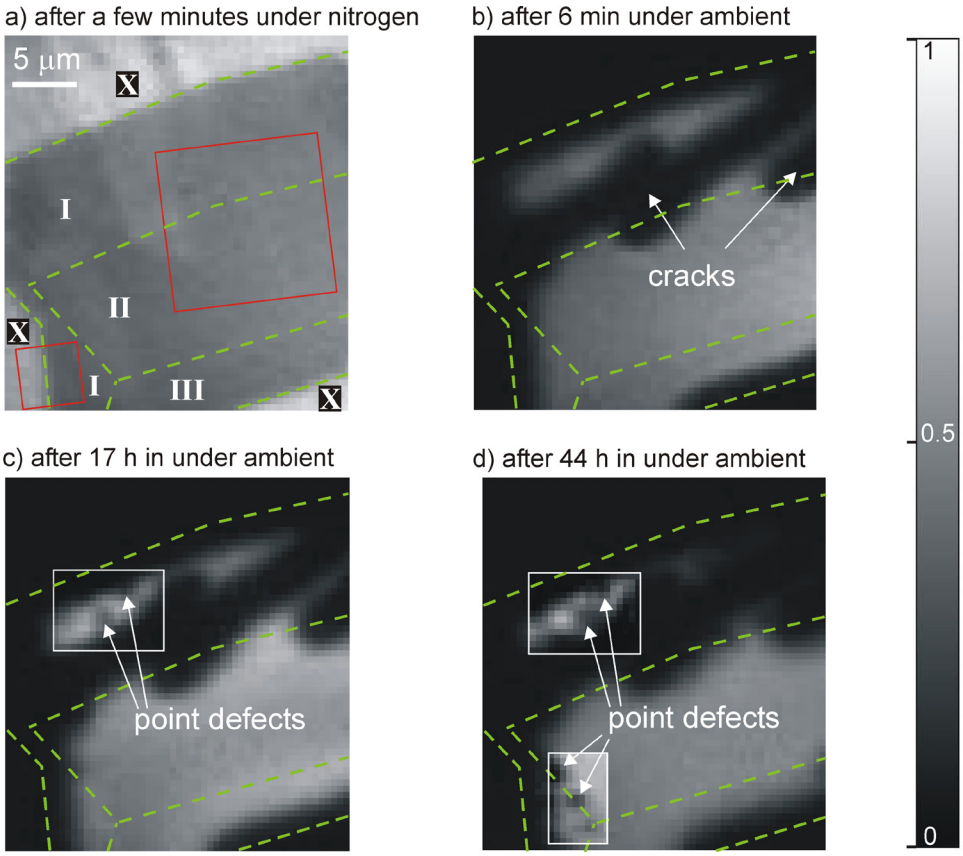

Figure 4.3. Fluorescence images of a P3HT film partially covered by graphenes excited with ~ 100 W/cm^2 at 532 nm a) Under nitrogen flow. b) – d) After 6 min, 17 h and 44 h of illumination, respectively, under ambient. Green dashed lines indicate regions with single (I), double (II) and triple layer (III) graphene, and uncovered (X) P3HT film. Red squares in a) indicate location of SFM images in Figure 4.6 a) and b). White rectangles in c) and d) indicate contrast enhanced regions of the image.

The fluorescence of film regions covered with double and triple layer graphene exhibit only a slight attenuation after nearly two days of continuous illumination (Figure 4.3d). This small decrease is approximately linear with time (see Figure 4.8). In contrast, there are signs of stronger degradation in regions covered with single layer graphene and at the edges between single and double layer graphene. Dark spots appear after several hours of illumination (Figure 4.3c and d) in regions that exhibit no significant degradation for the first minutes of illumination (Figure 4.3b). The total number of these dark spots increases over time. After nearly two days of

continuous illumination, the fluorescence from film regions covered with single layer graphene is significantly degraded in comparison to the fluorescence from regions covered with double layer graphene (Figure 4.3d).

The strong and fast fluorescence decay of uncovered P3HT film regions under ambient conditions (Figure 4.2b and Figure 4.3b) is attributed to photo-induced P3HT degradation through interaction with water and oxygen [18-20]. The degradation of graphene covered P3HT film regions near the edges and cracks (see SFM image in Figure 4.6) of the graphene layer (Figure 4.3c-d) results from water and oxygen diffusing through the P3HT film under the graphene layer. The width of the dark region reflects the maximum diffusion length of water and oxygen prior to their photo-induced reaction with P3HT. One might suspect that the regions near the edges, exhibiting strong fluorescence degradation, cannot provide reaction sites for water and oxygen anymore. However regions of strong P3HT fluorescence degradation can still exhibit strong light absorption [18] which is sufficient for photo-induced reaction of water and oxygen with P3HT.

The centers of the graphene covered P3HT film regions exhibit only small changes in the fluorescence over time (Figure 4.3a-d), since the graphene layer acts as an efficient barrier and thus protects the P3HT from contact with water and oxygen. A small fluorescence increase of graphene covered P3HT (Figure 4.3a-c), which is also observed for P3HT under inert conditions without graphene (see Figure 4.8), can be attributed to improved π-stacking of the P3HT chains [100]. Any significant fluorescence increase is apparently saturated after a few hours (Figure 4.3c-d and Figure 4.8). The moderate fluorescence decrease of P3HT covered with double layer graphene (Figure 4.3c-d) is attributed to possible water and oxygen diffusion under the graphene layer from the edge of the graphene layer and intrinsic P3HT fluorescence degradation.

The permeable point defects (dark spots in Figure 4.3c and d) result from a slow disassembly of the graphene layer upon illumination or from intrinsic defects in pristine graphene. Since the observed defect density is at least one order of magnitude lower than the average density of intrinsic lattice vacancies in the first monolayer of natural [101] and highly oriented pyrolytic graphite (HOPG) [102,103],

the visible defects are attributed to light induced bond breaking [104] and chemical degradation of graphene by radicals [105] and catalytically active impurities [106]. Here radicals generated by photo-induced P3HT degradation [19] and catalysts from P3HT synthesis [16] are likely involved in the formation of defects in graphene. However the driving force for formation of visible defects is apparently not strong enough to break the lattice of two layers of graphene at one site, not even at folds or at the edge between double and triple layer graphene (Figure 4.3 and Figure 4.6b).

Despite the dark spots growing in, some small regions of the film covered with single layer graphene exhibit visually no strong degradation even after 44 h of continuous illumination under ambient (Figure 4.4). In the following the fluorescence image in Figure 4.4 will be used to check whether P3HT protected by visually defect free single layer graphene exhibits equal fluorescence as P3HT protected by double layer graphene. Differences could e.g. result from weak diffusion through defect free single layer graphene and should manifest itself in the mean value and distribution (e.g. in the case of inhomogeneous diffusion) of the intensity. The red and blue rectangles in Figure 4.4 indicate regions that will be used in the following to compare the fluorescence of single and double layer graphene regions, respectively.

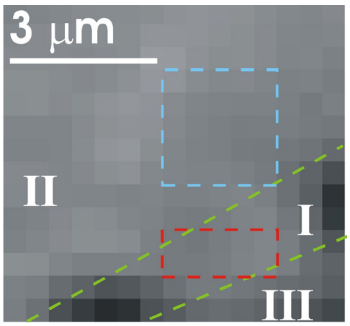

Figure 4.4. Fluorescence image of P3HT film regions covered by single (I), double (II) and triple layer graphene (III) after 44h of continuous illumination. The fluorescence image is averaged from four images of the same sample, which were all acquired under the same conditions within a few seconds. The pixel-size is in the range of the optical resolution of the setup. Red and blue rectangles indicate regions used for investigation of the fluorescence intensity distribution of film regions covered with single and double layer graphene, respectively.

For this it will be tested, if the fluorescence in the blue and red rectangle comes from populations with the same fluorescence intensity distribution. The empirical cumulative distribution function of the red and blue rectangle is denoted with $R_n(t)$,

$B_m(t)$ (number of data values that do not exceed t / total number of data values $n = 10$ and accordingly $m = 25$ of the samples), respectively, and the null hypothesis $H_0 : R = B.$ against $H : R \neq B$ will be tested (Two-Sample Kolmogorov-Smirnov Test).

If H_0 is true, then the statistic

$$\sqrt{\frac{m \cdot n}{m+n}} \cdot D_{n,m}, with\ D_{n,m} = \sup_t \left| R_n(t) - B_m(t) \right| \qquad \text{Eq. 4.3}$$

has a limiting distribution function given by the cumulative distribution functions of the Kolmogorov distribution [107].

t	$R_n(t)$	$B_m(t)$	$D_{n,m}$
83	0,10	0,00	0,10
84	0,10	0,04	0,06
85	0,40	0,12	0,28
86	0,50	0,16	0,34
87	0,60	0,20	0,40
88	0,60	0,32	0,28
90	0,70	0,44	0,26
91	0,80	0,60	0,20
92	0,80	0,72	0,08
93	1,00	0,76	0,24
94	1,00	0,80	0,20
95	1,00	0,88	0,12
96	1,00	0,92	0,08
97	1,00	0,96	0,04
103	1,00	1,00	0,00

Table 1. Empirical cumulative distribution functions $R_n(t)$, $B_m(t)$ dependent on the fluorescence intensity t of the red and blue rectangle, respectively, and their difference $D_{n,m}$.

Table 1 lists $R_n(t)$, $B_m(t)$ and their difference $D_{n,m}$, dependent on the jointly ordered fluorescence intensities t observed on the two samples. The supremum of $D_{n,m}$ is 0.4 and the statistic in Eq. 4.3 corresponds to a p-value of about 0.202 [107]. Thus there is no reason to reject H_0. From this one can conclude that single and double layer graphene regions exhibit the same fluorescence intensity after 44 h of continuous illumination under ambient. Therefore there is no evidence for permeation of water and oxygen through defect free graphene (e.g. by tunnelling [108]) and the upper limits of the water and oxygen transmission rates through double layer graphene should also apply to single layer graphene (see discussion below).

Despite graphene acting as a permeation barrier and therefore protecting P3HT from degradation under ambient there must be a small probability for water and oxygen reaching the center under the double layer graphene within hours through lateral water and oxygen diffusion from the edges of the graphene. Indeed at much lower illumination intensities (~ 1 W/cm^2) significant lateral water and oxygen diffusion through graphene covered P3HT films prior to reaction occurs over more than ten microns. The diffusion, visible from P3HT fluorescence degradation, starts from the edge of the graphene layer and moves to its center within a few minutes (Figure 4.5).

In contrast at intense illumination (~ 100 W/cm^2) even exposure of the sample to ambient for nearly two days showed no significant increase of the diffusion path sufficient for reaction of water and oxygen with P3HT (dark region near the edge of the graphene layer in Figure 4.3b-d).

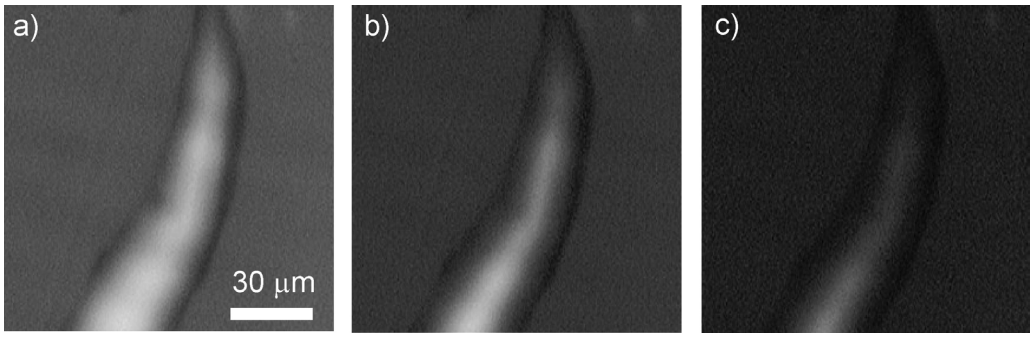

Figure 4.5. Fluorescence image of a ~ 30 nm thick P3HT film covered with thin graphite (< 100 nm) at moderate illumination intensities (~ 1 W/cm^2, 515 nm – 560 nm bandpass filter) under ambient condition acquired after a few seconds a), 80 s b) and 280 s c) exposure to ambient.

The larger diffusion path of water and oxygen prior to reaction at moderate illumination intensities (Figure 4.5) is attributed to a lower reaction probability of water and oxygen with P3HT. As the reaction is photo induced, the diffusion path prior to reaction can be controlled by the illumination intensity.

It should be noted, that thicker films (~ 30 nm) were used for fluorescence imaging at moderate excitation intensities since the fluorescence intensity of nanometer thin films was below the detection threshold of the camera. The lateral water and oxygen flux through covered P3HT films and thus the number of reaction sites per diffusant molecule should be independent on P3HT film thickness. Thus also the diffusion path of water and oxygen prior to reaction is assumed to be independent on the P3HT film thickness.

4.1.4 Structure of graphene on photo-degraded P3HT

In order to investigate possible correlations of regions of strong P3HT fluorescence degradation with possible structural degradation of the sample, SFM images were acquired after 44 h of illumination. Figure 4.6 displays SFM images of regions of interest marked in Figure 4.3a with red squares.

The height of the uncovered P3HT (X) in Figure 4.6a is significantly lower than the P3HT regions covered with graphene (I), and increases continuously by $1.9\ \text{nm} \pm 0.2\ \text{nm}$ over $\sim 1\ \mu\text{m}$ from the edge of the graphene layer to its center (Figure 4.6c). This height difference indicates a volume loss of $48\% \pm 15\%$, estimated from the film thickness of a freshly prepared film. In Figure 4.6b, the dark areas (see Figure 4.3) under the single layer graphene (I) can be correlated to cracks and cavities (supposedly point defects, see discussion below) in the graphene covered P3HT film. In contrast, no cavities are visible on the film regions covered with double layer graphene (II), and these regions also exhibit no significant fluorescence degradation (Figure 4.3).

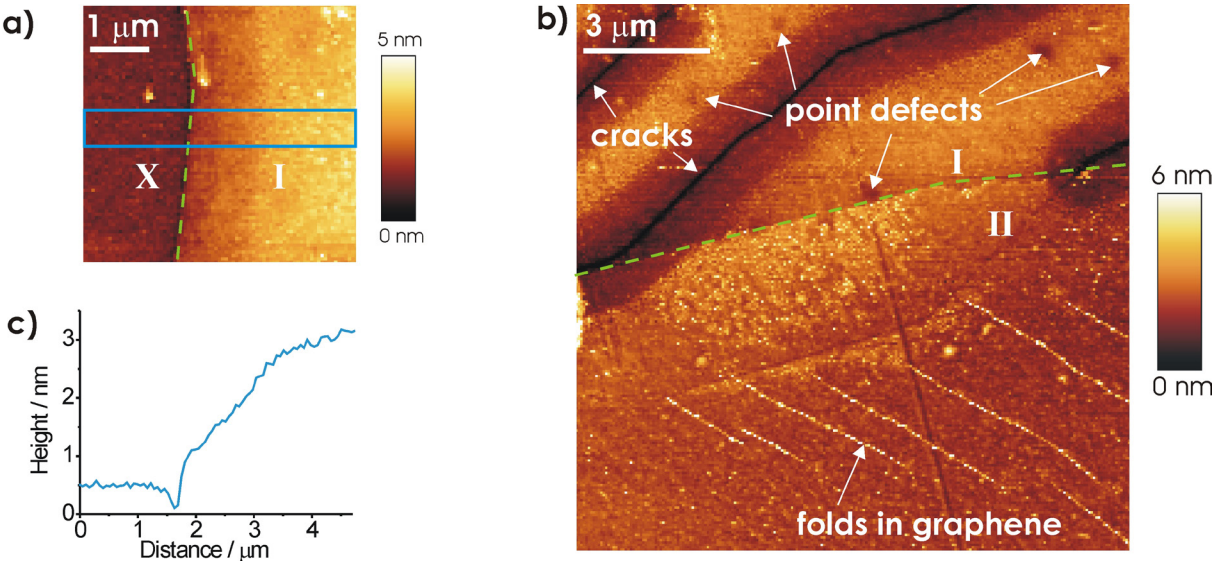

Figure 4.6. a) and b) SFM images of red marked regions indicated in Figure 4.3a. Images were taken after fluorescence investigation. (I) single layer graphene, (II) double layer graphene, and (X) uncovered P3HT film. c) Line average of blue marked region in a).

The volume loss of the uncovered P3HT film and the covered P3HT near the edge of the graphene layer (Figure 4.6a) is attributed to photochemical degradation and evaporation of the resulting reaction products after reactions with water and oxygen [109]. The cavities under the single layer graphene (see Figure 4.6b) are attributed to a volume loss of the subjacent P3HT film and are assumed to be centered at point defects in the single layer graphene that allow the permeation of bare water and oxygen and the photoreaction products.

4.1.5 Probability for formation of permeable defects in graphenes

As shown in chapters 4.1.3.2 and 4.1.4 single layer graphene on P3HT suffers from a slow photo-induced structure degradation.

In order to obtain the quantum yield for photo-induced formation of permeable defects in single layer graphene, the number of individual defects, visible as cavities on the SFM image (see last chapter, Figure 4.6b, ~ 0.2 defects per μm^{-2}), was related to the number of photons incident onto the single layer graphene in 44 h, providing a quantum yield for photo-induced defect formation of 10^{-19} defects per photon.

Double layer graphene in contrast remained free of permeable defects (see chapters 4.1.3.2 and 4.1.4). Still, there should be a small probability for the formation of permeable defects in a double layer graphene.

In the following the probability for formation of permeable defects in a multilayer graphene with the size A on P3HT will be estimated. A permeable defect in e.g. double layer graphene requires the penetration of both layers at the same site (see Figure 4.7).

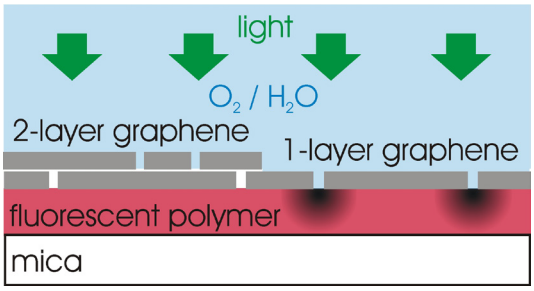

Figure 4.7. Sketch of P3HT on mica substrate protected from the ambient by graphene. The dark regions in the P3HT layer indicate regions of degraded fluorescence by water and oxygen permeation through graphene. A permeable defect in double layer graphene requires the penetration of both layers at the same site. Non co localized defects remain impermeable.

Assuming that the defects occur randomly in the single graphene layers and that the formation is uncorrelated between the m layers, the probability for the formation of permeable defects can be derived from the definitions of disjoint and independent events [110].

First the total number of defects k in one layer can be estimated from the total number of photons $N(t)$ incident onto the graphene layer in a time interval t and the quantum yield for photo-induced defect formation η:

$$k = N(t) \cdot \eta \,. \qquad \text{Eq. 4.4}$$

With the assumption that all defects have a defined size a (assumed to be ~ 1 nm^2 for a permeable defect), the total number of possible locations n for a defect within the area A can be estimated as

$$n = \frac{A}{a} \quad . \qquad \text{Eq. 4.5}$$

This estimate is only valid for $k << n$, which is the case in the described experiment and also for the estimations for graphenes with macroscopic size (see below).

The probability $P(B_{x,j})$ of the event $B_{x,j}$ to find a defect at the position x in the graphene layer j, for $x \in X = \{1, 2, 3, \ldots, n\}$ and $j \in J = \{1, 2, 3, \ldots, m\}$can thus be estimated to:

$$P\left(B_{x,j}\right) = P\left(\bigcup_{i=1}^{k} B_{x,j,i}\right) = \sum_{i=1}^{k} P\left(B_{x,j,i}\right) = k \cdot \frac{1}{n} \quad . \qquad \text{Eq. 4.6}$$

Assuming that permeable defects in mulitilayer graphene result only from m co-localized defects in m layers, the probability $P(B_x)$ for the formation of a permeable defect at the position x amounts to:

$$P\left(B_x\right) = P\left(\bigcap_{j=1}^{m} B_{x,j}\right) = \prod_{j=1}^{m} P\left(B_{x,j}\right) = \left(k \cdot \frac{1}{n}\right)^m \quad . \qquad \text{Eq. 4.7}$$

Now one can calculate the probability $P(C)$ of finding not a single defect at any position x, i.e. the probability that the graphene remains impermeable:

$$P\left(C\right) = P\left(\bigcap_{x=1}^{n} C_x\right) = \prod_{x=1}^{n} P\left(C_x\right) = \left(1 - \left(k \cdot \frac{1}{n}\right)^m\right)^n \quad , \qquad \text{Eq. 4.8}$$

with $P(C_x) = 1 - P(B_x)$.

The probability $P(D)$ for finding at least one defect (which would destroy the efficiency of the whole graphene layer) is then:

$$P(D) = 1 - P(C) = 1 - \left(1 - \left(k \cdot \frac{1}{n}\right)^{m}\right)^{n} . \qquad \text{Eq. 4.9}$$

With this one obtains a probability of 10^{-6} for the formation of at least one permeable defect in the double layer graphene (~ 300 μm^2) displayed in Figure 4.3. This is an upper limit of the probability, since the layer, which is not in contact with the P3HT should degrade slower.

One can also predict the probability for formation of permeable defects in graphenes with technological relevant sizes. Assuming a double layer graphene used as ultra-barrier to cover one square centimeter of an organic solar cell, that is exposed to sunlight (~1 kW/m^2) for 10.000 hours, one obtains a probability for formation of at least one defect permeable to water and oxygen of 10^{-2}. This indicates that double layer graphene meets the technological requirements of barrier material also on a macroscopic scale. Much larger graphene barriers require a triple layer graphene, for which the probability for permeable defects is 10^{-6} even for a barrier size of one square meter.

4.1.6 Water vapour and oxygen permeation rates through graphenes

In the following an estimation of the water vapour and oxygen transmission rates through graphene will be presented based on the Stern-Volmer equation [72]. The estimation requires knowledge of the time dependency of the fluorescence evolution of graphene covered P3HT and the deconvolution of P3HT fluorescence degradation from initial fluorescence enhancement through improved π-stacking (see chapter 4.1.3.2).

In order to investigate the time dependence of the P3HT fluorescence continuously over nearly two days, the fluorescence emanating from a ~ 2 μm^2 area centered under the double layer graphene was monitored in addition to imaging (see Figure 4.3) with an avalanche photo diode (Figure 4.8, blue curve). A small increase of the fluorescence can be detected over the first 17 h followed by a moderate decrease

over several hours in agreement with the fluorescence kinetics recorded by the camera (see Figure 4.3).

As a reference for the time dependence of the fluorescence under inert conditions, the fluorescence evolution was also recorded for P3HT films under continuous nitrogen flow and additionally covered with micron-thin pieces of mica. The thin flexible and undoubtedly impermeable mica pieces stick to the P3HT film surface and thus protect the P3HT from contact with possible water and oxygen contamination of the nitrogen.

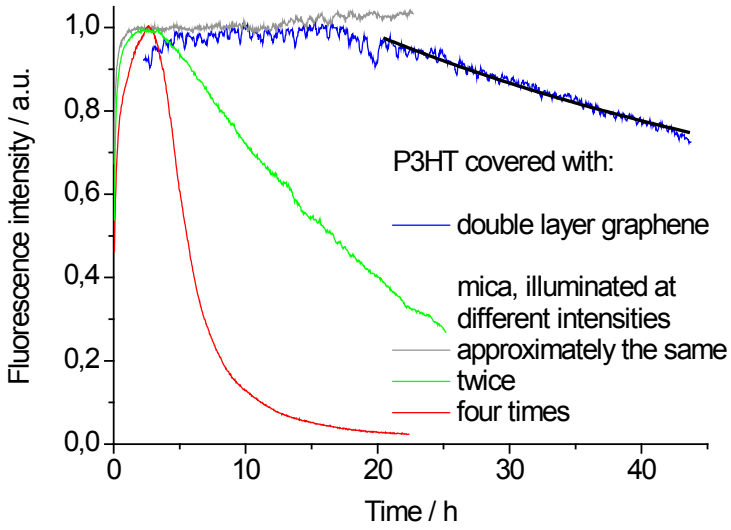

Figure 4.8. Time dependent fluorescence of a P3HT film covered with double layer graphene under ambient conditions (blue curve) and covered with mica under continuous nitrogen flow at approximately the same (grey curve), twice (green curve) and four times this illumination intensity (red curve). The interval of nearly constant fluorescence decay of the graphene covered P3HT is fitted by the Stern Volmer equation [72] (black curve), see also Eq. 4.10.

Figure 4.8 (grey, green and red curve) shows the fluorescence evolution of mica covered P3HT films, excited with different illumination intensities. The curves exhibit an initial asymptotic fluorescence increase (attributed to improved π-stacking), which is generally saturated after a few hours almost independent on illumination intensity. For illumination intensities comparable to the graphene sample (Figure 4.8, grey curve), the fluorescence increase is followed by nearly constant fluorescence over hours. An increase of the illumination intensity by a factor of two or higher already results in a strong fluorescence decay (Figure 4.8, green and red curve), which is attributed to intrinsic photo-induced P3HT degradation.

To estimate an upper limit for the water and oxygen permeation through graphene, it is assumed that the fluorescence decrease of P3HT covered by double layer graphene results from water or oxygen diffusing into the P3HT through the graphene with a constant rate ($\delta[Q]/\delta t$ = const), i.e. fast reaction of water and oxygen with P3HT and thus no saturation of P3HT with water and oxygen (given at the used illumination intensities, see Figure 4.2b). Any possible water and oxygen diffusion from the edge of the graphene layer as well as intrinsic fluorescence degradation is neglected (see chapter 4.1.3.2). The fluorescence decay $F(t)$ can be fitted by the Stern Volmer equation [72] with the fluorescence intensity F_0 of the quencher free P3HT at time t equal zero and the quencher diffusion rate $\delta[Q]/\delta t$ as unknown parameters (see black curve in Figure 4.8):

$$\frac{F_0}{F(t)} - 1 = K_{SV} \frac{\delta[Q]}{\delta t} t \,. \qquad \text{Eq. 4.10}$$

Any kind of possible interaction of the P3HT film with the substrate that could affect the absolute fluorescence intensity will not alter the estimation of the diffusion rate from the rate of change of the fluorescence as it is taken into account through the fit parameters F_0 and $\delta[Q]/\delta t$.

With the Stern Volmer constant K_{SV} of oxygen in P3HT (6.7 M^{-1}, smallest possible quenching efficiency [18]) one obtains a maximum molar oxygen diffusion rate of $\delta[O_2]/\delta t$ of 6 x 10^{-2} M day^{-1}, neglecting any possible water diffusion.

The estimated molar oxygen diffusion rate should also account for an upper limit of the molar water diffusion rate under the used experimental conditions (sufficient time and illumination intensity for reaction), since the quenching efficiency is dominated by exciton diffusion to the quenching center (reacted oxygen or water) and not by diffusion of the quenching center itself [111].

The diffusion rate can be converted into an upper limit of the permeation P:

$$P = \frac{\delta[Q]}{\delta t} d \,, \qquad \text{Eq. 4.11}$$

where d is the thickness of the polymer film. It yields an upper limit for the WVTR and OTR of 5×10^{-6} g m^{-2} day^{-1} and 6×10^{-3} cm^3 m^{-2} day^{-1}, respectively, including the error of the P3HT film thickness. From this one obtains an upper limit for the transmission rates through single layer graphene, since no significant difference is observed for the fluorescence intensity distribution of film regions covered with defect free single and double layer graphene (Figure 4.4).

This should be the currently most sensitive experimental estimation of the water and oxygen permeation through graphene (two orders of magnitude more sensitive than the previously reported measurement of the air leak rate [108]). Since the observed defect density is at least one order of magnitude below the average density of intrinsic lattice vacancies in the first monolayer of natural [101] and highly oriented pyrolytic graphite (HOPG) [102,103], it is suggested that intrinsic lattice vacancies are impermeable to water and oxygen within the detection sensitivity of the used setup. Furthermore, the used method is two orders of magnitude more sensitive than commercially available MOCON water sensors and as sensitive as MOCON oxygen sensors (MOCON, Minneapolis, USA). The established calcium test widely used to determine permeation constants of technologically relevant barrier materials is only sensitive to water vapour [112]. The suggested method allows quite generally to estimate the combined water and oxygen permeation of thin films like metal oxides, polymers and epoxies.

4.1.7 Conclusions

In conclusion defect free single and double layer graphenes efficiently protect a fluorescent semiconducting polymer film from degradation under ambient with WVTR and OTR reaching the technological requirements on ultra-barriers. However, single layer graphene suffers from a slow structural degradation with a quantum yield of about 10^{-19} defects per photon. In contrast double layer graphene remains free of permeable defects, which is attributed to the structural independence of the two single layers. With these data, one would predict that double layer graphene used as ultra-barrier to cover one square centimeter of an organic solar cell would be

largely defect free for more than 10.000 h of operation, and that triple layer graphene could offer protection up to a size of one square meter. This suggests that graphenes can function as both transparent electrode and barrier layer in future optoelectronic devices.

4.2 Probing graphene plasmons with fluorescent molecules

4.2.1 Introduction

Surface plasmons (SPs) are propagating charge density oscillations at the interface of a conductor and a dielectric. This and their strong confinement, the origin of plasmon induced field enhancement, renders them interesting for application such as light harvesting [113], Raman spectroscopy [59] and quantum information processing [34].

SPs are not limited to the interface between a conducting bulk substrate and a dielectric but they may also exist near quasi 2D conducting layers like graphene. The solution of Maxwell's equations for a p-polarized wave localized near a 2D layer with a conductivity σ provides the plasmon dispersion relation [34,60]:

$$\lambda_{sp} \approx \frac{2\pi}{\mathrm{Re}\left(i\left(\varepsilon+1\right)\varepsilon_0\,\omega/\sigma\right)}, \qquad \text{Eq. 4.12}$$

with λ_{sp} being the wavelength and ω the frequency of the plasmon, ε the dielectric function of the dielectric medium at the interface to the 2D layer and ε_0 the vacuum permittivity.

The existence of such a 2D plasmon with a finite wavevector requires a non-vanishing imaginary part of the conductivity σ at the frequency of interest [34], as demonstrated for graphene in the infrared [29]. In contrast, in the visible spectral range the conductivity of graphene, even for strong dopings, was predicted to be primarily real, both within the tight binding model (TBM) [51] and the TBM based random phase approximation (RPA) [34]. These are the predominantly used models in the field of graphene plasmonics and graphene is thus believed to be plasmon inactive in the visible spectral range.[29,34,35]

In the following it will be discussed that TBM [51] and TBM based RPA [34] at optical frequencies contradicts both recent experiments and more accurate theoretical descriptions of graphene. The graphene plasmon dispersion in the visible will be derived from the optical properties of graphene as measured by ellipsometry and

simulated by density functional theory (DFT). Furthermore it will be discussed how to excite graphene plasmons in the visible.

4.2.2 Dispersion relation of graphene plasmons in the visible

Precise ellipsometry measurements of the graphene refractive index for the visible spectral range have been recently reported.[45,58] The refractive index *n* of graphene can be converted into its sheet conductivity σ using the relation [27,55,56]:

$$\sigma = i\omega\varepsilon_0 d\left(n^2 - 1\right), \qquad \text{Eq. 4.13}$$

with *d* being the thickness of the graphene layer. Substitution of the experimentally acquired refractive index of graphene into Eq. 4.13 reveals that the real and imaginary parts of graphene's complex conductivity in the visible range are of comparable magnitude (at least for graphene on a solid substrate), in contrast to theoretical predictions by TBM and TBM based RPA (see last chapter) [34,51]. The real part of the graphene conductivity derived from the refractive index (Figure 4.9a dashed green and black curves) in the infrared/red wavelength regime is close to the value of $\sigma_0 = e^2/4\hbar$, which is predicted by the Dirac cone approximation of the TBM [27] and experimentally derived from the optical absorption of freely suspended graphene [46]. Also in agreement with absorption measurements of freely suspended graphene the real part of the conductivity in the green and blue wavelength regime deviates significantly from predictions by the Dirac cone approximation and the TBM, which is attributed to the unreasonable single-particle model for this wavelength regime.[46] Since an absorption measurement is rather insensitive to the imaginary part of the conductivity of graphene,[56] it does not contradict the complex conductivity derived from refractive index measurements of graphene (see Figure 4.9a).

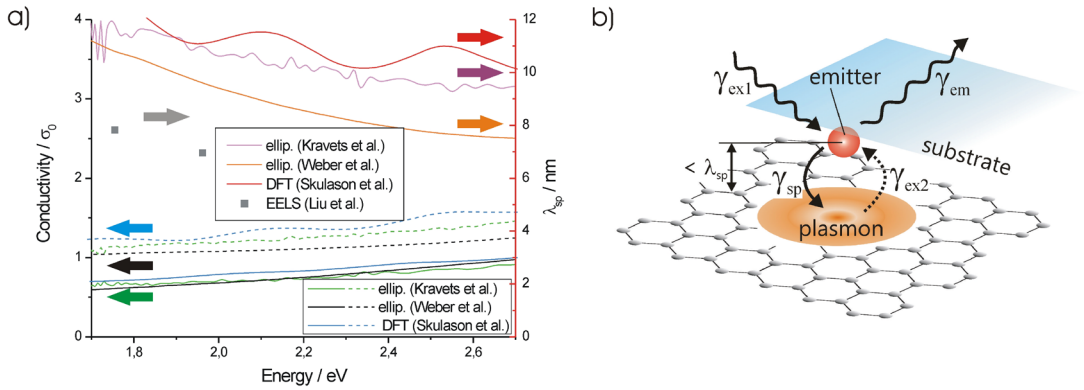

Figure 4.9. a) Left axis: Real and imaginary parts (dashed and solid curves, respectively) of the conductivity of graphene in units of the universal conductivity $\sigma_0 = e^2/4\hbar$ calculated (Eq. 4.13) from the experimental (green and black curves) and theoretical (blue curves) refractive indices. Refractive indices adaopted from ref. [45] (Kravets et al.), ref. [58] (Weber et al.) and ref. [56] (Skulason et al.). Right axis: plasmon dispersion (Eq. 4.12) for graphene on a solid substrate (here $\varepsilon = 2.6$) calculated from the imaginary part of the conductivity (pink, orange and red curves). Grey squares are plasmon wavelengths for graphene on mica recalculated from the plasmon wavelength for graphene on silicon carbide (SiC) provided by EELS (ref. [32], Liu et al.) with respect to the dielectric constants of SiC (6.9) [114] and mica (2.6) [115]. b) Diagram of the experiment: graphenes were exfoliated onto a mica substrate covered with a submonolayer of R6G molecules. Direct excitation of graphene plasmons by the far-field (γ_{ex1}) is not possible due to the large wavevector mismatch. However, fluorescent molecules in close proximity to graphene can efficiently excite graphene plasmons (γ_{sp}), since they provide the large wavevectors, existing in the near-field of the emitters, necessary for graphene plasmon excitation. Excited graphene plasmons can subsequently re-excite the emitters (γ_{ex2}).

Furthermore, the complex conductivity of graphene is in good agreement with predictions by density functional theory (DFT) (see Figure 4.9a), which in contrast to TBM and TBM based RPA is not only dominated by electronic transitions in the vicinity of the *K* points, but also includes significant contributions from electronic transitions along the ΓK and ΓM directions.[54,56] Therefore DFT calculations support graphene plasmons in the visible spectral range for undoped graphene as well as doping induced graphene plasmon enhancement also at plasmon energies well above the Fermi level shift [116], in strong contrast to TBM based RPA [34].

The graphene plasmon dispersion is obtained by substitution of graphene's experimental conductivities into Eq. 4.12 yielding in the visible spectral range graphene plasmon wavelengths on the order of 10 nanometers (Figure 4.9a orange and pink curves), more than one order of magnitude below the wavelength of free space photons. Furthermore it is reasonable to expect the graphene plasmon dispersion curve in Figure 4.9a to converge to the graphene plasmon resonance in the

ultraviolet frequency region, where also direct optical excitation of graphene plasmons has been demonstrated [62].

The graphene plasmon dispersion curves derived from graphene's measured optical properties is in good agreement with investigations of graphene by electron energy loss spectroscopy (EELS), using electrons to excite graphene plasmons [32,33] (see Figure 4.9a). Additionally the results of EELS including higher order graphene plasmon modes in the ultraviolet [117] are in good agreement with DFT simulations [116].

The considerations above imply graphene plasmons being optically excitable also in the visible spectral range. However, efficient excitation of SPs requires matching of energy and momentum of the photons to the SPs.[59] Standard near-field configurations like total internal reflection at the surface of a prism do not allow efficient excitation of graphene plasmons in the visible spectral range since the increase of the wavevector scales with the refractive index of the prism [59] and therefore a refractive index of about 50 is required in order to match the wavevector of free space photons to the orders of magnitude larger wavevectors (shorter wavelengths) of the graphene plasmons in the visible spectral range.

Nevertheless, the large momenta needed to efficiently excite graphene plasmons can be provided by apertureless scanning near-field microscopy, successfully demonstrated to resolve graphene plasmon fields in the infrared,[29] and were predicted to exist in the near-field of a small emitter [59] located at a distance to graphene smaller than the graphene plasmon wavelength [34] of around 10 nm at optical frequencies.

In the following results on coupling of molecular emitters to graphene plasmons are presented. Graphenes are exfoliated onto transparent mica substrates covered with a submonolayer of rhodamine 6G molecules (R6G) to bring graphenes and the molecules in a subnanometer distance to each other (Figure 4.9b). Steady state and time resolved fluorescence measurements under ambient conditions were used to quantify the coupling efficiency of the emitters and graphene plasmons, i.e. to

quantify the fluorescence quenching efficiency of graphene (reduction of the emission rate γ_{em}).

The following chapters cover sample characterisation of R6G on mica and confined by graphenes. Absorption spectroscopy and scanning force microscopy were used to estimate the R6G surface coverage and orientation (chapters 4.2.3.1 and 4.2.3.2). Chapters 4.2.4.1 and 4.2.4.2 contain spectrally and time resolved fluorescence measurements of R6G on mica. Fluorescence quenching by graphenes in presented in chapter 4.2.4.3 followed by estimations of the impact of orientation dependent excitation and collection efficiency of the R6G fluorescence on measured fluorescence quenching (see chapters 4.2.4.4 and 4.2.4.5). Finally measured fluorescence quenching is compared to quenching expected from theory (chapter 4.2.5).

4.2.3 R6G surface coverage and orientation

4.2.3.1 Estimation of the R6G surface coverage on mica from absorption spectroscopy

In the following an estimation of the R6G surface density from an absorption spectroscopy measurement will be presented.

To determine the surface density of the molecules from an absorption measurement one needs to relate the absorbance to the surface density and the absorption cross section of the molecules. The absorption cross section of a molecule σ_{abs} is defined as the average power <*P*> absorbed by a molecule divided by the intensity *I* of a plane wave incident onto the molecule [59]:

$$\sigma_{abs} = \frac{\langle P \rangle}{I}. \qquad \text{Eq. 4.14}$$

In an ensemble measurement, a light beam with intensity *I* will be attenuated by [59]:

$$I(z) - I(z+dz) = -\frac{N}{V}\langle P(z) \rangle dz \qquad \text{Eq. 4.15}$$

after propagating an infinitesimal distance dz through a sample with a volume concentration of molecules N/V. The integration of this equation yields Lambert-Beer law in its general form.[59]

Considering now a sample with N molecules on a surface with the size S the light beam will be attenuated by

$$I(N) - I(N + dN) = -\frac{\langle P(N) \rangle}{S} dN \qquad \text{Eq. 4.16}$$

after passing the interface. Inserting Eq. 4.14 and integration of the equation yields

$$\ln\left(\frac{I(N)}{I_0}\right) = -\frac{N}{S}\sigma_{abs} \,, \qquad \text{Eq. 4.17}$$

with the intensity I_0 of the light beam incident onto the sample, the intensity $I(N)$ transmitted by the sample and the surface concentration of molecules N/S. Inserting measured absorption $-\ln(I(N)/I_0)$ into Eq. 4.17 allows to determine the corresponding molecule surface density. If the absorption measured with a spectrometer is displayed as $-\log(I(N)/I_0)$ (as in Figure 4.10) the measured signal needs to be multiplied by ln(10) to relate it to the right side of the equation above.

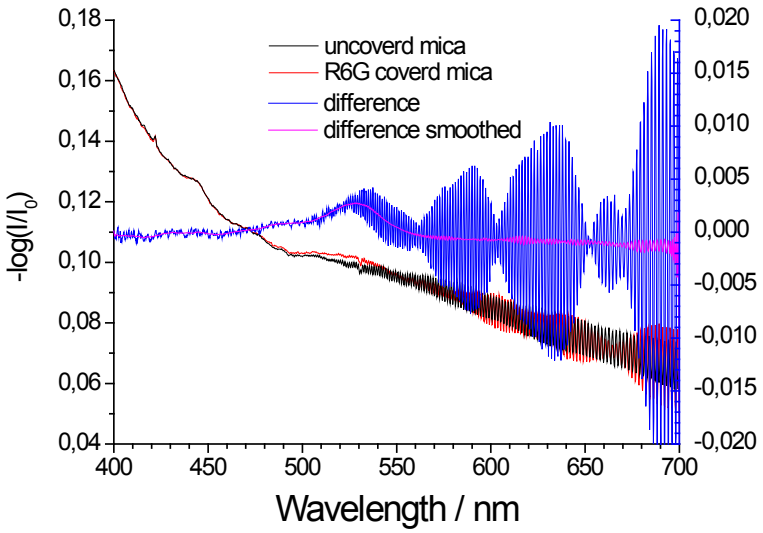

Figure 4.10. Left axis: Absorption spectrum of bare mica (black curve) and R6G covered mica (spincoated from 0.1 mM solution, red curve). Right axis: The difference of the absorption of R6G covered and uncovered mica (blue curve and pink curve (smoothed)) exhibits an absorption peak around 530 nm.

Figure 4.10 displays absorption spectra of R6G covered (red curve) and uncovered mica substrate (black curve) performed in a double beam absorption spectrometer with blank reference. The higher absorption (black and red curve) at shorter wavelengths is due to intrinsic absorption of the mica substrate. The oscillations (stronger at longer wavelengths) result from interference of the light beam reflections at the mica-air interfaces. After subtraction of the black curve from the red curve, the excess absorption of R6G around 530 nm becomes visible (blue curve (raw), pink curve (smoothed)), the measured signal is however close to the spectrometer accuracy (provided by the manufacturer), which results in a high experimental error. Substituting the measured peak absorption of 0.003 ± 0.002 (Figure 4.10) and the peak absorption cross section of R6G of $3 \pm 1 \times 10^{-16}$ cm^2 (peak absorption cross section of R6G in solution (unordered) is 4×10^{-16} cm^2 [118]; here light incidence perpendicular to the substrate is assumed and an angle between the absorption dipole of R6G and the substrate between 45° (corresponds to unordered) and about 60° (requires multiplication of literature value of the solution absorption cross section by $\cos^2(60°)/\cos^2(45°)$), corresponding to the orientation of cationic dyes on mica [119]) into Eq. 4.17, yields a surface coverage between 0.6×10^{13} cm^{-2} and 5.8×10^{13} cm^{-2}. These values correspond to a submonolayer coverage of R6G (see also next chapter).

4.2.3.2 Scanning force microscopy of humidity dependent topographies of graphenes

Graphene is known to follow the substrate topography even on a molecular scale. [6] Thus scanning force microscopy (SFM) measurements of graphenes confining R6G will be used in the following to confirm the assumed submonolayer thickness of R6G and to investigate the orientation of the confined molecules. This information is necessary to quantify effective fluorescence quenching by graphene (see chapters 4.2.4.4 and 4.2.4.5).

The first of the following two sections present humidity dependent topographies of graphenes on mica substrate. On this basis the second of the following two sections covers estimation of the R6G orientation and surface coverage from humidity dependent topographies of graphenes confining R6G on mica substrate.

Humidity dependent topography of graphenes

 It will be shown that a molecular thin, fluid water film is confined between mica and graphene under ambient condition. The results from this section will be used in the next section to proof the submonolayer thickness of R6G and to estimate the orientation of the R6G molecules.

Figure 4.11a-c displays SFM images of a single layer graphene prepared under ambient conditions on mica and imaged during purging the SFM chamber with dry nitrogen or with dry nitrogen bubbled through purified water. At 60% RH graphene is remarkably flat and virtually free of folds, cracks or any other structural defects, occasionally occurring on mechanically exfoliated graphenes. The flatness of graphene indicates the virtual absence of any confined large defects or contaminations (Figure 4.11a). At RH below 4%, small depressions in the graphene topography appeared growing into fractal structures (Figure 4.11b and c). The growth of fractals generally saturates on a time scale of hours (see reference [120]). Upon rapidly raising the humidity again, initially no noticeable change of the fractals was observed, while at about 50% RH the fractals disappeared quite abruptly (Figure 4.11c).

A subsequent image taken at 60±5% RH revealed a flat graphene surface. Upon purging again with dry nitrogen with the same flow rate a very similar growth of fractals occurred as observed initially. The overlay of the images reveals, however, that in defect free graphene the newly grown fractals grew from new nuclei, which indicates homogeneous nucleation. For graphene with defects like folds and edges, these can serve as nucleation center for the growth of fractals. Fractal growth was also observed in multilayer graphenes, however with coarser fractal shape for substantially thicker graphenes. No topography alteration (e.g. growth of fractals) upon variation of RH were observed on freshly cleaved HOPG surface (see reference [120]).

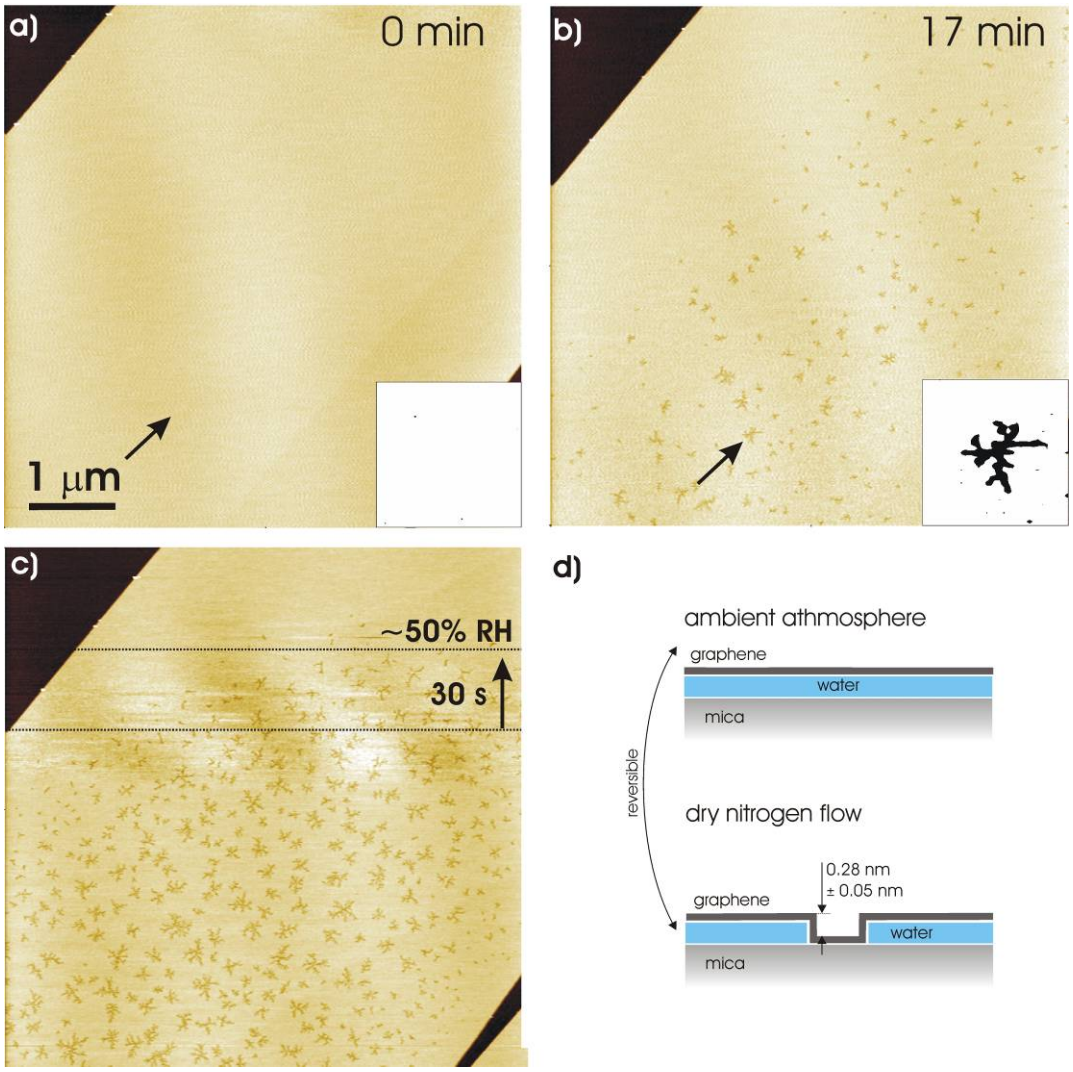

Figure 4.11. SFM images of single layer graphene (brighter area) deposited onto mica (darker area) at ambient conditions, and imaged during purging of the SFM chamber with dry nitrogen. The time noted at the beginning of each scan is indicated directly on the images; the time required to take one image was 3.2 minutes. Inserts show zooms (400 nm), into the area indicated with the arrow with strongly exaggerated contrast a) Initially, graphene is homogeneously flat. b) First depressions appear at RH below 4% and grow into fractal structures (see also lower half in (c)). c) Upon increasing the humidity graphene becomes again atomically flat. The black lines are guides to the eye, which indicate the erasure of fractals; the time elapsed between the lines is 30 seconds. A subsequently taken image revealed a flat graphene topography similar to a). d) Schematics of the proposed sample structure before and after dewetting of the water layer, indicated heights are the heights measured by SFM.

The depth of the fractals measured on graphene was 2.8±0.5 Å, which is comparable to the size of a water molecule [121].

The mica surface is known to be covered at ambient with a heterogeneous water film (islands of water molecules) with a thickness depending on the RH.[122] It is reasonable to assume that graphenes exfoliated at ambient conditions onto a mica

surface confine the water film at least initially. Graphene is known to be substantially flexible to follow the surface topography.[6] Furthermore, mechanically exfoliated single and multiple layer graphenes have been shown to be largely impermeable to small molecules.[108,123]

Therefore the reversible growth of fractal depressions in graphenes upon changing of the ambient humidity implies that an initially homogeneous water film confined between graphene and mica exhibits flow to the graphene edges, i.e. it is fluid in this semi-hydrophilic slit pore. This complies with the widely accepted view that an aqueous film confined to a hydrophilic sub-nanometer slit pore remains fluid.[124-126] Taking into account the recurrent refilling of the graphene-mica slit pore upon increasing the relative humidity, the film is attributed largely to water. The depth of the dewetting patterns is comparable to the size of a water molecule and substantially smaller than expected for a bi-layer of water molecules [121], which suggests the dewetting film to be monomolecularly thin.

The growth of fractal structures has been observed previously during dewetting of thin liquid films.[127-129] However, the largely impermeable soft graphene cover of the water film and its monomolecular thickness differentiates this case. The humidity dependent recurrent de/re-wetting of the film with exponential equilibration implies that the water molecules confined between graphene and mica are in dynamic equilibrium with the exterior water. The variation of the ambient humidity breaks the equilibrium, e.g. reduction of the ambient RH leads to desorption of water molecules, thereby reducing the density of the film and promoting nucleation of the dewetting. The growth of fractal objects with dimensions around 1.7 (dimensions of well developed fractal patterns in the graphene-mica) is typical for Laplacian growth processes [130], which are observed in a variety of physical situations, including the diffusion-limited aggregation (DLA) as the most prominent example [131]. Desorption events of the water molecules at graphene edges may create initially pinholes (point defects) in the film, which could then diffuse and merge with the growing fractals, equivalent to the DLA growth mechanism. The observed reversibility of fractal growth in the water film, however, suggests a similarity with the Saffman-Taylor instability [132] of a viscous film, here driven by the negative pressure developed in the film upon molecular desorption.

In summary it was shown that a molceular thin water film is confined between mica and graphene. The water film is reversibly dewettable upon changing RH with graphene following the water film in the flat and dewetted regions.

Humidity dependent topography of graphenes confining R6G

In this section dewetting of a film containing water and additionally R6G molecules will be used to estimate the surface density and the orientation of the dye molecules, replicated by graphene.

Figure 4.12a shows a SFM image of double layer graphene exfoliated onto R6G covered mica substrate (see sample preparation in chapter 3.8.3) and imaged at 30% relative humidity (RH). The topography exhibits plateaus and small elevations with a height of 0.34 ± 0.05 nm. The full width at half maximum (FWHM) of the small elevations is about 10 nm. It is noticeable that small elevations are rarely located between laterally larger plateaus. The surface density of the small elevations in the regions not exhibiting larger plateaus is on the order of $2x10^3$ per μm^2. Since graphene exfoliated onto mica substrate is known to be atomically flat under ambient condition [120] the elevations and plateaus on the SFM image (Figure 4.12a) are attributed to R6G molecules confined between mica and graphene. The fact that the small elevations are rarely located in between the laterally larger plateaus indicates that the plateaus consist of laterally closely packed elevations.

As a molecularly thin water layer is known to be confined between mica and graphene under ambient conditions, the regions between the elevations and plateaus should therefore contain water. This water layer should be dewettable upon lowering the humidity [120], which will be checked in the following.

Figure 4.12b displays the same regions as in a) after continuous purging with dry nitrogen for half an hour and finally imaged at 1.5% RH. Some areas in the regions between the elevations and plateaus now exhibit depressions with a depth of 0.28 ± 0.03 nm. Rising the humidity results in disappearance of the depressions (Figure 4.12c, imaged at 55% RH after continuous rising the humidity for the quarter of an hour). Thus the depression growing between the elevations and plateaus upon lowering the humidity are attributed to result from dewetting of the molecularly thin

water layer confined between mica and graphene additionally to the R6G molecules. The measured depth of the depressions (0.28 ± 0.03 nm) fits well to the depth of the depressions measured on graphene samples not containing R6G molecules additionally to water (see last section and ref. [120]).

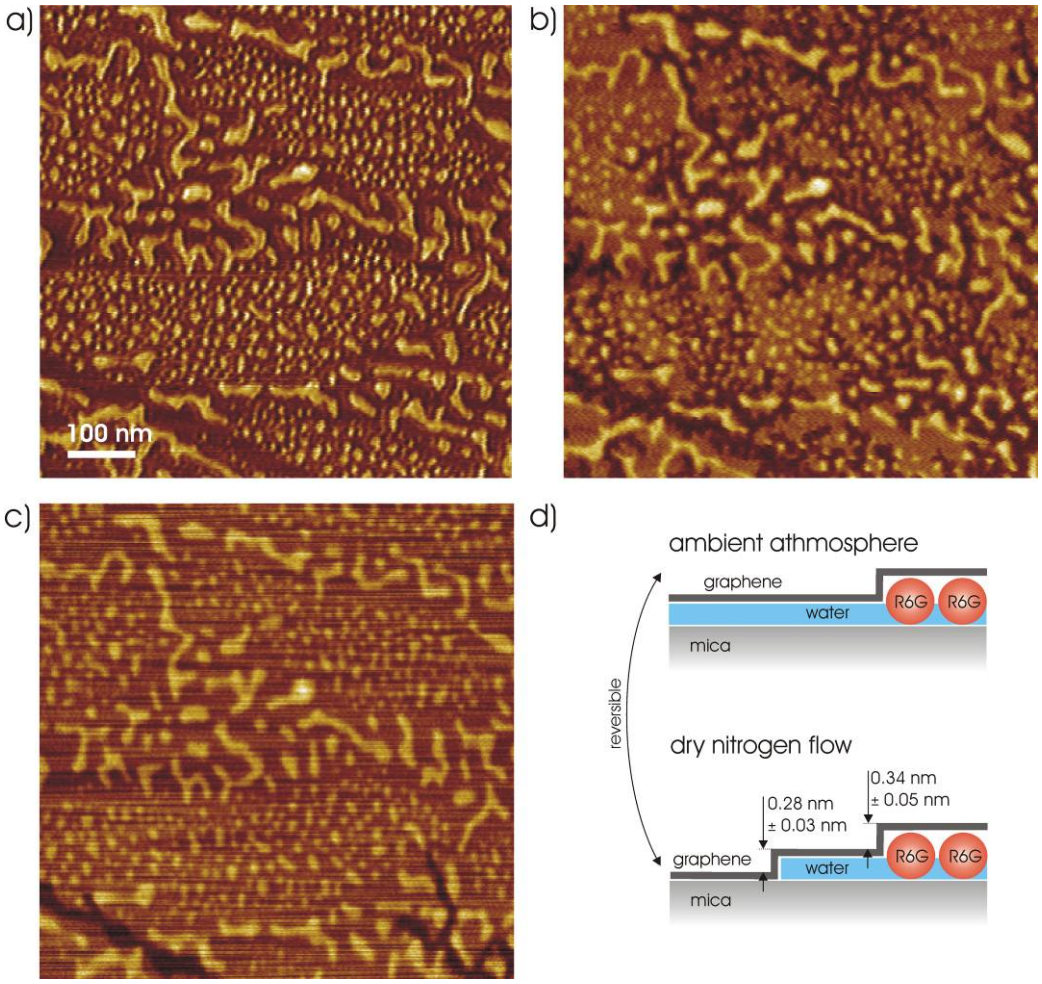

Figure 4.12. SFM images of double layer graphene exfoliated onto a R6G covered mica substrate (prepared from 0.1 mM) imaged at a) 30% RH, b) 1.5% RH after continuous drying for half an hour and c) 55% RH after continuous rising the humidity for the quarter of an hour. d) Schematics of the proposed sample structure before and after dewetting of the water layer, indicated heights are the heights measured by SFM (a and b).

By adding the height of the water layer to the height of the elevations (molecules) above the water layer the total apparent height of the R6G molecules is estimated to 0.62 ± 0.08 nm (see Figure 4.12d). As the thickness of a R6G molecule perpendicular to its plane is calculated to range between 0.5 nm and 0.85 nm (see ref. [133]) it is concluded that the molecules are approximately flatly confined between mica and graphene. Consequently it is assumed that the dipole moment of R6G is oriented approximately parallel to the graphene layer.

Assuming that the measured FWHM of the elevations corresponds approximately to the lateral extension of the elevations, that the R6G molecules are densely packed within the elevations and that the cross sectional area of a single flatly oriented R6G is 1.56 nm^2 (see ref. [133]) one can estimate a R6G surface density on the order of 10^5 molecules per μm^2 (equal to 10^{13} cm^{-2}).From the SFM measurements one can not exclude that some molecules are also located on top of graphene. However, since the estimation of the R6G surface density in the graphene and mica regions by contrast (see chapter 4.3.3.1) and absorption spectroscopy (see chapter 4.2.3.1), respectively, yield R6G surface densities on the same order as by SFM (see above), it is concluded that the R6G surface densities in the mica and graphene regions are on the same order.

4.2.4 Fluorescence of R6G on mica and confined by graphenes

4.2.4.1 Spectrally resolved fluorescence of R6G on mica

Fluorescence spectra of R6G on mica were recorded to verify the fluorescence maximum of R6G on mica under ambient conditions since this is a parameter needed for the calculation of quenching expected from theory. Additionally the spectra provide evidence that the short fluorescence lifetime of R6G on mica results from interaction of R6G with the mica substrate (see next chapter).

Figure 4.13 shows fluorescence spectra of R6G on mica substrate at different relative humidities and of R6G dissolved in water. The fluorescence spectrum of R6G on mica is even at high relative humidities (maximum at 544 nm at 81% RH) blue shifted (9 nm) with respect to the solution spectrum (maximum at 553 nm) (see also ref. [134]). Interestingly the blue shift of the spectrum is increased by reducing the relative humidity of the surrounding environment (e.g. to about 535 nm at 48% RH, the humidity range at which the fluorescence images were recorded, see chapter 4.2.4.3).

The observed blue shift of the fluorescence spectrum of R6G on mica could result from the lack of a solvent induced bathochromic shift (also observed for R6G in the gas phase) [135] and interaction of R6G with the mica substrate. Possible interaction mechanisms with the substrate are formation of a contact ion pair [136], ion

exchange with the mica surface [119] and charge transfer with the substrate [137]. Since the fluorescence of R6G on mica at high humidities is still blue shifted with respect to the fluorescence of R6G dissolved in water, the blue shift is attributed to a superposition of interaction with the mica substrate and the lack of a bathochromic shift.

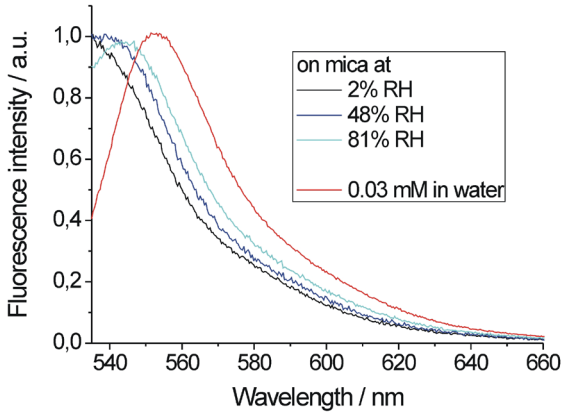

Figure 4.13. Fluorescence spectra of R6G in water (0.03 mM, red curve) and of R6G on mica surface spincoated from 0.03 mM solution at varying humidities (2% RH, black curve; 48% RH, blue curve; 81% RH, light blue curve).

4.2.4.2 Time resolved fluorescence of R6G on mica

In order to estimate the total decay rate $\gamma^s = 1/\tau^s$ of R6G on mica, with τ^s being the measured dominating fluorescence lifetime, time resolved fluorescence decay measurements (Figure 4.14) were performed. This parameter is necessary to compare measured quenching and quenching expected from theory (see chapter 4.2.5). A double exponential decay was found to fit the data, similarly as for rhodamines on other substrates [137]. The resulting fluorescence life times are 0.28 ± 0.02 ns and 0.89 ± 0.05 ns with the amplitude of the faster decay being more than one order of magnitude stronger.

The dominating lifetime of R6G on mica is about one order of magnitude shorter compared with lifetimes of rhodamines in solutions [138] which can be attributed to an increase of the non-radiative decay rate resulting from interaction with the substrate [137]. Substrate interaction is also indicated by fluorescence spectra of R6G on mica (see chapter 4.2.4.1).

Furthermore, by assuming the radiative decay rate of R6G on mica under ambient conditions being equal to the radiative decay rate of R6G in water (2.2×10^8 s^{-1}, see ref. [138]), the domination fluorescence lifetime of R6G on mica (0.28 ± 0.02 ns, see above) yields a fluorescence quantum yield (see Eq. 2.46) of R6G on mica of $\phi_m = 0.062 \pm 0.005$.

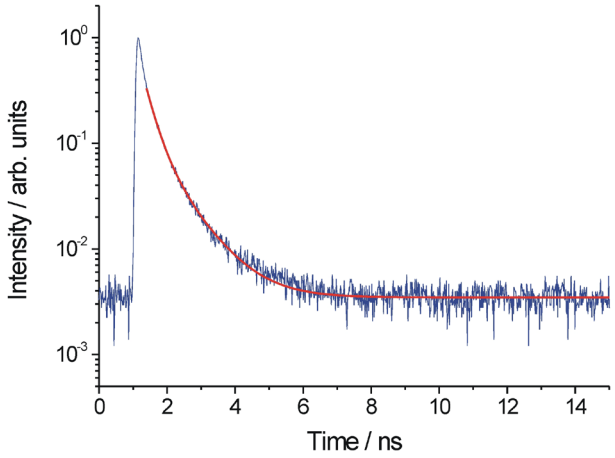

Figure 4.14. Time resolved fluorescence decay of R6G on mica excited at 532 nm (blue curve). A double exponential decay fits the data (red curve). The resulting fluorescence life times are 0.28 ± 0.02 ns and 0.89 ± 0.05 ns with the amplitude of the faster decay being more than one order of magnitude stronger.

4.2.4.3 Fluorescence quenching by graphenes

Fluorescence imaging is used to quantify fluorescence quenching by graphenes.

Figure 4.15a shows a reflection microscopy image of graphenes exfoliated onto a submonolayer of R6G on a mica substrate. Graphenes appear dark on the mica substrate. The region marked with (I) exhibits a contrast of $10.5\% \pm 0.3\%$ on the background (X) and can thus be identified as single layer graphene.[88]

Figure 4.15b shows a fluorescence image of the same sample region displayed in a). Graphene covered regions (I) appear darker in comparison to the bright fluorescence emitted from the uncovered R6G (X), which is attributed to quenching of the R6G fluorescence by the graphenes. Single layer graphene exhibits an apparent quenching factor of $q \equiv I_m/I_g = 5.2 \pm 0.7$, with I_m and I_g being the fluorescence intensities of uncovered and graphene covered areas respectively, i.e. the mean of the intensity histograms in (c) (quoted error is the standard deviation of the mean from different

samples). Only a weak increase of the quenching factor with the number of graphene layers is observed: e.g., 6 ± 1 layers of graphene quench the fluorescence by a factor of 8.2 ± 1.2 (not shown).

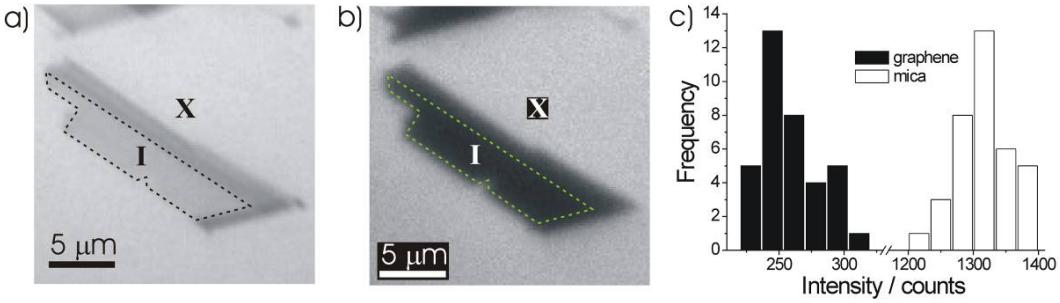

Figure 4.15. a) Reflection microscopy image of graphenes on R6G covered mica substrate. Single layer graphene is outlined with the black dashed line and marked with (I), regions not covered by graphenes with (X). b) Fluorescence microscopy image of the sample region displayed in (a). Single layer graphene (I) is outlined with the green dashed line. c) Fluorescence intensity histograms from single layer graphene covered (I, black bars) and uncovered (X, white bars) areas, respectively. Fluorescence of molecules under single layer graphene is significantly quenched, but still detectable.

However, the apparent fluorescence quenching of R6G by graphenes is rather a lower limit of the quenching factor: first of all scanning force microscopy investigation of the graphene covered R6G submonolayers have shown that R6G is confined flatly by graphene (transition dipole moment parallel to graphene, see chapter 4.2.3.2) while uncovered cationic dye molecules are known to adsorb rather disordered on mica [119], which is also reasonable for (cationic) R6G. This and an additional possible red shift of the R6G absorption in the graphene region results in a higher excitation and collection efficiency of R6G fluorescence in the graphene region. The corrections necessary for equal excitation and emission detection conditions of the R6G fluorescence in the mica and graphene regions will be discussed in the following two chapters.

4.2.4.4 Excitation efficiency of R6G in the mica and graphene regions

In this section the impact of the excitation efficiency of R6G in the mica and graphene regions on the apparent quenching factor will be estimated. The excitation efficiency of R6G in the mica and graphene regions might vary due to different orientations of R6G and spectral shifts of the R6G absorption in the mica and

graphene regions which both can affect the absorbed power. First the orientations of R6G in the mica and graphene regions will be shortly discussed.

Using SFM it has been shown that R6G is confined flatly between mica and graphene (see chapter 4.2.3.2). However, cationic dye molecules (crystal violet and malachite green) are known to adsorb on mica with a maximum angle between the plane of the molecule and the mica substrate of about 60° or rather unordered (average tilt angle of 45°).[119] These orientation are also reasonable for (cationic) R6G on mica, and for these the estimation of the R6G surface density from absorption spectroscopy measurements (see chapter 4.2.3.1) of uncovered R6G on mica is in good agreement with the estimation from SFM of R6G confined between mica and graphene (see chapter 4.2.3.2). Consequently the different orientation of R6G in the regions covered and not covered by graphene might influence the apparent quenching factor.

In the following the dependency of the excitation efficiency of R6G on the illumination aperture and the orientation of the R6G absorption dipole will be estimated.

The samples were illuminated through the object lens. Since the microscope used for fluorescence imaging is not equipped with an aperture stop, the illumination aperture and accordingly the maximum illumination angle α is equal to the aperture of the object lens ($NA = 0.55$, $\alpha \cong 33°$). This can be described as an effective illumination angle $\alpha' \cong 24°$, which will be shown in the following.

The intermediate image of the light source is assumed to be a uniform bright round area with radius r and the circles around its centre being linearly distributed onto the illumination angles (only a point source will result into NA = 0). Furthermore, using that the centre r' of an area of a segment of a circle with radius r is equal to $r' = r/\sqrt{2}$ and that α/r is the optical invariant [139], the effective illumination angle can be estimated to $\alpha' = \alpha/\sqrt{2} \cong 24°$ (Figure 4.16a).

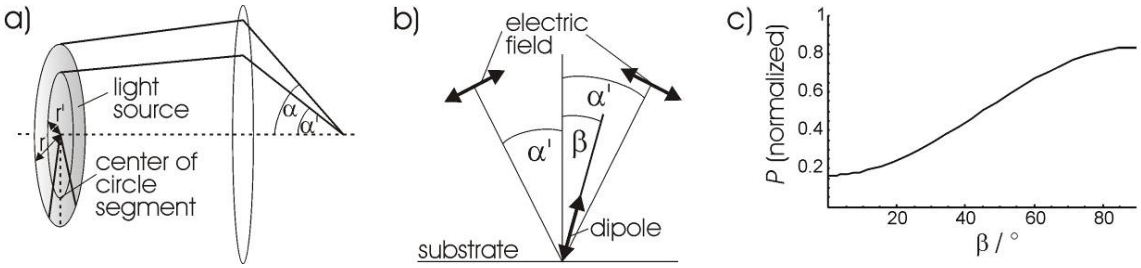

Figure 4.16. a) Sketch for the estimation of the effective illumination angle α´ from the maximum illumination angle α (corresponding to the illumination aperture) and the radius of the intermediate image of the light source r using that α/r is the optical invariant of the system. b) Sketch for the calculation of the illumination aperture and dipole orientation dependent absorption, with β being the angle between the absorption dipole and the optical axis and α' the effective illumination angle. c) Dependency of the absorbed power P on the dipole orientation β for an illumination aperture NA = 0.55.

To estimate the dependency of the excitation efficiency of R6G it is now used that the power absorbed by a dipole is proportional to the square of the electric field projected onto the dipole [59] (Figure 4.16b), which can be written as:

$$P \propto \left|\sin(\alpha'-\beta)\right|^2 + \left|\cos(90-\alpha'-\beta)\right|^2, \qquad \text{Eq. 4.18}$$

with α' being the effective illumination angle and β being the angle between the axis of the dipole and the optical axis. A dipole parallel to the optical axis will absorb 0.17, 45° to the optical axis 0.5, 30° to the optical axis (60° to the substrate) 0.33 and 90° to the optical axis 0.83 of the maximum possible absorbed power (Figure 4.16c). From this one can estimate that the maximum orientation dependent variation of the absorbed power is smaller than a factor of 0.83/0.17 (≅ 4.9). In particular one can estimate that corresponding to the orientation of R6G under graphene a dipole parallel to the substrate will absorb 1.7 times more than a dipole tilted 45° and 2.5 times more than a dipole tilted 30° to the optical axis (equal to a tilt of 60° to the substrate), corresponding to the orientations of R6G on mica.

Additionally the absorption maximum of R6G in the graphene regions might be red shifted (see ref. [36] and chapter 4.3.3.1) to the absorption of R6G in the mica region (see chapter 4.2.3.1) and could consequently be closer to the used emission maximum of the microscope lamp (546 nm). This implies an up to three times higher excitation efficiency of R6G in the graphene region.

The apparent quenching factor needs to be multiplied by the discussed factors (geometrical and spectral correction) to provide equal excitation conditions in the mica and graphene regions, i.e. effective quenching is here higher than apparent quenching.

4.2.4.5 Collection efficiency of the R6G fluorescence in the mica and graphene regions

Besides the excitation efficiency (see last chapter) also the collection efficiency of the R6G fluorescence in the mica and graphene regions depends on the orientation of R6G and can thus impact the apparent quenching factor.

In the following an equation for the estimation of the collection efficiency of the object lens is derived, related to the numerical aperture of the object lens, the orientation of the R6G emission dipole and the transmittance of the mica substrate.

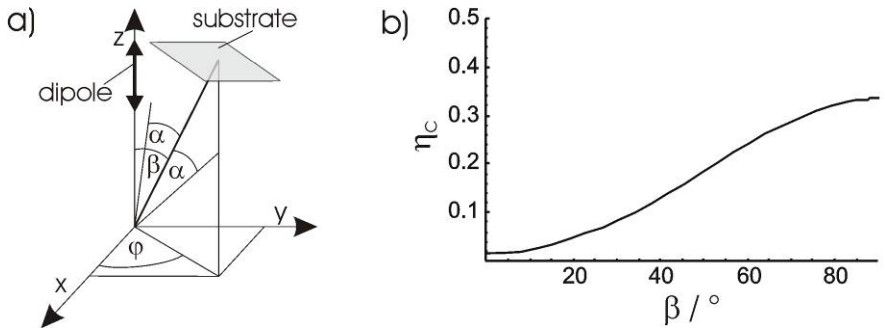

Figure 4.17. a) Sketch for the calculation of the illumination aperture and dipole orientation dependent collection efficiency, with β being the angle between the emission dipole and the optical axis and α the maximum collection angle of the object lens (representation of the dipole in a spherical coordinate system) [59]. b) Dependency of the collection efficiency η_c on the dipole orientation β for an object lens aperture of NA = 0.55.

The power of a dipole in a homogeneous environment $P(\vartheta,\varphi)$ radiated into an infinitesimal small unit solid angle $d\Omega = sin(\vartheta)d\vartheta d\varphi$, expressed in spherical coordinates with the dipole pointing along the z-axis and normalized by the total radiated power $\bar{P}$ is given by [59]:

$$\frac{P(\vartheta,\varphi)}{\bar{P}} = \frac{3}{8\pi}\sin^2(\vartheta). \qquad \text{Eq. 4.19}$$

The fraction η_c of the total emitted power transmitted through a substrate with the transmittance T and collected by an object lens with an aperture angle α (maximum collection angle) smaller than the critical angle of total internal reflection (which is given here) can be calculated by integration of the equation above with respect to the transmittance [140]:

$$\eta_C = \frac{3}{16\pi}\left(\begin{array}{l}\int_{-\pi}^{\pi}\int_{0}^{\alpha+\beta} T(\vartheta-\beta)\sin^3(\vartheta)\,d\vartheta\,d\varphi \\ +l\int_{-\pi}^{\pi}\int_{0}^{\alpha-\beta} T(\vartheta+\beta)\sin^3(\vartheta)\,d\vartheta\,d\varphi\end{array}\right), \qquad \text{Eq. 4.20}$$

with β being the angle between the optical axis and the dipole axis and $l = 1$ for $\alpha > \beta$ and accordingly l = -1 for $\alpha < \beta$ (see Figure 4.17a).

The transmittance of the substrate is calculated from the Fresnel transmission coefficients of the air-mica and mica-air interfaces. Defining the plane of incidence being parallel to the dipole axis, the transmittance of the air-mica interface is related to the transmission coefficient t_1^p for parallel polarized waves. Since mica is birefringent and thus the p-polarized wave is split into a p- an s-polarized part during propagation through the substrate, the transmission coefficients t_2^p and t_2^s for p- and accordingly s-polarized light need to be considered for the transmittance of the mica-air interface. As mica substrates with a thickness of at least several micrometers were used, the light is assumed to be approximately unpolarized upon reaching the mica-air interface (equally distribution of p- and s-polarized light, as summation over dipoles with arbitrary orientation to the mica crystal axes parallel to the cleaved mica surface). The transmittance is thus estimated to:

$$T = \left(t_1^p \frac{\left(t_2^p + t_2^s\right)}{2}\right)^2, \qquad \text{Eq. 4.21}$$

with the transmission coefficients t_1^p, t_2^p and t_2^s equal to:

$$t_1^p = \frac{2\, n_{air} \cos(\gamma_1)}{n_{mica} \cos(\gamma_1) + n_{air} \cos(\gamma_2)}, \qquad \text{Eq. 4.22}$$

$$t_2^p = \frac{2\, n_{mica} \cos(\gamma_2)}{n_{air} \cos(\gamma_2) + n_{mica} \cos(\gamma_1)} \text{ and} \qquad \text{Eq. 4.23}$$

$$t_2^s = \frac{2\, n_{mica} \cos(\gamma_2)}{n_{mica} \cos(\gamma_2) + n_{air} \cos(\gamma_1)}. \qquad \text{Eq. 4.24}$$

The refraction index of air and mica is given by n_{air} = 1 and n_{mica} = 1.596, respectively and the angle of incidence γ_1 ranging from $\{0 \ldots \alpha\}$ and transmission γ_2 are related through Snell's law of refraction by $\gamma_2 = \arcsin(n_{air}/n_{mica} \sin(\gamma_1))$.

The numerical aperture of the object lens (NA = 0.55) yields a maximum collection angle $\alpha \cong 33°$. If the dipole axis is parallel to the substrate (corresponding to R6G under graphene, $\beta = 90°$) a collection efficiency of 0.33 is obtained. An unordered orientation of the dipoles ($\beta = 45°$) or an angle between the substrate and the dipole axis of 60° ($\beta = 30°$) (corresponding to R6G on mica) yields a collection efficiency of 0.16 and 0.08, respectively (see Figure 4.17b). This means that the light emission from molecules with emission dipole parallel to the substrate surface is collected 2.1 times more efficient than from molecules with the emission dipole oriented 45° to the substrate surface and 4.1 times more efficient than from molecules with the emission dipole orientated 60° to the substrate surface.

The apparent quenching factor needs to be multiplied by the discussed geometrical factors to provide equal conditions for the collection of the R6G fluorescence in the mica and graphene regions. To obtain the effective quenching factor both the correction factors for equal conditions for the fluorescence collection and excitation (see last chapter) must be included.

Correcting the apparent quenching factor (see chapter 4.2.4.3) for equal excitation and emission detection conditions of the R6G fluorescence in the mica and graphene regions an effective quenching factor q_{eff} between 16 and 181 is obtained.

4.2.5 Estimation of fluorescence quenching expected from theory

In the following the results on measured quenching through graphene (effective quenching factor q_{eff} between 16 and 181, see chapters 4.2.4.3, 4.2.4.4 and 4.2.4.5) will be compared to that expected from theory.

The effective quenching factor equals the ratio of the R6G fluorescence emission rates (intensity) in the mica and graphene regions γ_{em}^{s} and γ_{em}^{g}, respectively:

$$q_{eff} \equiv \frac{\gamma_{em}^{s}}{\gamma_{em}^{g}}. \qquad \text{Eq. 4.25}$$

The fluorescence rate in the mica region can be written as (see also ref. [141]):

$$\gamma_{em}^{s} = \gamma_{ex}^{s} / \left(\gamma^{s} / \gamma_{r}\right), \qquad \text{Eq. 4.26}$$

with γ_{ex}^{s} being the excitation rate, γ_{r} the radiative rate and γ^{s} the total decay rate in the mica region. Accordingly the fluorescence rate in the graphene region can be written as:

$$\gamma_{em}^{g} = \gamma_{ex}^{g} / \left(\gamma^{g} / \gamma_{r}\right). \qquad \text{Eq. 4.27}$$

Substitution of Eq. 4.26 and Eq. 4.27 into Eq. 4.25 and rearranging the same gives

$$\left(\gamma_{ex}^{g} / \gamma_{ex}^{s}\right) / \left(\gamma^{g} / \gamma_{r}\right) = \gamma_{r} / \left(q_{eff}\, \gamma^{s}\right) \equiv \gamma_{em}^{norm}, \qquad \text{Eq. 4.28}$$

which is referred in the following to as the normalized fluorescence rate γ_{em}^{norm}. $\left(\gamma_{ex}^{g} / \gamma_{ex}^{s}\right)$ deviates from unity only if local excitation enhancement is present (e.g. in the case of plasmon active metal surfaces) [141]. The normalized fluorescence rate relates the radiative rate to the total decay rate induced by graphene and is thus a proper quantity to compare quenching measured in different experimental configurations (e.g. varying substrate induced decay). Therefore the measured effective quenching factor (see chapters 4.2.4.3, 4.2.4.4 and 4.2.4.5) will be

converted into the normalized fluorescence rate using Eq. 4.28. For this γ_r and γ^s are required.

Assuming the radiative decay rate γ_r for R6G in the mica and graphene regions under ambient conditions being equal to the radiative decay rate of R6G in water of $2.2\text{x}10^8$ s^{-1} (ref. [138]) and with $1/\gamma^s = 0.28 \pm 0.02$ ns (see chapter 4.2.4.2) and q_{eff} between 16 and 181 (see chapters 4.2.4.3, 4.2.4.4 and 4.2.4.5) this yields according to Eq. 4.28 a measured normalized fluorescence rate between $3.2\text{x}10^{-4}$ and $4.1\text{x}10^{-3}$. This experimental result will now be compared with theoretical predictions.

The normalized total decay rate γ^g/γ_r in the graphene region (including excitation of plasmons and electron hole pairs) for an emission dipole parallel to the graphene surface (like in this experiment, see chapter 4.2.3.2) can be calculated from graphenes optical conductivity σ at the emission frequency ω of the emitter [34] (emission maximum at about 535 nm, see chapter 4.2.4.1):

$$\gamma^g/\gamma_r = 1 + \frac{3c^3}{2\omega^3}\int_0^\infty k^2 dk \,\mathrm{Im}\left\{\frac{-1}{\varepsilon + 1 + 4\pi i k\sigma/\omega}\right\} e^{-2kz}, \qquad \text{Eq. 4.29}$$

where z is the distance between emitter and graphene, ε is the dielectric constant of the substrate and c the speed of light.

With an optical conductivity $\sigma = 1.2+0.8i$ (average value at 535 nm, see Figure 4.9 a), the dielectric constant of mica $\varepsilon_{mica} = 2.6$ (ref. [115]) at 535 nm and a distance between R6G and graphene of $z = 0.5$ nm (center-to-center distance of graphene and R6G, estimated from the SFM images of R6G confined by graphene and the thickness of graphene, see chapter 4.2.3.2), a normalized total decay rate γ^g/γ_r of $2.9\text{x}10^5$ is calculated. Assuming no any local excitation enhancement this value is identical to the inverse of the normalized fluorescence rate γ_{em}^{norm} and thus yields a normalized fluorescence rate of $3.5\text{x}10^{-6}$. Also usage of the equations for the non-radiative decay rate based on the theoretically calculated dielectric properties of graphene (TBM [142] and TBM based RPA [143], no plasmon activity in the visible) results in normalized fluorescence rates close to the ones calculated above from the

measured dielectric properties with the equation published in ref. [34]. Note, that the calculated normalized fluorescence rates are between two and three orders of magnitude smaller than the measured one. Possible charge transfer quenching, which is not taken into account by the equations above, results only in a further decrease of the calculated normalized fluorescence rate and can thus only increase the discrepancy between calculated and measured normalized fluorescence rates.

However, so far excitation enhancement provided by graphene plasmons was not taken into account. Similar to plasmons at metal surfaces the graphene plasmon contribution to the total decay rate of the emitter is estimated from the pole contribution of the local reflected field.[80,144] In particular the graphene plasmon contribution to the normalized decay rate in the graphene region γ^{sp}/γ_r can be calculated from the graphene plasmon wavelength λ_{sp}, which is related to the optical conductivity of graphene (see Figure 4.9a) at the emission frequency ω of the emitter [34]:

$$\gamma^{sp}/\gamma_r \approx \frac{12\pi^4 c^3}{(\varepsilon+1)\omega^3}\frac{e^{-4\pi z/\lambda_{sp}}}{{\lambda_{sp}}^3}, \qquad \text{Eq. 4.30}$$

where z is the distance between emitter and graphene, ε is the dielectric constant of the substrate and c the speed of light. Substitution of an optical conductivity σ = 1.2+0.8i at 535 nm and the dielectric constant of mica (see Figure 4.9a) into Eq. 4.12 gives a plasmon wavelength λ_{sp} of 9 nm. The imaginary part of the plasmon wavevector reflects the in-plane propagation distance [34] l_{sp} (here equal to 6 nm) and indicates that the plasmon is damped in the visible spectral range due to generation of electron-hole pairs, but is still capable of field enhancement which will be shown in the following.

By substituting the graphene plasmon wavelength and the same values as above into Eq. 4.30 the plasmon contribution to the normalized decay rate of the emitter γ^{sp}/γ_r is calculated to $1.4\text{x}10^5$, which is on the same order as the normalized total decay rate (see above). Thus, the plasmon-related decay is a major contribution to the total decay. This is changing at emitter graphene distances on the order of the graphene

plasmon wavelength, at which the emitter can not support the large wavevectors needed to excite plasmon anymore and thus also direct excitation of electron-hole pairs becomes significant (see Figure 4.18 and discussion below).[34]

Excitation enhancement is caused by excited graphene plasmons that subsequently re-excite, not necessarily coherent, the emitters (self-reaction or secondary field) [59]. As a result in the graphene regions an increase of the normalized fluorescence rate is observed. The excitation enhancement ($\gamma_{ex}^{g}/\gamma_{ex}^{s}$) scales with the square of the enhancement of the electric field at the position of the emitter [59] (as excitation of graphene plasmons by free space photons is negligible). Since the field enhancement results from the field confinement of the photon field with a wavelength λ_0 to the field of the graphene plasmons with a wavelength λ_{sp},, the magnitude of the excitation enhancement at the origin of the plasmon can be estimated from the reduction of the mode volume given by [34] $(\lambda_0/\lambda_{sp})^2$ yielding a correspondent increase of the energy density [145] (equal to the square of the field enhancement). The electric field normal to graphene exponentially decays as $\exp(-z\ \mathrm{Re}(k_{sp}))$ and in the plane of graphene as $\exp(-x\ \mathrm{Im}(k_{sp}))$ due to damping of the plasmon away from the point of its excitation by generation of electron-hole pairs in graphene.[34] Assuming that the extension of the plasmon is large compared to that of the absorption dipole of the emitter, which is justified here, the excitation enhancement by plasmon-mediated re-excitation of R6G in the graphene covered areas relative to the uncovered mica areas can be written as:

$$\gamma_{ex}^{g}/\gamma_{ex}^{s} = 1 + g_{sp\to em} g_{em\to sp} \frac{\lambda_0^{\,2}}{\lambda_{sp}^{\,2}} e^{-4\pi z/\lambda_{sp}} . \qquad \text{Eq. 4.31}$$

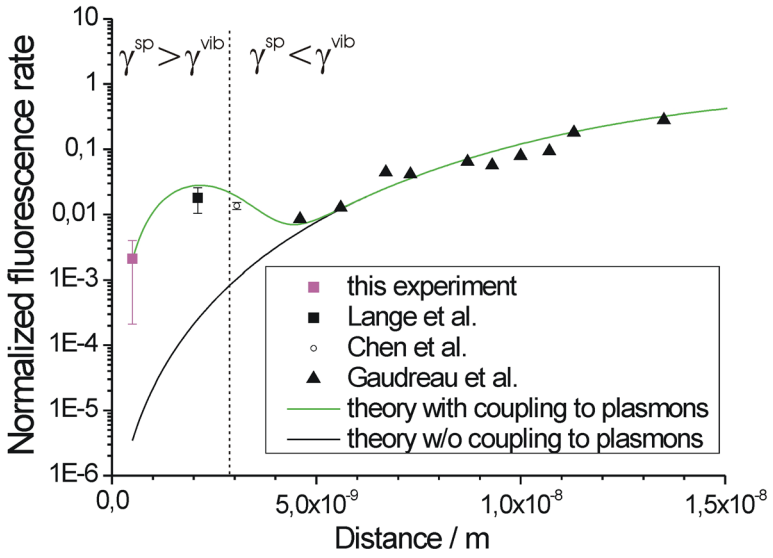

Figure 4.18. Distance dependent normalized fluorescence rate with (green curve) and without (black curve) excitation enhancement. A striking deviation of the experimental data to the theory without plasmon excitation at distances smaller than the graphene plasmon wavelength is evident. The pink square is the normalized fluorescence rate measured in this experiment. Black square, circle and triangles are normalized fluorescence rates obtained from the measured quenching factors and rates adopted from ref. [123] (Lange et al.)), ref [70] (Chen et al.) and ref. [71] (Gaudreau et al.), respectively. Note that the curves are calculated for the experimental parameters given in this publication. The experimental parameters (emission wavelength, substrate refractive index) in ref. [123], ref. [70] and ref [71] differ somewhat, the resulting deviations in the calculations are, however, insignificant for the comparison to theory with and without plasmon. Ratios of excited state relaxation rate to radiative rate, necessary for calculation of the excitation enhancement (Eq. 4.31), are also comparable to R6G (see ref. [70,138,146-149]).

Similar as in ref. [144] first the coupling efficiency of the emitters to graphene surface plasmons $g_{em\to sp} = \gamma^{sp} / \left(\gamma^{sp} + \gamma^{g}\right)$ is introduced as additional correction to include reduction of the coupling efficiency to graphene plasmons through direct excitation of electron-hole pairs in graphene. Second, with the coupling efficiency of graphene plasmons to the emitters $g_{sp\to em} = \gamma^{sp} / \left(\gamma^{sp} + \gamma^{vib}\right)$, it is included that efficient re-excitation is only possible if the decay rate into graphene plasmon γ^{sp} (here $3.1\text{x}10^{13}$ s^{-1}, see above) is larger than the vibrational relaxation rate γ^{vib} of the emitter [59] ($\approx 10^{12}$ s^{-1} for R6G) [149]. The latter is equivalent with a negligible spectral red shift between the energy of the graphene plasmon and the absorption of the emitter, i.e. a negligible spectral mismatch (indicated by the dashed vertical line in Figure 4.18). Furthermore a damping induced spectral broadening of the graphene plasmon which can also result in a reduced spectral overlap of graphene plasmon and emitter is considered in the following.

The plasmon linewidth Γ is related to the plasmon group velocity v_{sp} (in graphene equal to the Fermi velocity 10^6 m/s) [150] and its propagation distance l_{sp} (6 nm, see above) by $\Gamma = (\hbar v_{sp})/l_{sp}$ (ref. [80]) and can thus be estimated to 0.1 eV. Note that the plasmon group velocity can not be estimated from the slope of the plasmon dispersion (see Figure 4.9a). in the anomalous dispersion region (which is given here) due to wave profile deformation. Instead it coincides with to the plasmon group velocity in the normal dispersion region as used above.[151] A further estimation can be conducted by considering broadening of the graphene plasmon linewidth through dephasing [152] (damping) of the collective oscillation of electrons. Taking the lower limit of the nonequilibrium (quasi free) carrier relaxation time in graphene (0.01 ps) [153] as an estimate for the graphene plasmon dephasing time τ_{sp}, one can estimate an upper limit of the graphene plasmon linewidth $\hbar/\tau_{sp}$ of even less than 0.1 eV. Since these value are on the same order as the full width half maximum of the R6G absorption [118] reduced spectral overlap through spectral broadening of the graphene plasmon can be neglected in this calculations. Note that structural defects in epitaxial graphene can lead to larger graphene plasmon linewidths,[150] these defects are, however, unreasonable for the exfoliated graphenes used here.

Using the values for z, λ_{sp} and λ_0 given above yields a relative excitation enhancement $\gamma_{ex}^{g} / \gamma_{ex}^{s}$ in the graphene covered sample regions on the order of 600, nearly 3 orders of magnitude. Substitution into Eq. 4.28 yields a normalized fluorescence rate on the order of $2\text{x}10^{-3}$, which is in the same range as the measured normalized fluorescence rate in contrast to the underestimation by orders of magnitude when neglecting possible re-excitation due to plasmons.

Figure 4.18 contains the key result and displays the normalized fluorescence rate for emitters as a function of the distance to graphene (green curve with and black curve without plasmon induced excitation enhancement). The graph implies that the difference between including and excluding excitation enhancement is only pronounced at distances smaller than the graphene plasmon wavelength at which efficient graphene plasmon excitation and strong field enhancement is present, similarly as demonstrated for plasmons at metal surfaces [141,154]. The calculated normalized fluorescence rate is also in very good agreement with fluorescence rates

of emitters in proximity to graphene measured at larger distances by the author himself (see chapter 4.1.3.2 or ref. [123], fluorescent polymer film with a typical quantum yield of 0.03±0.01 [148]) and by others [70,71].

Quenching by multilayer graphene can be calculated by treating every layer of graphene in a multilayer graphene sample as an individual decay channel (superposition) with the individual layers separated by 0.34 nm as suggested in ref.[70]. Including in this case also the excitation enhancement induced by each layer the normalized emission rate for R6G confined by a 6-layer graphene can be obtained by summing up the total decay rate normalized by the excitation enhancement of each layer which gives a normalized emission rate of 1.2×10^{-3}. This value is 1.7 times smaller than the normalized emission rate estimated for single layer graphene, which agrees well with the ratio of the experimental quenching factors for single and 6-layer graphene samples, respectively (see chapter 4.2.4.3). Thus this data also indicate emitter-plasmon coupling for multilayer graphene. Similarly as for single layer graphene one would expect a decrease of the normalized fluorescence rate by orders of magnitude when coupling to plasmons is neglected (see above). Note, that plasmon activity of few and multilayer graphenes is also indicated by EELS.[33,117]

4.2.6 Conclusions

In conclusion, it was shown that graphene supports strongly localized plasmons in the visible with a line width of 0.1 eV and capable of excitation enhancement by nearly 3 orders of magnitude. Its existence is implied by the optical conductivity of graphene and also direct evidence by quantifying the quenching efficiency of graphene was given. These results agree well with EELS experiments and DFT predictions. Plasmonic activity in the visible introduces graphene not only as an exciting material for plasmonic devices for technological application at optical frequencies, but also its understanding is mandatory for the interpretation of graphene based optical experiments (e.g. graphene induced Raman enhancement, see next chapter). The extraordinarily strong confinement of graphene plasmons, implied by their short wavelength and short propagation distance and thus the outstanding emitter-plasmon coupling strength, despite strong intrinsic plasmon damping, suggests graphene as a candidate for highly integrated nano-optoelectronic devices.

Future experiments should address graphene plasmon tuning in the visible spectral range

4.3 Graphene induced Raman enhancement

4.3.1 Introduction

Raman spectroscopy is a powerful tool for material analysis and identification. However, Raman scattering cross sections of molecules and consequently the detected Raman intensities are typically low, which limits the applicability of Raman spectroscopy, especially for low analyte concentrations. Thus, in the last decades extensive research has addressed the development of techniques and substrates, which increase the detection sensitivity in Raman spectroscopy. These include decrease of the often present but undesired fluorescence, scattering and reflection background and increase the Raman intensity of the analyte. The use of fluorescence quencher [155] and stimulated Raman spectroscopy [156] have been demonstrated to strongly reduce the fluorescence background and consequently increase the signal to noise ratio in Raman spectroscopy. Furthermore plasmon active substrates have been demonstrated to enhance Raman scattered intensities by orders of magnitude referred to as Surface Enhanced Raman Spectroscopy (SERS).[52]

Graphene can be considered as a promising substrate for Raman spectroscopy, as it exhibits strong fluorescence quenching [70,123,157], low reflectivity [2] and additionally large scale graphene production has been demonstrated [8,9]. Graphene was also shown to protect conjugated molecules from photodegradation (see chapter 4.1.3.2), which allows the use of high Raman excitation power to further increase signal output. Yet, Raman enhancement by graphene, both its magnitude and the acting mechanism, is still under debate in literature [35,36,158-162]. The Raman intensity of phthalocyanine molecules on graphene was demonstrated to be enhanced by more than one order of magnitude relative to their Raman intensity on the supporting substrate.[35] However, the Raman cross section of rhodamine 6G molecules on graphene was shown to be even smaller than its Raman cross section in solution.[36] Thus an enhancement of Raman cross sections of any molecules through graphene relative to their value in solution, the key for Raman spectroscopy on low analyte concentrations, has not been demonstrated yet.

The author would like to point out that the use of the detectability of Raman peaks from fluorescent molecules on graphene as an evidence for Raman enhancement by

graphene [161] is unfounded, since strong fluorescence quenching has been demonstrated to increase the signal to noise ratio in Raman spectroscopy [155]. Unsuitable references and unknown molecule surface density can indeed result in overestimation of Raman enhancements by orders of magnitude.[52]

Raman enhancement induced by graphene has been argued to result from a charge transfer (CT) between graphene and the adsorbed molecules,[35,160,162] since the enhancement occurred for very small graphene to molecule distances only, prerequisite for a transfer of charges [160] and since the enhancement was found to be tunable through a shift of the Fermi level of graphene [158,162]. However, the excitation of a charge transfer resonance with the photon (laser) energy being almost two times larger than the energy gap of the CT requires a very strongly broadened CT resonance,[162] which on the author's opinion makes a CT resonance Raman enhancement mechanism at least questionable. Furthermore, a strong dependence of the Raman enhancement on the Fermi level shift of graphene is expected from a CT resonance enhancement mechanisms, but in experiments a weak dependency is found, Therefore a CT resonance as major source for graphene induced Raman enhancement is unreasonable.[158]

The assignment of graphene induced Raman enhancement to a CT mechanisms was also motivated by the assumption that graphene is plasmon inactive in the visible spectral range [35] (as it was predicted by tight binding model based random phase approximation, see e.g. ref. [34]). However, graphene has been shown to be plasmon active at visible frequencies by electron energy loss spectroscopy (EELS) [32,33]. Furthermore graphene plasmons were shown to increase the excitation rate of fluorescent molecules in proximity to graphene (see chapter 4.2.5). This indicates that graphene plasmons must be considered as a possible Raman enhancement mechanism.

Here Raman measurements rhodamine 6G (R6G) on solid substrate and covered by single and multilayer graphenes are presented. The Raman cross section of resonantly excited R6G is estimated by two independent methods: the first method is based on the R6G surface density and the Raman cross section of graphene as the reference cross section, consideration of the orientation of the molecules confined by

graphene is also taken into account; the second method, which is independent of the R6G surface density, is based on the measured fluorescence cross section of R6G covered by graphene as reference. Raman enhancement is estimated as the ratio of the Raman cross sections of R6G covered by graphene to its value in solution. The results are compared to Raman enhancement expected from increase of the molecule's induced dipole through interaction with graphene plasmons in the visible spectral range (see Figure 4.19).

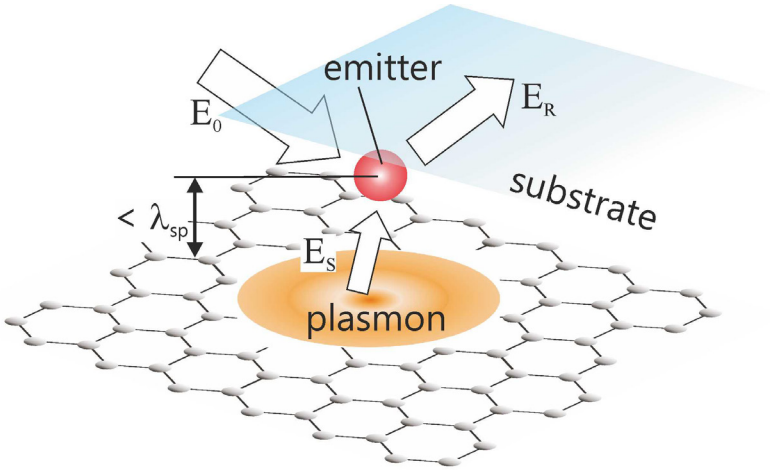

Figure 4.19. Diagram of the experiment including proposed Raman enhancement meachanism: graphenes were exfoliated onto a mica substrate covered with a submonolayer of R6G molecules. Raman scattering was excited with a laser incident through the substrate (E_0). Efficient excitation of graphene plasmons by the far-field (E_0) is not possible due to the large mismatch with the wavevector of graphene plasmons (see chapter 4.2.2). However, the nearfield of the scattering dipole of the emitter provides wavevectors suitable for efficient graphene plasmon excitation. The field of the graphene plasmon (E_S) enhances the amplitude of the induced Raman dipole and subsequently scattering of incident radiation (E_R) [52].

4.3.2 Spectrally resolved emission of R6G confined by graphenes

Figure 4.20a shows a Raman spectrum of R6G covered with single layer graphene including R6G fluorescence background (blue curve). A fluorescence background subtracted spectrum (black curve) is obtained by conforming the R6G fluorescence recorded in sample regions not covered by graphene (red curve) to the blue curve followed by its subtraction (see also discussion below). The spectrum in the graphene region exhibits typical R6G Raman peaks, with the R6G Raman peak ratios being remarkably similar to the peak ratios recorded in solution using stimulated Raman spectroscopy [156].

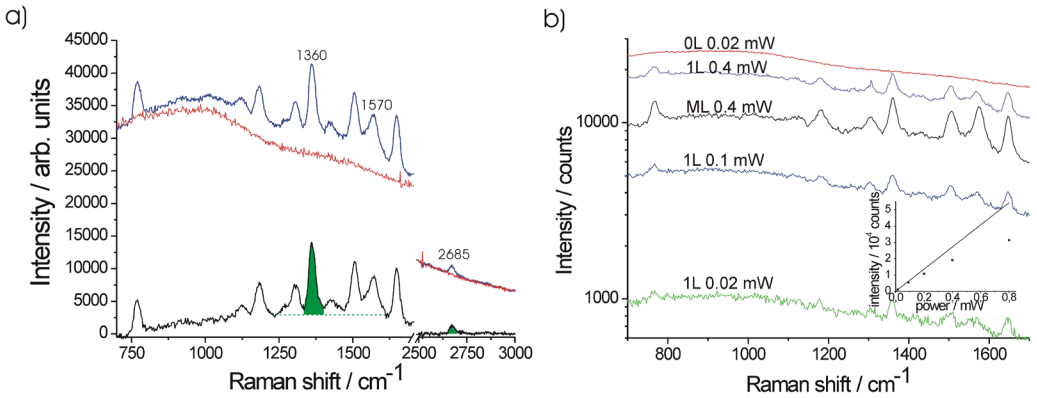

Figure 4.20. a) Raman spectra of R6G on mica (prepared from 0.1 mM) covered with single layer graphene including R6G fluorescence background (blue curve) and with fluorescence background subtracted (black curve) at 0.8 mW excitation power. To obtain the background subtracted spectrum the fluorescence recorded in uncovered sample regions is conformed (red curve) to the fluorescence background in the graphene covered regions. Note, that the red curve does not perfectly fit the fluorescence background in the graphene covered sample regions in the entire spectral range. Thus the green shaded peaks areas used for quantification of the R6G Raman cross section are obtained by assuming the minima between well separable Raman peaks as the base line (green dashed line) b) Raman spectra and fluorescence background recorded in single layer graphene (1L; green, blue and violet curve), multilayer graphene (ML; roughly 10 layers; black curve) and mica regions (0L; red curve), at different excitation powers. The inset shows the excitation power dependence of the detected peak fluorescence intensity of R6G covered by single layer graphene (black squares). The back curve in the inset indicates the peak fluorescence expected from a linear extrapolation of the detected peak fluorescence recorded at the lowest excitation power. All spectra were excited at 532 nm.

Furthermore the graphene 2D Raman peak around 2685 cm^{-1} is detectable. The peak around 1570 cm^{-1} can be attributed to an overlap of the graphene G peak and the R6G Raman peak in the same spectral region (see also below). The R6G Raman peaks are also detectable in spectra recorded within multilayer graphene regions (Figure 4.20b black curve) with the R6G peak heights and ratios being similar to the single layer graphene regions. Yet the peak around 1575 cm^{-1} (overlap of R6G and graphene peak, see also above) has increased due to the larger Raman cross section of the multilayer graphene G peak relative to the single layer graphene G peak (see e.g. ref. [163]).

Spectra recorded in the mica regions not covered by graphene, in contrast, do not exhibit any detectable Raman peaks but fluorescence background only (Figure 4.20a and b). The fluorescence intensity in regions covered by graphene is about 25 times weaker than in uncovered regions (Figure 4.20b red and green curve), which can be attributed to strong fluorescence quenching by graphene (see chapter 4.2.4.3 and below). Thus in agreement with previous investigations fluorescence background

reduction through quenching has contributed to the increased detectability of the R6G Raman peaks in the graphene regions [37].

Note that measured fluorescence quenching by graphene for excitation of R6G at around 546 nm (here at 532 nm) was determined in chapter 4.2.4.3 to 5.2±0.7 and that including equal excitation and emission detection conditions of the R6G fluorescence in the mica and graphene regions an effective quenching factor between 16 and 181 was obtained (see chapter 4.2.4.5).

The higher quenching factor measured here (about 25 at 532 nm excitation) compared to chapter 4.2.4.3 (5.2 ± 0.7 at around 546 nm excitation) can be attributed to a more efficient excitation of R6G in the mica region in this case resulting from the absorption maximum of R6G on mica (see chapter 4.2.3.1) being closer to the laser wavelength (532 nm) used for excitation. Still it can be regarded as a lower limit, due to possible bleaching of the R6G fluorescence in the mica regions. The excitation powers used in chapter 4.2.4.3 were chosen to be much lower than here (4 orders of magnitude below the lowest excitation power used here) in order to exclude significant impact of bleaching on the measured quenching factor.

Including the higher fluorescence excitation and emission collection efficiencies of R6G in the graphene regions due to its flat orientation, accounting roughly for a factor of 2 and 3, respectively (see chapters 4.2.4.4 and 4.2.4.5), an effective quenching factor on the order of 100 can be estimated here in aggreement with the measurements in chapter 4.2.4.3 and the effective quenching factor derived from them in chapter 4.2.4.5. Also in agreement with chapter 4.2.4.3 is that multilayer graphene exhibits stronger fluorescence quenching than single layer graphene (here about 40% stronger).

Also note, that the contribution of R6G Raman scattering to the total measured emission signal (Raman and fluorescence) in the graphene region is very small (about 0.004, see chapter 4.3.3.2) and does not change the estimated quenching factor in chapter 4.2.4.3.

During the Raman measurements in the graphene regions fluorescence background reduction by photodegradation is present at high excitation powers, but low compared to fluorescence quenching (see above) and thus only a minor contribution to the background reduction increased detectability of the R6G Raman peaks (Figure 4.20b).

4.3.3 Estimation of the R6G Raman cross section from a reference

In order to quantify possible Raman enhancement, the Raman cross section of R6G covered by graphene is estimated in the following by two independent methods.

4.3.3.1 Estimation of the Raman cross section of R6G from the Raman cross section of graphene

This method is based on the Raman cross section of the R6G layer estimated from the Raman cross section of graphene and the R6G surface density.

Estimation of the Raman cross section of the R6G layer

First the Raman cross section of the R6G submonolayer is estimated using the Raman cross section of the graphene as a reference. The Raman cross section of a single R6G molecule is obtained by determination of the R6G surface density (see below). This approach was up to the author's knowledge introduced by Kangan and McCreery to estimate the Raman cross section of molecules adsorbed on glassy carbon [164] and employed in ref. [36] to estimate the Raman cross section of R6G on graphene. The approach used in ref. [36] is expanded here, by deriving the Raman cross section of graphene directly from its Raman tensor [165] and estimating the R6G surface density including consideration of the R6G orientation.

R6G (here R6G peak around 1360 cm^{-1} used for comparison) and graphene 2D Raman cross sections $\sigma_R(\omega_2)$ and, respectively, $\sigma_R(\omega_{2D})$ are related by the ratio of their integrated peak intensities $P_R(\omega_2)$ and, respectively, $P_R(\omega_{2D})$ (green shaded areas in Figure 4.20a) :

$$\sigma_R(\omega_2) = \frac{\langle P_R(\omega_2)\rangle}{\langle P_R(\omega_{2D})\rangle}\sigma_R(\omega_{2D}). \qquad \text{Eq. 4.32}$$

Since the Raman cross section of the graphene 2D peak $\sigma_R(\omega_{2D})$ is not directly availabe in literature, it is derived from the known differential Raman cross section of graphite $\sigma_R(\omega_{graphite})$ and the known ratio of graphene and graphite cross sections. In particular it can be related to the Raman cross section of the 2D graphene peak $\sigma_R(\omega_{2D})$ by the ratio of the graphene G and 2D peak $P_R(\omega_{2D})/P_R(\omega_G)$ and the ratio of the graphene G and graphite peak $P_R(\omega_G)/P_R(\omega_{graphite})$:

$$\sigma_R(\omega_{2D}) = \frac{\langle P_R(\omega_{2D})\rangle}{\langle P_R(\omega_G)\rangle} \frac{\langle P_R(\omega_G)\rangle}{\langle P_R(\omega_{graphite})\rangle} \sigma_R(\omega_{Graphite}). \qquad \text{Eq. 4.33}$$

With $P_R(\omega_2)/P_R(\omega_{2D}) = 8.2 \pm 2.9$ (see Figure 4.20a), $P_R(\omega_{2D})/P_R(\omega_G) \approx 3$ (for graphene on mica, see Figure 4.21), $P_R(\omega_G)/P_R(\omega_{graphite}) = 0.49$ (ratio of the squared Raman tensor components of graphene and graphite given in ref. [165]) and $\sigma_R(\omega_{graphite})$ between $3.3 \times 10^{-11}\,sr^{-1}$ and $5.4 \times 10^{-11}\,sr^{-1}$ [164,166], this yields a differential Raman cross section of the R6G layer between $2.6 \times 10^{-10}\,sr^{-1}$ and $8.9 \times 10^{-10}\,sr^{-1}$. Note, that $P_R(\omega_{2D})/P_R(\omega_G)$ is not expected to be smaller than 3 even in the case of a possible strong Fermi energy shift [167].

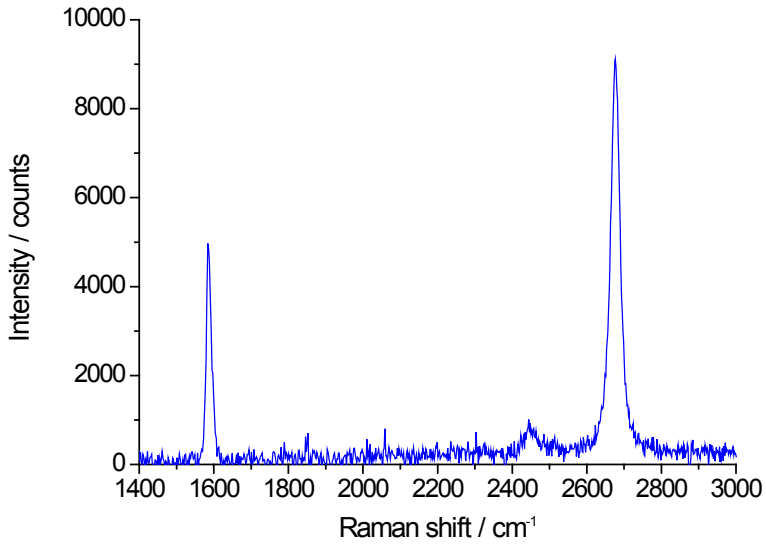

Figure 4.21. Raman spectrum of single layer graphene on mica substrate recorded at 45% RH, excitation at 532 nm. The integrated Raman intensity of the 2D and G peak yields a ratio of about 3.

Furthermore, in the estimation above the Raman cross section of graphite and the Raman tensor component of graphene measured at 514.5 nm excitation [164-166] is assumed for the 532 nm excitation used here. This is reasonable, since graphene and

graphite do not exhibit strong dispersion of their absorption in this spectral range [45,58] and therefore no strong variation (resulting from a more or less resonant excitation) of their Raman scattering cross sections is expected. To obtain the Raman cross section of a single R6G, the R6G surface density will be estimated in the following from a contrast measurement.

Estimation of the R6G surface density from contrast spectroscopy

The surface density of R6G confined by graphenes was already estimated from absorption spectroscopy (chapter 4.2.3.1) and SFM (chapter 4.2.3.2), however, with rather low accuracy. In this chapter a further approach exhibiting higher accuracy will be presented.

Figure 4.22a displays a contrast micrograph of graphene exfoliated on R6G covered mica substrate. Graphenes appear dark on the mica background (single layer graphene and mica regions are marked as I and X, respectively). Figure 4.22b displays the wavelength dependent contrast of single layer graphenes on the R6G covered mica substrate (blue squares), with the contrast C being defined by the intensities in mica (I_X) and graphene regions (I_I): $C = (I_X - I_I)/I_X$. The dashed black line indicates the contrast expected from the lower limit of graphene's absorption in the visible (see below).

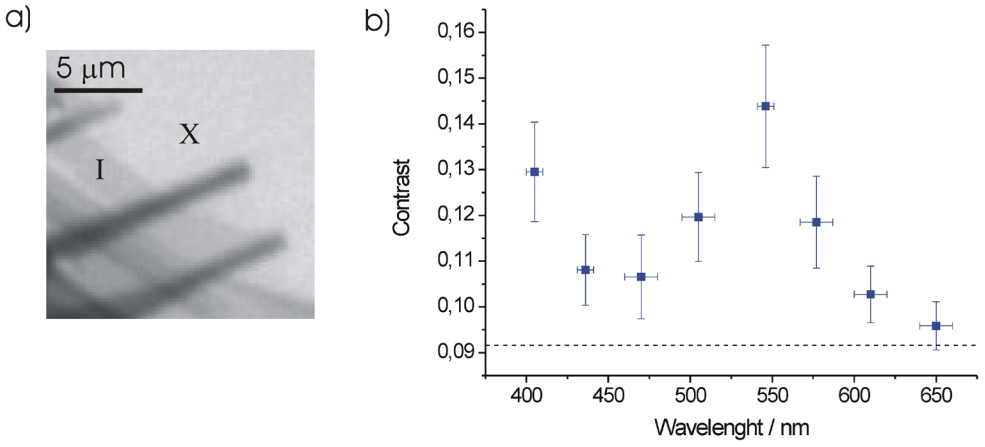

Figure 4.22. a) Contrast micrograph of graphene on R6G covered mica substrate. Graphenes appear dark on the mica background. Single layer graphene (brightest of the darker areas) and mica regions are marked as I and X, respectively. b) Wavelength dependent contrast of single layer graphenes on R6G covered mica (prepared from 0.1 mM). The errors in direction of the wavelength axis correspond to the half width of the used bandpass filters. Dashed black line indicates the contrast expected from the lower limit of graphene's absorption.

The measured contrast (Figure 4.22b) around 650 nm and 405 nm, at which no strong absorption of R6G is expected [118], corresponds roughly to the contrast of single layer graphene on mica [88]. The higher contrast around 405 nm agrees with the increased absorption in this wavelength range (contrast is proportional to absorption, see below) observed for freely suspended graphene [2,46] and graphene on other substrates [45,58]. However, the contrast peak around 546 nm is attributed to result from R6G absorption. Absorption features such narrow that they fit in the spectral regions not covered by the used bandpass filters (515 nm to 541 nm and 551 nm to 567 nm) are not expected for R6G [118]. This is supported by the similar contrast values around 505 nm and 577 nm, indicating the contrast peak to be centered between these wavelength values. Thus it can be concluded that the absorption peak of R6G in the graphene region is located between 541 nm and 551 nm (width of the bandpass filter). This corresponds to a red shift of the R6G absorption peak in the graphene region compared to the mica region (see chapter 4.2.3.1) (and to solution, see ref. [118]) by at least about 11 nm, which is attributed to interaction of R6G with the substrate (see e.g. [168,169]).

The intensity of the contrast peak allows to estimate the surface density of R6G in the single layer graphene region (similarly to the identification of the number of graphene layers on a mica substrate from the optical contrast, see ref. [88]), by fitting the measured peak contrast C_{max} with

$$C_{\max} = \frac{r_N^2 - r_{N'+g}^2}{r_N^2} \quad , \qquad \text{Eq. 4.34}$$

with r_N being the reflection coefficient for the regions not covered by graphene and $r_{N'+g}$ the reflection coefficient for the regions covered by graphene (corresponding to the reflected field amplitudes in the respective regions). These reflection coefficients will be derived in the following.

The reflection coefficient of an arbitrary interface r_{ij} at normal incidence is given by [96]:

$$r_{ij} = \frac{n_i - n_j}{n_i + n_j}, \qquad \text{Eq. 4.35}$$

with the refraction n_i and n_j of the media forming the interface. In the thin film approximation (valid for film thicknesses much smaller than the optical wavelength) the reflection from an interface with a surface conductivity G can be written as [89]:

$$r_{ij}' = \frac{n_i - n_j - 4\pi G/c}{n_i + n_j + 4\pi G/c}. \qquad \text{Eq. 4.36}$$

For graphene the real part of $4\pi G/c$ is approximately equal to $\pi\alpha$, with α being the fine structure constant (see also below). The dynamic conductivity G of a thin film can also be related to its transmittance T [2,27]:

$$T = \left(1 + 2\pi G/c\right)^{-2} \approx 1 - 4\pi G/c \cong 1 - A. \qquad \text{Eq. 4.37}$$

As a thin film (like graphene or thin molecular layers) does practically not reflect light, its absorbance A is equal to $4\pi G/c$ [2,170]. One can thus write:

$$r_{ij}' = \frac{n_i - n_j - A}{n_i + n_j + A}. \qquad \text{Eq. 4.38}$$

With the relation of the surface density of a molecule layer N/S and the absorption cross section σ_{abs} to the absorbance A, the reflection coefficient from an interface covered with a thin molecule layer can be written as:

$$r_N = \frac{n_i - n_j - \frac{N}{S}\sigma_{abs}}{n_i + n_j + \frac{N}{S}\sigma_{abs}} \qquad \text{Eq. 4.39}$$

and the reflection coefficient from an interface covered with both graphene and a thin molecule film with a surface density N'/S and an absorption cross section σ'_{abs} as:

$$r_{N'+g} = \frac{n_i - n_j - \pi\alpha - \frac{N'}{S}\sigma'_{abs}}{n_i + n_j + \pi\alpha + \frac{N'}{S}\sigma'_{abs}}. \qquad \text{Eq. 4.40}$$

Here n_i and n_j refer to the refractive indices of mica and air n_m and n_a, respectively. Accordingly N/S is the surface density and σ_{abs} the absorption cross section of R6G in the mica region and N'/S and σ'_{abs} in the graphene region. $\pi\alpha$ is the lower limit of the absorption of freely suspended graphene in the visible.[2] Since the absorption of graphene on a substrate could be slightly higher (see e.g. ref. [58]), the estimated surface density of the molecules N'/S in the graphene region is an upper limit.

The peak absorption cross section of R6G in the graphene covered region for the illumination aperture used in this experiment (NA = 0.55) can be estimated to $\sigma' = 6.8 \times 10^{-16}$ cm^2 by multiplication of the peak absorption cross section of (unordered) R6G in solution 4×10^{-16} cm^2 [118] with the geometrical correction factor 1.7 (see chapter 4.2.4.4). The correction factor accounts for the fact that the R6G molecules are approximately flatly confined by graphene and not unordered as in solution (see chapter 4.2.3.2), resulting in an effectively higher absorption cross section. The absorption cross section of uncovered R6G on mica and of R6G in solution at 546 nm can be estimated to be approximately one third of the peak absorption cross section in solution: $\sigma = 1.3 \times 10^{-16}$ cm^2. Molecules in the uncovered mica region are rather unordered as in solution and exhibit an absorption spectrum similar as in solution (see chapter 4.2.3.1). With $n_a = 1$ and $n_m = 1.596$ [88,171] and further assuming the surface density in the mica and graphene regions to be identical ($N = N'$), this yields a R6G surface density of $2.5 \pm 1.1 \times 10^{13}$ cm^{-2}.

Assuming the R6G surface density in the regions not covered by graphene being smaller than in the graphene covered regions does not strongly alter the calculated surface density in the graphene covered regions. This can be attributed to the effectively higher absorption cross section of R6G covered by graphene compared to

R6G on mica around 546 nm, resulting from the peak shift and the flat orientation (see above). Thus the above estimation of the R6G surface density is reasonably.

In order to obtain the total Raman cross section of the 1360 cm^{-1} peak of a single R6G molecule, the differential cross section of the 1360 cm^{-1} peak of the R6G layer needs to be divided by the R6G surface density ($2.5 \pm 1.1 \times 10^{13}$ cm^{-2}, see above) and multiplied by the whole solid angle 4π. Multiplication by 4π is equivalent to the integration over the whole solid angle under the assumption that R6G with the transition dipole oriented parallel to graphene exhibits in the used experimental configuration the same radiation pattern as graphene (same angular distribution of radiated power). This yields a total Raman cross section of R6G covered by single layer graphene between 0.9×10^{-22} cm^2 and 8×10^{-22} cm^2. The ratio of the estimated total R6G Raman cross section to the total R6G Raman cross section in solution ($2.6 \pm 0.3 \times 10^{-23}$ cm^2 with 532 nm excitation, see ref. [156]) yields a Raman enhancement between 3 and 35. The estimated Raman enhancement exhibits a large spread since a number of quantities is necessary for its estimation.

A Raman enhancement resulting from a substrate induced shift of the molecule resonance towards the laser wavelength used to excite Raman spectra can be excluded, since the resonantly excited Raman in solution [156] was used for comparison and since the peak absorption of R6G in the single layer graphene region is even slightly red shifted to its solution value and the wavelength of the laser used for excitation. Thus and because the estimated R6G surface density is an upper limit (see above) the R6G Raman cross section and correspondingly the Raman enhancement by graphene estimated here is a lower limit. Still the R6G Raman cross section estimated here is at least one order of magnitude higher than previously estimated by a similar approach [36]. This can be attributed to the more resonant excitation of R6G in this case (532 nm excitation) compared to ref. [36] (514.5 nm excitation).

To support the above conclusion the Raman cross section of R6G covered by graphene will be estimated in the next chapter by a further approach using the R6G fluorescence cross section as a reference (this approach does not require the R6G surface density).

4.3.3.2 Estimation of the Raman cross section of R6G from the R6G fluorescence cross section

In the following a second approach for the estimation of the R6G Raman cross section using the R6G fluorescence cross section $\sigma_F(\omega_3)$ as a reference will be presented, which is independent of the R6G surface density.

The R6G fluorescence cross section $\sigma_F(\omega_3)$ is related to the R6G Raman cross section $\sigma_R(\omega_2)$ by the ratio $P_R(\omega_2)/P_F(\omega_3)$ of the integrated peak intensity of the fluorescence and Raman peaks:

$$\sigma_R(\omega_2) = \frac{\langle P_R(\omega_2)\rangle}{\langle P_F(\omega_3)\rangle}\sigma_F(\omega_3), \qquad \text{Eq. 4.41}$$

with

$$\sigma_F(\omega_3) = \phi_{mica}\,\frac{1}{Q_{graph}\;B}\,\sigma_A(\omega_1). \qquad \text{Eq. 4.42}$$

The R6G fluorescence cross section in the graphene covered region is related to the R6G absorption cross section in the graphene region $\sigma_A(\omega_1)$ through the fluorescence yield of R6G on mica ϕ_{mica} (between 0.057 and 0.067, see chapter 4.2.4.2) and the fluorescence quenching by graphene Q_{graph} (between 16 and 181 see chapter 4.2.4.5). The bleaching B in the graphene region is estimated here to be smaller than $B < 2$ (see Figure 4.20).

The peak absorption cross section of R6G in the graphene covered region at an illumination aperture of $NA = 0.55$ equals $\sigma_{A\,peak} = 6.8 \times 10^{-16}$ cm^2 (see last chapter). From the contrast spectroscopy measurement (see Figure 4.22) the absorption of R6G in the graphene region at 532 nm (used excitation laser) can be estimated to be approximately 50% of the peak absorption, which results into an R6G absorption cross section in the graphene region at 532 nm of $\sigma_A(\omega_1) = 3.4 \times 10^{-16}$ cm^2. The ratio of the integrated fluorescence and Raman peaks can be determined from the measured spectra (Figure 4.20) to $P_R(\omega_2)/P_F(\omega_3) = 0.004 \pm 0.001$ assuming that about 50% of the total fluorescence is located in the detected spectral range of the

Raman measurement ranging from about 550 nm to 650 nm. With Eq. 4.41 and Eq. 4.42 this yields a total R6G Raman cross section in the graphene region between 0.2 x 10^{-21} cm^2 and 7.1 x 10^{-21} cm^2, corresponding to a Raman enhancement between 7 and 309 (comparision to solution value, see last chapter).

As in chapter 4.3.3.1 a number of quantities is necessary for the estimation of the Raman cross section thus resulting in a large spread. Combing the upper and lower limits of Raman enhancement estimated in this chapter and in chapter 4.3.3.1 yields a Raman enhancement between 7 and 35. A decrease of the Raman cross section can be excluded.

The results on Raman enhancement by graphene are in agreement with that estimated previously from a comparison of the Raman emission of molecules on graphene to the Raman emission of the molecules on the supporting substrate [35]. Yet the estimation presented here is up to the author's knowledge the first demonstration of enhancement of the resonance Raman cross section of molecules through graphene relative to the value in solution.

4.3.4 Raman enhancement by graphene plasmons in the visible

In the following it will be demonstrated that Raman enhancement by graphene can be explained by the electromagnetic enhancement induced by graphene plasmons in the visible.

The Raman dipole of a molecule $\mu(\omega_R)$ induced by the total electric field E at the dipole's origin is given by [59]:

$$\mu(\omega_R) = \alpha(\omega_0, \omega_v) E, \qquad \text{Eq. 4.43}$$

with $\alpha(\omega_0, \omega_v)$ being the Raman polarizability of a specific vibrational mode with frequency ω_v. The frequency of the Stokes scattered light ω_R is related to the frequency of the incident light by $\omega_R = \omega_0 - \omega_v$. The total local electric field E is the sum of the incident field E_0 and the local field E_s scattered or reflected by the dipole's environment. The field E_s can result from scattering of the incident field E_0

as well as from reflection of the dipole's own field by the environment and arriving again at its origin (secondary field or self-reaction). Since the reflected field is linearly dependent on the incident field one can write $E = (1+f)E_0$, with f being the field enhancement factor. The reflected field can enhance the amplitude of the dipole to oscillate at the frequency ω_R, and thus enhance the scattering amplitude of the incident radiation.[52]

In the case of plasmon active surfaces E_s is associated with the field of locally excited plasmons.[59] Rough metal surfaces and metal particles allow direct excitation of plasmons by the incident field (farfield) and by the dipole's own field (nearfield). Therefore in the case of rough metal surfaces the total enhancement of the Raman scattered field is expected to scale with f^2 and consequently the Raman scattered intensity with f^4.[59]

Graphene plasmons in the visible exhibit a wavevector mismatch with free space photons of about 50. Thus graphene plasmons are expected to be excitable only indirectly by the high wavevectors existing in the nearfield of the scattering (radiating) dipole (see chapter 4.2.2). Therefore field enhancement induced by graphene plasmons is expected to scale only with f and consequently enhancement of the Raman intensity of molecules in proximity to graphene with f^2.

In order to estimate graphene plasmon induced Raman enhancement, the field enhancement provided by graphene plasmons in the visible will be calculated in the following including the coupling efficiency of the Raman dipole to graphene plasmon and the spectral response of the graphene plasmon.

By assuming the coupling efficiency of the field scattered by the Raman dipole to graphene plasmons being equal to the coupling efficiency of the field radiated by a point dipole to graphene plasmons a total excitation enhancement $(1+f)^2$ (square of the field enhancement) of 600 can be estimated (see chapter 4.2.5). The spectral response of the graphene plasmons with respect to the emission of the Raman dipole needs also to be taken into account: Graphene plasmons in the visible spectral range are damped through excitation of electron hole pairs, which results in a graphene plasmon line width Γ_{sp} of 0.1 eV (see chapter 4.2.5). The line widths of R6G Raman

peaks are much smaller, in particular the R6G Raman peak around 1360 cm^{-1} exhibits a width Γ_R of 0.005 eV [156]. As only the spectral response of the graphene plasmon within the spectral response of the Raman emission can enhance the amplitude of the Raman dipole and subsequently scattering of incident radiation, the total excitation enhancement needs to be corrected by Γ_R/Γ_{sp}. The graphene plasmon induced Raman enhancement γ_R (square of the field enhancement acting on the Raman dipole) can thus be written as:

$$\gamma_R = (1+f)^2 \frac{\Gamma_R}{\Gamma_{sp}}, \qquad \text{Eq. 4.44}$$

which yields a Raman enhancement on the order of 30. This is much less compared to Raman enhancement by rough metal structures [52] since direct far-field excitation of graphene plasmons is so far not possible.

The similarity of the R6G Raman peak intensities recorded in single and multilayer graphene regions (see Figure 4.20b) indicates in agreement with previous investigation (see chapter 4.2.5) multilayer graphene being also plasmon active.

The strong confinement of the plasmon to the plane of graphene (out of plane decay 9 nm, see chapter 4.2.5) limits significant graphene plasmon induced enhancement of the Raman emission of molecules to graphene-molecule-distances on the order of nanometers. Thus graphene plasmon induced Raman enhancement is in agreement with the observation that enhancement of the Raman intensity of molecules by graphene occurs only for small graphene-molecule-distances [160].

Graphene induced Raman enhancement based on the graphene plasmon is also supported by the recently demonstrated dependency of the Raman intensity of molecules in proximity to graphene on the Fermi level position of graphene, as follows: EELS provided evidence that an upshift of the Fermi level of graphene results in a decrease of the graphene plasmon wavevector.[172] The wavevector decrease is accompanied by weaker confinement of the graphene plasmon, i.e. by a lower graphene plasmon induced field enhancement (see chapter 4.2.5). Consequently lower enhancement of the Raman emission of molecules in proximity

to graphene is expected (see above). This expected tendency of the Fermi level shift dependence of graphene plasmon induced Raman enhancement is in agreement with recently demonstrated Fermi level shift dependent Raman intensities of molecules adsorbed on graphene [158,162]. Furthermore the graphene plasmon wavevector [172] as well as the Raman intensity of molecules on graphene [158,162] showed a weak dependency on the Fermi level shift of graphene, which further supports that graphene plasmons are responsible for graphene induced Raman enhancement. In contrast for a CT resonance based Raman enhancement mechanism a strong dependency of the Raman intensity on the Fermi level shift of graphene is expected.[158]

A further increase of Raman enhancement by graphene can be expected with the use of antenna systems designed for direct far-field excitation of graphene plasmons, e.g. metal nano structures and gratings fabricated from graphene (graphene nano ribbons), both successfully demonstrated to be suitable for graphene plasmon excitation in the infrared [30,31].

4.3.5 Conclusions

It was shown that graphene enhances the R6G Raman cross section by one order of magnitude and in agreement with previous investigations additionally strongly increases the signal to noise ratio by the reduction of R6G fluorescence background. Results on Raman enhancement by graphene can be explained by purely electromagnetic enhancement provided by graphene plasmons in the visible excited by the Raman scattering dipole. The design of antenna systems for additional direct farfield excitation of graphene plasmons in the visible makes graphene a promising candidate for the development of a powerful SERS substrate.

5 Summary and Outlook

To investigate whether graphene may protect organic devices from their ubiquitous degradation under ambient conditions the permeation barrier properties of graphene were quantified *in situ* on a semiconducting organic layer. For this graphenes were deposited by mechanical exfoliation onto thin fluorescent polymer (P3HT) films. Reflection microscopy combined with a Fresnel law based model was used to identify the graphenes. Fluorescence and scanning force microscopies were used to probe the degradation kinetics of the polymer protected from the ambient by graphenes. Defect free graphenes were found to efficiently protect the fluorescent polymer from its ubiquitous degradation by water and oxygen from the ambient atmosphere. The change of the polymer fluorescence over time was used to provide upper limits of the water vapour and oxygen transmission rates through defect free graphenes of 5×10^{-6} g m^{-2} day^{-1} and 6×10^{-3} cm^3 m^{-2} day^{-1}, respectively. However, in single layer graphene a growing number of individual permeable point defects was observed resulting from a photo-induced structural degradation of the graphene. In contrast few layer graphene was found to remain free of permeable defects. The quantum yield for defect formation in single layer graphene was determined to 10^{-19} permeable defects per photon incident onto the graphene. Assuming that the defects occur randomly in a single layer of graphene and that the defect formation is uncorrelated between the layers of a multilayer graphene, the probabilities for defect formation in graphenes used to cover an organic solar cell exposed to sunlight (~1 kW/m^2) for 10.000 hours were calculated: The probability for formation of at least one permeable defect in one square centimetre of double layer graphene is 10^{-2}. Much larger graphene barriers require a triple layer graphene, for which the probability for at least one defect is 10^{-6} even for a size of one square meter. This indicates that graphenes meet the technological requirements of barrier material even on a macroscopic scale. Future experiments should address if large scale fabricated graphene layers, successfully demonstrated to work as electrode in prototypical devices,[7,12,13] can simultaneously function as permeation barrier layer to reduce device degradation through the ambient. The defect density of the fabricated graphenes is expected be a critical parameter [173].

Besides graphene's potential application as combined electrode and barrier layer in organic devices, it is an interesting quasi two-dimensional system. The investigation of the interaction between light emitters and graphene allows to study the nano-optical properties of graphene, e.g. its quasiparticles. In particular it was shown here that the known optical properties of graphene imply it to support strongly confined plasmons in the visible spectral range with a wavelength of 9 nm and a spectral width of 0.1 eV. This expectation on the properties of graphene plasmons agrees with plasmon spectroscopy of graphene using electron energy loss spectroscopy (EELS) [32,33] and with predictions by density functional theory (DFT) [116]. However, graphene is predicted to be plasmon inactive in the visible by the tight binding model (TBM) and by the TBM based random phase approximation (RPA),[34] which can be attributed to simplifications used in the TBM and being unfounded for the visible spectral range.

While the strong confinement of graphene plasmons in the visible prevents the use of standard experimental configurations for their excitation, the large wavevectors in the nearfield of small emitters are expected to be suitable for their excitation.[34] To investigate the interaction of graphene plasmons with small emitters, graphenes were deposited onto submonolayers of R6G molecules. Absorption, contrast and scanning force microscopies were used to explore the surface density and orientation of the emitters (R6G). Steady state and time resolved fluorescence microscopies were used to determine the quenching efficiency of graphene. Including consideration of the orientation of the small emitters a normalized fluorescence rate of the emitters in subnanometer proximity to graphene between 3.2×10^{-4} and 4.1×10^{-3} was determined. Based on the expected properties of graphene plasmons in the visible (see above) a theoretical calculation of the fluorescence rate was provided that includes increased nonradiative decay and enhanced fluorescence excitation (nearly 1000 times) through graphene plasmons yielding in agreement with the experimental results a normalized fluorescence rate of 2×10^{-3}. In contrast the fluorescence rate of the emitters expected for plasmon inactive graphene (TBM [142] and TBM based RPA [143]), which thus does not provide excitation enhancement, was calculated to 3.5×10^{-6} and thus disagrees the results. Furthermore it was predicted here that graphene plasmons provide strong excitation enhancement even up to graphene emitter distances of a

few nanometers in agreement with data on fluorescence quenching collected here and by others [70,71].

Finally Raman spectra of R6G covered by graphenes were recorded. In agreement with previous investigations [37] it was found here that fluorescence quenching by graphene contributes to the increased detectability of the R6G Raman spectra in the graphene regions. The Raman cross section of graphene was quantified based on the R6G surface density and the Raman cross section of graphene as a reference. Relative to the R6G Raman cross section in solution Raman enhancement through graphene was determined to range between at least 7 and 35, which is up to the author's knowledge the first demonstration of graphene induced enhancement of the Raman cross section of molecules. Following recent literature [158] it was argued that Raman enhancement expected from a charge transfer resonance can not explain the results found here and found by others [158,162]. However, Raman enhancement expected from graphene plasmons in the visible was calculated here to provide a 30 times enhancement, due to the narrow width of the R6G Raman emission relative to the spectral width of the graphene plasmon a lower enhancement than in the case of fluorescence (see above). The calculated Raman enhancement is in good agreement with the results.

The strong confinement of graphene plasmon in the visible makes graphene a promising candidate for highly integrated nano-optoelectronic devices. Future experiments should address switching of graphene plasmons in the visible spectral range by tuning graphene's optical conductivity and using electrically driven plasmon excitation [174] in graphene. Furthermore the use of antenna systems designed for efficient farfield excitation of graphene plasmons may allow a plasmon based light collection efficiency enhancement of devices and the development of an efficient graphene plasmon based substrate for surface enhanced Raman spectroscopy (SERS).

Abbreviations

BSE	Bethe-Salpeter equation
CT	charge transfer
CVD	chemical vapour deposition
DFT	density functional theory
DLA	diffusion limited aggregation
EELS	electron energy loss spectroscopy
FWHM	full width at half maximum
HOPG	highly oriented pyrolytic graphite
ITO	indium tin oxide
NA	numerical aperture
OLED	organic light emitting diode
OTR	oxygen transmission rate
P3HT	poly(3-hexylthiophene)
RH	relative humidity
RPA	random phase approximation
R6G	rhodamine 6G
SERS	surface enhanced Raman spectroscopy
SFM	scanning force microscopy
SP	surface plasmon
TBM	tight binding model
WVTR	water vapour transmission rate

Acknowledgements

I would like to thank Prof. Dr. J.P. Rabe for supervising me and for funding me through the Humboldt-Universität zu Berlin, the Integrative Research Center for the Sciences IRIS Adlershof and Sfb 658. This gave me the opportunity to work on these research projects.

I thank Prof. Dr. J.P. Rabe and Prof. Dr. D.A. Vanden Bout for initiating experiments and Prof. Dr. J.P. Rabe for directing the projects.

Especially I thank Prof. Dr. J.P. Rabe, Dr. Nikolai Severin, Günter Kewes, Prof. Dr. D.A. Vanden Bout and Martin Dorn for useful discussion and for their thoughts contributing to this work.

Furthermore I thank the following persons for their contributions to this work:

Dr. Nikolai Severin gave important ideas on preparation and identification of graphenes and demonstrated dewetting of water confined between mica and graphene under ambient conditions.

Martin Dorn contributed to the design of the experimental configuration making graphenes on thin polymer films detectable. Furthermore I thank him for introducing me in the use of *Mathematica* which was very useful for this thesis.

Günter Kewes conducted time resolved fluorescence decay measurements.

Dr. Nikolai Severin and Martin Dorn supported me with help by scanning force microscopy measurements.

Johannes Frisch gave me useful advice on the fabrication of thin polymer films.

PlasmaChem GmbH and its collaborators offered me the use of their Raman spectrometer to record Raman spectra of graphenes on thin polymer fillms.

PD Dr. Stefan Kirstein and Günter Kewes gave me useful advice on assembly of optics setups.

Prof. Dr. J.P. Rabe, Dr. Nikolai Severin, Prof. Dr. D.A. Vanden Bout and Prof. Dr. O. Benson gave me useful advice on scientific writing.

Manuel Gensler and PD Dr. Stefan Kirstein provided useful discussion on the photochemistry of conjugated molecules.

Dr. Nikolai Severin, Günther Kewes and Dr. Omar Al-Khatib proofread parts of this thesis.

Evi Poblenz, Lothar Geyer and Sabine Schönherr supported me with smooth material purchase. Furthermore Lothar Geyer provided constant IT support.

Finally I thank my room mates and the whole PPM group for the nice atmosphere, having made pleasant years in the group possible.

Reference List

1. K. S. Novoselov *et al.*, Science **306,** 666 (2004).
2. R. R. Nair *et al.*, Science **320,** 1308 (2008).
3. X. Du, I. Skachko, A. Barker, and E. Y. Andrei, Nature Nanotechnology **3,** 491 (2008).
4. A. K. Geim and K. S. Novoselov, Nature Materials **6,** 183 (2007).
5. C. Lee, X. D. Wei, J. W. Kysar, and J. Hone, Science **321,** 385 (2008).
6. N. Severin, M. Dorn, A. Kalachev, and J. P. Rabe, Nano Letters **11,** 2436 (2011).
7. X. Wang, L. J. Zhi, and K. Müllen, Nano Letters **8,** 323 (2008).
8. X. S. Li *et al.*, Science **324,** 1312 (2009).
9. S. Gilje *et al.*, Nano Letters **7,** 3394 (2007).
10. W. S. Hummers and R. E. Offeman, Journal of the American Chemical Society **80,** 1339 (1958).
11. L. Chen, Y. Hernandez, X. L. Feng, and K. Müllen, Angewandte Chemie-International Edition **51,** 7640 (2012).
12. S. Bae *et al.*, Nature Nanotechnology **5,** 574 (2010).
13. P. Matyba *et al.*, Acs Nano **4,** 637 (2010).
14. S. P. Pang, Y. Hernandez, X. L. Feng, and K. Müllen, Advanced Materials **23,** 2779 (2011).
15. Y. Wang *et al.*, Applied Physics Letters **95,** 063302 (2009).
16. T. A. Chen, X. M. Wu, and R. D. Rieke, Journal of the American Chemical Society **117,** 233 (1995).
17. M. Beija, C. A. M. Afonso, and J. M. G. Martinho, Chemical Society Reviews **38,** 2410 (2009).
18. L. Luer *et al.*, Organic Electronics **5,** 83 (2004).
19. M. Manceau *et al.*, Polymer Degradation and Stability **94,** 898 (2009).
20. K. Norrman, S. A. Gevorgyan, and F. C. Krebs, Acs Applied Materials & Interfaces **1,** 102 (2009).
21. J. S. Lewis and M. S. Weaver, Ieee Journal of Selected Topics in Quantum Electronics **10,** 45 (2004).

22. G. Dennler *et al.*, Thin Solid Films **511,** 349 (2006).

23. J. Meyer *et al.*, Advanced Materials **21,** 1845 (2009).

24. K. S. Novoselov *et al.*, Proceedings of the National Academy of Sciences of the United States of America **102,** 10451 (2005).

25. K. S. Novoselov *et al.*, Nature **438,** 197 (2005).

26. P. R. Wallace, Physical Review **71,** 622 (1947).

27. A. B. Kuzmenko, E. van Heumen, F. Carbone, and D. van der Marel, Physical Review Letters **100,** 117401 (2008).

28. J. N. Chen *et al.*, Nature **487,** 77 (2012).

29. Z. Fei *et al.*, Nature **487,** 82 (2012).

30. L. Ju *et al.*, Nature Nanotechnology **6,** 630 (2011).

31. H. G. Yan *et al.*, Nature Nanotechnology **7,** 330 (2012).

32. Y. Liu, R. F. Willis, K. V. Emtsev, and T. Seyller, Physical Review B **78,** 201403 (2008).

33. C. Tegenkamp *et al.*, Journal of Physics-Condensed Matter **23,** 012001 (2011).

34. F. H. L. Koppens, D. E. Chang, and F. J. G. de Abajo, Nano Letters **11,** 3370 (2011).

35. X. Ling *et al.*, Nano Letters **10,** 553 (2010).

36. E. S. Thrall, A. C. Crowther, Z. H. Yu, and L. E. Brus, Nano Letters **12,** 1571 (2012).

37. L. M. Xie *et al.*, Journal of the American Chemical Society **131,** 9890 (2009).

38. J. H. Warner, F. Schäffel, A. Bachmatiuk, and M. H. Rümmeli, *Graphene: Fundamentals and emergent applications* (Elsevier, 2013).

39. G. E. Bacon, Acta Crystallographica **4,** 558 (1951).

40. C. N. R. Rao and A. K. Sood, *Graphene: Synthesis, Properties, and Phenomena* (Wiley-VCH, 2013).

41. A. H. Castro Neto *et al.*, Reviews of Modern Physics **81,** 109 (2009).

42. S. Reich, J. Maultzsch, C. Thomsen, and P. Ordejon, Physical Review B **66,** 035412 (2002).

43. M. I. Katsnelson, European Physical Journal B **51,** 157 (2006).

44. J. H. Chen *et al.*, Nature Physics **4,** 377 (2008).

45. V. G. Kravets *et al.*, Physical Review B **81,** 155413 (2010).

46. D. H. Chae *et al.*, Nano Letters **11,** 1379 (2011).

47. L. Yang *et al.*, Physical Review Letters **103,** 186802 (2009).

48. A. L. Fetter and J. D. Walecka, *Quantum Theory of Many-Particle Systems* (McGraw-Hill Book Company, 1971).

49. B. Wunsch, T. Stauber, F. Sols, and F. Guinea, New Journal of Physics **8,** 318 (2006).

50. K. C. Kao, *Dielectric Phenomena in Solids* (Elsevier, 2004).

51. T. Stauber, J. Schliemann, and N. M. R. Peres, Physical Review B **81,** 085409 (2010).

52. E. Le Ru and P. Etchegoin, *Principles of Surface Enhanced Raman Spectroscopy* (Elsevier, 2009).

53. P. E. Trevisanutto *et al.*, Physical Review Letters **101,** 226405 (2008).

54. M. Klintenberg *et al.*, Journal of Physics-Condensed Matter **21,** 335502 (2009).

55. E. N. Economou, *The Physics of Solids: Essential and Beyond* (Springer, 2010).

56. H. S. Skulason, P. E. Gaskell, and T. Szkopek, Nanotechnology **21,** 295709 (2010).

57. X. F. Wang, Y. P. Chen, and D. D. Nolte, Optics Express **16,** 22105 (2008).

58. J. W. Weber, V. E. Calado, and M. C. M. van de Sanden, Applied Physics Letters **97,** 091904 (2010).

59. L. Novotny and B. Hecht, *Principles of Nano-Optics* (Cambridge, 2006).

60. F. Stern, Physical Review Letters **18,** 546 (1967).

61. S. A. Mikhailov and K. Ziegler, Physical Review Letters **99,** 016803 (2007).

62. S. W. Hwang *et al.*, Physical Review Letters **105,** 127403 (2010).

63. H. G. Frey, S. Witt, K. Felderer, and R. Guckenberger, Physical Review Letters **93,** 200801 (2004).

64. B. Sick, B. Hecht, and L. Novotny, Physical Review Letters **85,** 4482 (2000).

65. H. Weyl, Annalen der Physik **60,** 481 (1919).

66. G. Wentzel, Zeitschrift für Physik **43,** 524 (1927).

67. K. H. Drexhage, Journal of Luminescence **1,2,** 693 (1970).

68. J. S. Kang, G. Piszczek, and J. R. Lakowicz, Journal of Fluorescence **12,** 97 (2002).

69. L. Novotny, Applied Physics Letters **69,** 3806 (1996).

70. Z. Y. Chen *et al.*, Acs Nano **4,** 2964 (2010).

71. L. Gaudreau *et al.*, Nano Letters **13,** 2030 (2013).

72. E. F. Caldin, *The Mechanisms of Fast Reactions in Solution* (IOS Press, 2001).

73. A. M. Michaels, J. Jiang, and L. Brus, Journal of Physical Chemistry B **104,** 11965 (2000).

74. R. M. Stockle, Y. D. Suh, V. Deckert, and R. Zenobi, Chemical Physics Letters **318,** 131 (2000).

75. D. A. Weitz, S. Garoff, J. I. Gersten, and A. Nitzan, Journal of Chemical Physics **78,** 5324 (1983).

76. E. C. Le Ru, E. Blackie, M. Meyer, and P. G. Etchegoin, Journal of Physical Chemistry C **111,** 13794 (2007).

77. D. M. Eisele *et al.*, Nature Chemistry **4,** 655 (2012).

78. A. Pawlik, S. Kirstein, U. DeRossi, and S. Daehne, Journal of Physical Chemistry B **101,** 5646 (1997).

79. G. Scheibe, Kolloid-Zeitschrift **82,** 1 (1938).

80. A. Gonzalez-Tudela *et al.*, Physical Review Letters **110,** 126801 (2013).

81. A. W. Schell *et al.*, Review of Scientific Instruments **82,** 073709 (2011).

82. A. C. Ferrari *et al.*, Physical Review Letters **97,** 187401 (2006).

83. Nemes-Inc, Z. Osvath, K. Kamaras, and L. P. Biro, Carbon **46,** 1435 (2008).

84. P. Blake *et al.*, Applied Physics Letters **91,** 063124 (2007).

85. C. Casiraghi *et al.*, Nano Letters **7,** 2711 (2007).

86. Z. H. Ni *et al.*, Nano Letters **7,** 2758 (2007).

87. S. Roddaro *et al.*, Nano Letters **7,** 2707 (2007).

88. M. Dorn *et al.*, Journal of Applied Physics **108,** 106101 (2010).

89. P. E. Gaskell, H. S. Skulason, C. Rodenchuk, and T. Szkopek, Applied Physics Letters **94,** 143101 (2009).

90. I. N. Shklyarevskii, T. I. Korneeva, and A. N. Ryazanov, Journal of Applied Spectroscopy **4,** 51 (1966).

91. E. D. Palik, *Handbook of Optical constants of Solids* (Academic Press, 1991).

92. R. Q. Png *et al.*, Nature Materials **9,** 152 (2010).

93. C. Uhrich *et al.*, Advanced Functional Materials **17,** 2991 (2007).

94. J. H. Park and S. G. Oh, Materials Research Bulletin **44,** 110 (2009).

95. A. M. C. Ng *et al.*, Thin Solid Films **517,** 1047 (2008).

96. H. Anders, *Dünne Schichten für die Optik* (Wissenschaftliche Verlagsgesellschaft, Stuttgart, 1965).

97. X. Bai and S. Holdcroft, Macromolecules **26,** 4457 (1993).

98. J. Clark, C. Silva, R. H. Friend, and F. C. Spano, Physical Review Letters **98,** 206406 (2007).

99. R. S. Swathi and K. L. Sebastian, Journal of Chemical Physics **129,** 054703 (2008).

100. Y. C. Huang *et al.*, Solar Energy Materials and Solar Cells **93,** 888 (2009).

101. R. T. Yang and C. Wong, Journal of Chemical Physics **75,** 4471 (1981).

102. H. P. Chang and A. J. Bard, Journal of the American Chemical Society **112,** 4598 (1990).

103. A. Tracz, G. Wegner, and J. P. Rabe, Langmuir **9,** 3033 (1993).

104. B. Krauss *et al.*, Physical Review B **79,** 165428 (2009).

105. H. T. Liu *et al.*, Journal of the American Chemical Society **131,** 17099 (2009).

106. N. Severin, S. Kirstein, I. M. Sokolov, and J. P. Rabe, Nano Letters **9,** 457 (2009).

107. R. Bartoszynski and M. Niewiadomska-Bugaj, *Probability and statistical interference* (Wiley, 2008).

108. J. S. Bunch *et al.*, Nano Letters **8,** 2458 (2008).

109. H. H. G. Jellinek and R. Srinivasan, Journal of Physical Chemistry **88,** 3048 (1984).

110. R. Meester, *A natural introduction to probability theory* (Birkhaeuser, 2003).

111. M. S. A. Abdou, F. P. Orfino, Y. Son, and S. Holdcroft, Journal of the American Chemical Society **119,** 4518 (1997).

112. S. Cros *et al.*, Nuclear Instruments & Methods in Physics Research Section B-Beam Interactions with Materials and Atoms **251,** 257 (2006).

113. J. R. Krenn, Nature Materials **2,** 210 (2003).

114. G. L. Harris, *Properties of Silicon Carbide* (INSPEC, 1995).

115. S. Y. El Zaiat, Optics and Laser Technology **33,** 91 (2001).

116. Y. Gao and Z. Yuan, Solid State Communications **151,** 1009 (2011).

117. J. Lu *et al.*, Physical Review B **80,** 113410 (2009).

118. P. Sathy and A. Penzkofer, Journal of Photochemistry and Photobiology A-Chemistry **109,** 53 (1997).

119. D. Fischer, W. R. Caseri, and G. Hahner, Journal of Colloid and Interface Science **198,** 337 (1998).

120. N. Severin, P. Lange, I. M. Sokolov, and J. P. Rabe, Nano Letters **12,** 774 (2012).

121. G. A. Kimmel *et al.*, Journal of the American Chemical Society **131,** 12838 (2009).

122. J. Hu, X. D. Xiao, D. F. Ogletree, and M. Salmeron, Science **268,** 267 (1995).

123. P. Lange *et al.*, Journal of Physical Chemistry C **115,** 23057 (2011).

124. S. H. Khan, G. Matei, S. Patil, and P. M. Hoffmann, Physical Review Letters **105,** 106101 (2010).

125. U. Raviv, P. Laurat, and J. Klein, Nature **413,** 51 (2001).

126. Y. X. Zhu and S. Granick, Physical Review Letters **87,** 096105 (2001).

127. X. Gu, D. Raghavan, J. F. Douglas, and A. Karim, Journal of Polymer Science Part B-Polymer Physics **40,** 2825 (2002).

128. E. Pauliac-Vaujour *et al.*, Physical Review Letters **100,** 176102 (2008).

129. N. Samid-Merzel, S. G. Lipson, and D. S. Tannhauser, Physical Review e **57,** 2906 (1998).

130. L. M. Sander, Nature **322,** 789 (1986).

131. T. A. Witten and L. M. Sander, Physical Review Letters **47,** 1400 (1981).

132. P. G. Saffman and G. Taylor, Proceedings of the Royal Society of London Series A-Mathematical and Physical Sciences **245,** 312 (1958).

133. N. Iyi *et al.*, Applied Clay Science **22,** 125 (2002).

134. T. Govindanunny and B. M. Sivaram, Applied Physics **23,** 253 (1980).

135. M. W. Forbes and R. A. Jockusch, Journal of the American Society for Mass Spectrometry **22,** 93 (2011).

136. F. Kohn, J. Hofkens, and F. C. De Schryver, Chemical Physics Letters **321,** 372 (2000).

137. Y. Liang and A. M. Goncalves, The Journal of Physical Chemistry **89,** 3290 (1985).

138. D. Magde, R. Wong, and P. G. Seybold, Photochemistry and Photobiology **75,** 327 (2002).

139. D. Malacara, *Geometrical and Instrumental Optics* (Academic Press, Inc., 1988), Vol. 25.

140. W. Lukosz, Journal of the Optical Society of America **69,** 1495 (1979).

141. P. Anger, P. Bharadwaj, and L. Novotny, Physical Review Letters **96,** 113002 (2006).

142. R. S. Swathi and K. L. Sebastian, Journal of Chemical Physics **130,** 086101 (2009).

143. G. Gomez-Santos and T. Stauber, Physical Review B **84,** 165438 (2011).

144. D. E. Chang, A. S. Sorensen, P. R. Hemmer, and M. D. Lukin, Physical Review B **76,** 035420 (2007).

145. S. A. Maier, *Plasmonics: Fundamental and Application* (Springer, 2007).

146. E. Busby *et al.*, Journal of Physical Chemistry Letters **2,** 2764 (2011).

147. V. I. Klimov *et al.*, Physical Review B **61,** 13349 (2000).

148. L. Magnani *et al.*, Synthetic Metals **84,** 899 (1997).

149. D. Ricard, Journal of Chemical Physics **63,** 3841 (1975).

150. T. Langer *et al.*, New Journal of Physics **12,** 033017 (2010).

151. M. Tanaka, Plasma Physics and Controlled Fusion **31,** 1049 (1989).

152. C. Sonnichsen *et al.*, Physical Review Letters **88,** 077402 (2002).

153. T. Winzer, A. Knorr, and E. Malic, Nano Letters **10,** 4839 (2010).

154. H. F. Yuan *et al.*, Angewandte Chemie-International Edition **52,** 1217 (2013).

155. J. M. Friedman and R. M. Hochstrasser, Chemical Physics Letters **33,** 225 (1975).

156. S. Shim, C. M. Stuart, and R. A. Mathies, Chemphyschem **9,** 697 (2008).

157. R. J. Stöhr *et al.*, Acs Nano **6,** 9175 (2012).

158. Q. Z. Hao *et al.*, Applied Physics Letters **102,** 011102 (2013).

159. N. Jung *et al.*, Acs Nano **4,** 7005 (2010).

160. X. Ling and J. Zhang, Small **6,** 2020 (2010).

161. Y. Y. Wang *et al.*, Applied Physics Letters **99,** 233103 (2011).

162. H. Xu, L. M. Xie, H. L. Zhang, and J. Zhang, Acs Nano **5,** 5338 (2011).

163. Y. Y. Wang *et al.*, Journal of Physical Chemistry C **112,** 10637 (2008).

164. M. R. Kagan and R. L. Mccreery, Langmuir **11,** 4041 (1995).

165. R. Narula, R. Panknin, and S. Reich, Physical Review B **82,** 045418 (2010).

166. N. Wada and S. A. Solin, Physica B & C **105,** 353 (1981).

167. C. Casiraghi, Physical Review B **80,** 233407 (2009).

168. R. K. Emaus, R. Grunwald, and J. J. Lemasters, Biochimica et Biophysica Acta **850,** 436 (1986).

169. N. Yaginuma, S. Hirose, and Y. Inada, Journal of Biochemistry **74,** 811 (1973).

170. K. F. Mak *et al.*, Physical Review Letters **101,** 196405 (2008).

171. I. N. Shklyarevskii, T. I. Korneeva, and A. N. Ryazanov, Journal of Applied Spectroscopy **4,** 51 (1966).

172. S. Y. Shin *et al.*, Applied Physics Letters **99,** 082110 (2011).

173. S. S. Roy and M. S. Arnold, Advanced Functional Materials **23,** 3638 (2013).

174. D. M. Koller *et al.*, Nature Photonics **2,** 684 (2008).

Publications comprising parts of this work

Articles in scientific journals:

Single- and Double-Layer Graphenes as Ultrabarriers for Fluorescent Polymer Films, Philipp Lange, Martin Dorn, Nikolai Severin, David A. Vanden Bout, Jürgen P. Rabe, The Journal of Physical Chemistry C **115,** 23057 (2011).

Evidence for graphene plasmons in the visible spectral range probed by molecules, Philipp Lange, Günter Kewes, Nikolai Severin, Oliver Benson, Jürgen P. Rabe, submitted.

Graphene plasmon induced Raman enhancement, Philipp Lange, Günter Kewes, Nikolai Severin, Oliver Benson, Jürgen P. Rabe, in preparation.

Reversible Dewetting of a Molecularly Thin Fluid Water Film in a Soft Graphene-Mica Slit Pore, Nikolai Severin, Philipp Lange, Igor M. Sokolov, Jürgen P. Rabe, Nano Letters **12,** 774 (2012).

High contrast optical detection of single graphenes on optically transparent substrates, Martin Dorn, Philipp Lange, Alexey Chekushin, Nikolai Severin, Jürgen P. Rabe, Journal of Applied Physics **108,** 106101 (2010).

Conference contributions:

Encapsulation of thin fluorescent polymer films with graphenes, Philipp Lange, Martin Dorn, Nikolai Severin, David A. Vanden Bout, Jürgen P. Rabe, Poster, DPG Spring Meeting, Regensburg, 2010.

Encapsulation of thin fluorescent polymer films with graphenes, Philipp Lange, Martin Dorn, Nikolai Severin, David A. Vanden Bout, Jürgen P. Rabe, Poster, Polydays 2010: Polymers in Biomedicine and Electronics, Berlin, 2010.

Single and double layer graphenes as ultra-barriers for fluorescent polymer films, Philipp Lange, Martin Dorn, Nikolai Severin, David A. Vanden Bout, Jürgen P. Rabe, Talk, DPG Spring Meeting, Dresden, 2011.

Absolute Raman Cross Section of Rhodamine 6G Confined by Graphene, Philipp Lange, Günter Kewes, Nikolai Severin, Oliver Benson, Jürgen P. Rabe, Poster, XXVIIth International Winterschool on Electronic Properties of Novel Materials; Kirchberg, 2013.